LBNL-39721
UC-405

ERNEST ORLANDO LAWRENCE BERKELEY NATIONAL LABORATORY

A Study of Short Wave Instability on Vortex Filaments

Hong Yun Wang
Computing Sciences Directorate
Mathematics Department

December 1996
Ph.D. Thesis

REFERENCE COPY
Does Not
Circulate
Bldg. 50 Library - Ref.
Lawrence Berkeley National Laboratory
Copy 1
LBNL-39721

DISCLAIMER

This document was prepared as an account of work sponsored by the United States Government. While this document is believed to contain correct information, neither the United States Government nor any agency thereof, nor the Regents of the University of California, nor any of their employees, makes any warranty, express or implied, or assumes any legal responsibility for the accuracy, completeness, or usefulness of any information, apparatus, product, or process disclosed, or represents that its use would not infringe privately owned rights. Reference herein to any specific commercial product, process, or service by its trade name, trademark, manufacturer, or otherwise, does not necessarily constitute or imply its endorsement, recommendation, or favoring by the United States Government or any agency thereof, or the Regents of the University of California. The views and opinions of authors expressed herein do not necessarily state or reflect those of the United States Government or any agency thereof or the Regents of the University of California.

LBNL-39721

A STUDY OF SHORT WAVE INSTABILITY ON VORTEX FILAMENTS *

Hong Yun Wang

Department of Mathematics
and
Lawrence Berkeley National Laboratory
University of California
Berkeley, CA 94720, USA

Ph.D. Thesis

December 1996

* This work was supported in part by the Applied Mathematical Sciences subprogram of the Office of Energy Research, U.S. Department of Energy, under Contract Number DE-AC03-76SF00098.

A Study of Short Wave Instability on Vortex Filaments

Copyright © 1996

by

Hong Yun Wang

The U.S. Department of Energy has the right to use this document
for any purpose whatsoever including the right to reproduce
all or any part thereof

Abstract

A Study of Short Wave Instability on Vortex Filaments

by

Hong Yun Wang
Doctor of Philosophy in Mathematics

University of California at Berkeley

Professor Alexandre J. Chorin, Chair

The numerical stability and accuracy of the vortex method are studied. The effect of the ordinary differential equations (ODE) solver and of the time step on the numerical stability is analyzed. Various ODE solvers are compared and a best performer is chosen. A new constraint on the time step based on numerical stability is proposed and verified in numerical simulations. It is shown through numerical examples that empirical rules for selecting the spatial discretization obtained in simple test problems may not be extended to more general problems.

The thin tube vortex filament method is applied to the problem of Widnall's instability on vortex rings. Numerical results different from previous calculations are presented and the source of the discrepancies is explained. The long time behavior of the unstable mode on thin vortex rings is simulated and analyzed.

The short wave instability on vortex filaments is investigated both theoretically and numerically. It is shown that the short wave instability always occurs on co-rotating vortex filaments of fixed core structure. Furthermore when they are close to each other, vortex filaments produce short wave unstable modes which lead to wild stretching and folding. However, when the inter-filament distance is large in comparison with the core size of the filaments, unstable modes are bounded by a small fraction of the core size and the vortex filaments do not create hairpins nor wild stretching. These findings may explain the smooth behavior of the superfluid vortices.

The formation of hairpin structures on numerical vortex filaments is investigated. It is shown that the formation of hairpin structures is independent of the ODE solver, of the

time step and of other numerical parameters. The hairpin structures are primarily caused by short wave instability on co-rotating vortex filaments.

To my parents,

who have made so many sacrifices for me.

—

To my wife,

who makes this, and all things possible.

Acknowledgements

I would like to thank my advisor Professor Alexandre J. Chorin for his help and guidance. I would also like to thank Professor James Sethian and Professor Philip Marcus for their careful reading of this thesis and useful comments. Finally I would like to thank Donald Krapp for help in correcting grammatical errors.

Contents

List of Figures vii

List of Tables xii

1 Introduction 1

2 Mathematical Background of Fluid Mechanics and Vortex Methods 4
- 2.1 Euler's Equations and the Biot-Savart Law 4
- 2.2 Vortex methods 8
  - 2.2.1 Mathematical Formulation of Vortex Methods 10
  - 2.2.2 Standard Vortex Filament Method and Thin tube Vortex Filament Method 12

3 Instability of A Vortex Ring 14
- 3.1 Historical Review of the Study of Vortex Ring Instabilities 15
- 3.2 Vortex Ring Instabilities 17
  - 3.2.1 Vortex Pair Instability 18
  - 3.2.2 Dispersion Relations 22
  - 3.2.3 Vortex Ring Instability 29

4 Numerical Results Obtained with the Thin Tube Vortex Filament Method 33
- 4.1 Static Simulation of the Velocity of A Vortex Ring 34
- 4.2 Numerical Simulations of the Instability of Vortex Rings Subject to Perturbations of Azimuthal Waves. 36
- 4.3 Dispersion Relation and Stability Analysis for Thin Tube Vortex Filaments 48
- 4.4 Concluding Remarks 59

5 Numerical Stability, ODE Solver, Time Step, Spatial Step and Accuracy 61
- 5.1 Fourier Analysis of Stability and the Highest Discrete Mode on a Numerical Grid 62
- 5.2 Comparison of Various Runge-Kutta Methods on the Model Equation $\zeta'(t) = i\zeta(t)$ 70
- 5.3 Numerical Verifications 77

6 Short Wave Instability On Vortex Filaments Of Fixed Core Structure In A Co-rotating Vorticity Field **84**

6.1 Short wave instability on a co-rotating vortex pair 86

6.2 Numerical simulations of short wave instability on a co-rotating vortex pair 97

6.3 Short wave instability on a vortex filament immersed in a co-rotating vorticity field 113

6.3.1 A vortex filament embedded in a continuous vorticity field 113

6.3.2 A vortex filament immersed in a discrete vorticity field 116

6.4 Short wave instability and the proliferation of vortex hairpins in three dimensional vortex methods 122

7 Conclusions **135**

Bibliography **138**

List of Figures

2.1 A vortex line. 6
2.2 A vortex tube. 6
2.3 A front-on view of a vortex ring with ring radius R and core radius δ 8
2.4 A vortex segment. 13

3.1 A perturbed vortex pair of opposite circulation. 19
3.2 A cross-section of the vortex pair. 20
3.3 The core cross-sections before and after the perturbation for various azimuthal wave numbers. The solid curves denote the unperturbed core, the dashed curves denote the perturbed core. 24
3.4 The left hand side (solid curve) and the right hand side (dashed curve) of equation (3.30) as functions of $\beta\delta$. 26
3.5 Oscillation frequencies of the first four radial modes on a filament with constant vorticity. 27
3.6 Comparison of the exact (solid line) and asymptotic (dashed line) dispersion relations for waves on a vortex filament with constant vorticity. 28
3.7 Radial velocities at various locations for the first (a) and the second (b) radial modes. 29
3.8 Thick curve: the part of the filament curve responsible for the self-induced rotation of the waves around the ring; thin curve: the remainder of the ring. 30

4.1 Comparison of the numerical velocity and the asymptotic velocity of a vortex ring. Here the "+" denotes the numerical velocity while the solid line denotes the asymptotic velocity. 35
4.2 The perturbed vortex ring and the coordinate system 37
4.3 Evolution of the amplitude of the perturbation for the ring perturbed at wavenumber $n = 2, 5, 8, 10, 12, 13$, respectively. The solid line denotes the amplitude $\triangle\rho$ in the radial direction and the dashed line denotes the amplitude $\triangle z$ in the streamwise direction. 41
4.4 Evolution of the amplitude of the perturbation for the ring perturbed at $n = 14$. Notice the periodic behavior of the evolution, which is in contrast with Knio and Ghenoiem's result. 42

4.5 Evolution of the amplitude of the perturbation for the ring perturbed at $n = 14$, 15, 17, and 19. The solid line corresponds to the amplitude in the radial direction and the dashed line corresponds to the amplitude in the streamwise direction. 43
4.6 Comparison of the numerical results with different values of h/δ for the evolution of the perturbation wave. The ring is perturbed at wave number $n = 13$. The solid line corresponds to the amplitude in the radial direction and the dashed line corresponds to the amplitude in the streamwise direction. . . . 44
4.7 Comparison of the numerical results with different values of h/δ for the evolution of the perturbation. The ring is perturbed at wave number $n = 14$. The solid line corresponds to the amplitude in the radial direction and the dashed line corresponds to the amplitude in the streamwise direction. . . . 45
4.8 Evolution of the perturbation corresponding to different values of the initial amplitude. Notice that the amplitudes for $n = 10$ and $n = 13$ are bounded by their initial values so $n = 10$ and $n = 13$ are both stable modes. 46
4.9 Evolution of the perturbation for various initial values. Notice that the amplitudes for $n = 15$ are bounded by their initial values, whereas the amplitudes for $n = 14$ always grow to the same maximum values regardless of the initial values. Hence $n = 14$ is an unstable mode while $n = 15$ is a stable mode. . . 47
4.10 Frequency vs wavenumber. 49
4.11 A cross-section of the perturbed vortex ring (left) with a local coordinate system (right). 50
4.12 Trajectories of the waves ($n = 13$ and $n = 15$) with respect to the unperturbed position. All coordinates have been normalized by the initial amplitude. 51
4.13 Frequency vs perturbation amplitude. $-$: $k\delta = 1.4$, $-o-$: $k\delta = 1.375$, $--$: $k\delta = 1.35$, where k is wave number and δ is the core size 52
4.14 (a). A family of hyperbolas and the direction of the motion on them, predicted by the stagnation point flow plus the dispersion relation of sinusoidal waves with small amplitude. (b). The motion of perturbation waves, with respect to the unperturbed filament, obtained in the numerical simulations. $-.-$: initial amplitude $\varepsilon = 0.2\delta$, $-$: $\varepsilon = 0.1\delta$, $--$: $\varepsilon = 0.05\delta$. All coordinates have been normalized by the core size. 53
4.15 Comparison of the evolution of the corresponding unstable mode on a vortex ring for different core sizes. The solid line represents the amplitude in the radial direction and the dashed line represents the amplitude in the streamwise direction. 55
4.16 Comparison of the evolution of the corresponding unstable mode on a vortex ring for different core sizes. The solid line represents the amplitude in the radial direction and the dashed line represents the amplitude in the streamwise direction. 56
4.17 Comparison of the evolution of the corresponding unstable mode on a vortex ring for different core sizes. The solid line represents the amplitude in the radial direction and the dashed line represents the amplitude in the streamwise direction. 57

4.18 Numerical result for the large initial perturbation. The solid line represents the amplitude in the radial direction and the dashed line represents the amplitude in the streamwise direction. 58

5.1 (a). The amplification factor $|\rho(\xi,\lambda)|$ vs ξ for $\lambda = 3/4$. (b). The amplification factor $|\rho(\xi,\lambda)|$ vs λ for the most unstable mode $\xi = \pi$. 64
5.2 Upwind scheme: (a). The amplification factor $|\rho(\xi,\lambda)|$ vs ξ for $\lambda = 3/2$; (b). The amplification factor $|\rho(\xi,\lambda)|$ vs λ for the most unstable mode $\xi = \pi$. . . 65
5.3 Lax-Wendroff scheme: (a). The amplification factor $|\rho(\xi,\lambda)|$ vs ξ for $\lambda = 3/2$; (b). The amplification factor $|\rho(\xi,\lambda)|$ vs λ for the most unstable mode $\xi = \pi$. 66
5.4 A sketch of the highest discrete mode. 67
5.5 Amplification factor of the forward Euler method. 72
5.6 Amplification factor of the prediction-correction method. 73
5.7 Amplification factor of the Heun third order method. 73
5.8 Amplification factor of the classical Runge-Kutta method. 74
5.9 Amplification factor of the Prince-Dormand 5(4) method. 74
5.10 Heun third order method: Comparison of numerical results for different time steps. 80
5.11 Classical fourth order Runge-Kutta method: Comparison of numerical results for different time steps. 81
5.12 Comparison of numerical results for different h/δ. 82
5.13 Comparison of numerical results for different h/δ. 83

6.1 An unperturbed co-rotating vortex pair. 87
6.2 A cross-section of the unperturbed vortex pair. 88
6.3 A perturbed vortex pair of the same circulation. 89
6.4 A cross-section of the perturbed vortex pair. 90
6.5 A sketch of the motion of the right filament in Fig. 6.4. 91
6.6 Normalized rotation frequency $\tilde{\Omega}$ as a function of normalized wavenumber $\tilde{k}$ for the core vorticity distribution derived from the cut-off function (6.17) . . 92
6.7 Normalized rotation frequency $\tilde{\Omega}$ as a function of normalized wavenumber $\tilde{k}$ for the core vorticity distributions determined by various cut-off functions: (a) cut-off function (6.18), (b) cut-off function(6.19), (c) cut-off function (6.20), (d) cut-off function (6.21). 94
6.8 The unstable region in the $(b/\delta, \tilde{k})$ plane for a co-rotating vortex pair. . . . 97
6.9 Time evolution of the perturbations of different wavenumbers on a pair of co-rotating vortex filaments. Dashed line : amplitude in the x-direction (spanwise direction); Solid line : amplitude in the y-direction. The coordinate system is rotating with the vortex pair. 106
6.10 Time evolution of the perturbations with different initial amplitudes on a pair of co-rotating vortex filaments. Dashed line : amplitude in the x-direction (spanwise direction); Solid line : amplitude in the y-direction. The coordinate system is rotating with the vortex pair. 107

6.11 Time evolution of the perturbations with different initial amplitudes on a pair of co-rotating vortex filaments. Dashed line : amplitude in the x-direction (spanwise direction); Solid line : amplitude in the y-direction. The coordinate system is rotating with the vortex pair. 108
6.12 Normalized rotation frequency vs amplitude/core radius. $-o-$: $k\,\delta = 1.40$; $-+-$: $k\,\delta = 1.45$; $-*-$: $k\,\delta = 1.50$. 109
6.13 The predicted trajectory of the perturbed filament relative to its unperturbed position. The theory is valid only for large b/δ. 109
6.14 Time evolution of the perturbations on a pair of co-rotating vortex filaments with different separations. Dashed line : amplitude in the x-direction (spanwise direction); Solid line : amplitude in the y-direction. The coordinate system is rotating with the vortex pair. 110
6.15 Time evolution of the perturbations on a pair of co-rotating vortex filaments with different separations. Dashed line : amplitude in the x-direction (spanwise direction); Solid line : amplitude in the y-direction. The coordinate system is rotating with the vortex pair. 111
6.16 Time evolution of the perturbation on a pair of co-rotating vortex filaments. Dashed line : amplitude in the x-direction (spanwise direction); Solid line : amplitude in the y-direction. The coordinate system is rotating with the vortex pair. 112
6.17 Configuration of the vortex pair after the two filaments become tangled together. 112
6.18 A vortex filament surrounded by a continuous vorticity field. 114
6.19 The vortex filament and the coordinate system attached to it. 115
6.20 A sketch of the motion of a filament surrounded by a continuous vorticity field. 116
6.21 Layouts of numerical filaments. Here the solid circles are for illustration only. They do not describe the real size of the cross-section of numerical filaments. In fact, the overlapping condition requires that the core radius of the numerical filaments be larger than the inter-filament distance. 118
6.22 Velocity field and streamlines near the filament. 120
6.23 Velocity field and streamlines near the filament. 121
6.24 Configuration of the numerical filaments obtained with single precision and $dt = 0.04$. 128
6.25 Two-dimensional views of the numerical filaments obtained in the single precision calculation. 129
6.26 Two-dimensional views of the numerical filaments obtained in the double precision calculation. 129
6.27 Numerical results obtained in single precision calculations using different time steps. 130
6.28 Numerical results obtained in the single precision calculation where $N_{layer} = 2$, $N_{filament} = 19$, $\delta = 0.12$ and $dt = 0.04$. 131
6.29 Numerical results obtained in the single precision calculation where $N_{layer} = 3$, $N_{filament} = 37$, $\delta = 0.10$ and $dt = 0.04$. 132
6.30 Two perspective views of one filament in a co-rotating vortex pair. 133

6.31 Two perspective views of one filament in 7 numerical filaments which are used to represent the vortex ring. 133
6.32 Two perspective views of one filament in 19 numerical filaments which are used to represent the vortex ring. 134
6.33 Two perspective views of one filament in 37 numerical filaments which are used to represent the vortex ring. 134

List of Tables

5.1 The values of F as a function of $\tilde{\varepsilon}$ and $\tilde{h}$. 69
5.2 The values of F corresponding to different cut-off functions. 70
5.3 The interval I for different ODE solvers. 76

Chapter 1

Introduction

Tube-like vortex structures occur in many types of flow and are also predominant in turbulence [15], [21], [24], [25], [50], [51], [52], [64], [65]. The main work of this dissertation is to study the vortex methods and the short wave instability on vortex filaments of fixed core structure.

In a three-dimensional, inviscid, incompressible flow, vorticity remains confined to a small fraction of the total volume of the field and a complete simulation scheme for the flow can be built on the tracking of the vorticity field in Lagrangian coordinates. These facts make vortex methods particularly attractive [3], [10], [18], [29], [75] [87]. We study vortex methods by considering numerical stability, accuracy, ordinary differential equations (ODE) solver, time step and space step. The evolution of perturbed vortex rings in an inviscid flow is selected as a model problem for the validation study of the vortex methods. The choice of this problem was motivated by several reasons. First, vortex rings are very important building blocks for complicated vorticity configurations and they also arise in a variety of jet flows of practical interest; second, the same problem has been numerically simulated by Knio and Ghoniem [57]; third, Widnall *et al* [96], [95], [97], did a theoretical stability analysis for vortex rings. The numerical results obtained in the previous study [57] contain an artifact of the numerics due to an underresolved numerical mesh. The correct numerical solutions are obtained with a sufficiently refined mesh. We demonstrate that the choice of spatial step size is problem dependent and thus cannot be determined by an empirical criterion obtained in a simple test problem. For the thin tube vortex filament method, various numerical ODE solvers are analyzed and compared. Among these ODE solvers, the classical fourth order Runge-Kutta method comes out as the best performer. A

new criterion for selecting the time step is proposed based on a study of numerical stability, and is verified in numerical simulations.

After the validation study of vortex methods, we investigate short wave instabilities on co-rotating vortex filaments of fixed core structure. Several cases are examined including a co-rotating vortex pair, a vortex filament surrounded by many other co-rotating vortex filaments and a vortex filament in a straining flow induced by a co-rotating vorticity field. Short wave instability is found to always occur on co-rotating vortex filaments of fixed core structure. When these vortex filaments are far apart from each other, i.e. the inter-filament distance is large compared to the core size, the amplitudes of unstable modes are bounded by a small fraction of core size and, more important, the vortex filaments do not develop hairpin structures nor wild stretching. When the vortex filaments are close to each other, i.e. the inter-filament distance is comparable to or smaller than the core size, unstable modes grow without bound and the vortex filaments stretch and fold violently. These results of short wave instability on vortex filaments are derived from a theoretical analysis and are verified in numerical simulations. In particular, phenomena which are observed in numerical simulations but are not predicted in the analysis are explained by doing further analysis with refined models.

Superfluid vortices offer an interesting example where our analysis applies. Superfluid vortex filaments behave differently from the classical vortex filaments [31], [37], [38], [90]. In particular, classical vortex filaments stretch and fold wildly , and form small scale structures while superfluid vortex filaments remain smooth. It is well known that superfluid vortex filaments have a very small core size ($\sim$ O(Å)) and have fixed core structures [37], [38], [90]. Thus the superfluid vortex filaments are far apart from each other in the sense that the inter-filament distance is much larger than the core size. Our study of the short wave instability reveals that when vortex filaments are far apart, the unstable modes are bounded by a small fraction of the core size and more importantly the unstable modes do not cause the catastrophic stretching and folding. Therefore the short wave instability is insignificant for superfluid vortex filaments. This may imply that the tiny core size of the superfluid vortex filaments is more important in accounting for their non-classical dynamics than the quantization of circulation. The different behavior of the superfluid vortices and classical vortices has been explained by Chorin [23], [27], [31], [30], with the use of statistical theories. Our study of the short wave instability reinforces Chorin's analysis from a very different point of view.

We continue on to study the formation of hairpin structures. In computations with vortex methods, vorticity blows up and small scale hairpin structures appear [11], [22], [26], [28]. The coupling of small scales with large scales makes simulations of long time behavior impractical since the complexity of the flow outstrips the available computer capacity in a short time. Chorin [26], [28] proposed a hairpin removal algorithm to resolve this problem, based on a renormalization group procedure. However, the origin of the hairpin structures had not been shown. We show that the formation of hairpin structures is independent of the numerical ODE solver, of the time step, of the spatial step and of other numerical parameters. The formation of hairpin structures is not caused by numerical instability. Instead it is caused by short wave instability on co-rotating vortex filaments.

The outline of this dissertation is as follows. Chapter 2 gives some mathematical background on fluid mechanics and introduces vortex methods. In Chapter 3 we review Widnall's stability analysis of a vortex ring, which serves as a theoretical foundation for our analysis of short wave instability. Numerical results obtained by the thin tube vortex filament method are presented in Chapter 4. The differences between our results and those in the previous study are pointed out and explained. In Chapter 5, we focus on numerical considerations of the thin tube vortex filament method. The selection of the numerical ODE solver, the time step, and the spatial step is addressed in detail. Chapter 6 is devoted to the study of short wave instability on vortex filaments of fixed core structure surrounded by a co-rotating vorticity field. The different behavior of the unstable modes on vortex filaments which are close to each other and the unstable modes on vortex filaments far apart is analyzed and numerically simulated. The origin of hairpin structures and of the wild stretching of numerical vortex filaments is revealed. Finally, in Chapter 7 we summarize the conclusions of the dissertation.

These conclusions are: neighboring co-rotating vortices induce short wave unstable modes which lead to stretching and folding; an isolated vortex filament will not create hairpins or wild stretching; the formation of hairpins on numerical vortex filaments is not caused by numerical instability, rather, it is caused by the short wave instability on neighboring co-rotating vortex filaments. These results may explain the different behavior of superfluid vortices and of classical fluid vortices.

Chapter 2

Mathematical Background of Fluid Mechanics and Vortex Methods

This chapter introduces some mathematical background of fluid mechanics and gives a short review of vortex methods which are one of the building blocks of this thesis. We divide this chapter into two parts. In the first section, we introduce Euler's equations, the Biot-Savart law and the motion of vortex ring. In the second section, we briefly review vortex methods [29], [86], [87].

2.1 Euler's Equations and the Biot-Savart Law

This section summarizes some of the important facts about vortex dynamics.

Following Chorin & Marsden [34], we consider three dimensional, unbounded, incompressible, inviscid flows. The dynamics of this class of flows is governed by Euler's equations, which may be written as

$$\frac{\partial \mathbf{u}}{\partial t} + (\mathbf{u} \cdot \nabla)\mathbf{u} = -\nabla P, \tag{2.1}$$

$$\nabla \cdot \mathbf{u} = 0, \tag{2.2}$$

where $\mathbf{u}(\mathbf{x}, t) = (u, v, w)$ is the velocity field, $\mathbf{x} = (x, y, z)$ is the position vector, t is time, $\nabla = (\partial_x, \partial_y, \partial_z)$ is the gradient operator, P is pressure and we have assumed the unit density ($\rho = 1$). Equation (2.1) expresses the conservation of momentum while equation (2.2) is a consequence of incompressibility and the conservation of mass.

The vorticity $\boldsymbol{\omega}$ of a flow field is defined as the curl of the velocity $\mathbf{u}$, i.e.,

$$\boldsymbol{\omega} = \nabla \times \mathbf{u}. \tag{2.3}$$

Taking the curl of Euler's equation (2.1) and using the incompressibility condition (2.2), we readily obtain Euler's equations in terms of vorticity in three space dimensions, which read

$$\frac{\partial \boldsymbol{\omega}}{\partial t} + (\mathbf{u} \cdot \nabla)\boldsymbol{\omega} = (\boldsymbol{\omega} \cdot \nabla)\mathbf{u}, \tag{2.4}$$

or equivalently,

$$\frac{D\boldsymbol{\omega}}{Dt} = (\boldsymbol{\omega} \cdot \nabla)\boldsymbol{\omega}, \tag{2.5}$$

where $\frac{D}{Dt}$ denotes the material derivative. Equation (2.5) is also called the vorticity transport equation. In this equation, the term $(\mathbf{u} \cdot \nabla)\boldsymbol{\omega}$ is responsible for the convection of the vorticity $\boldsymbol{\omega}$, and the term $(\boldsymbol{\omega} \cdot \nabla)\mathbf{u}$ corresponds to the rotation and stretching of $\boldsymbol{\omega}$.

Now we introduce vortex lines, vortex tubes and vortex filaments. By definition, a vortex line is a line that is tangent to the vorticity vector $\boldsymbol{\omega}$ at each of its points. It follows from the vorticity transport equation (2.5) that vortex lines move with the fluid (see Chorin & Marsden [34] for a proof). A vortex tube consists of all vortex lines drawn through a two-dimensional surface S which is nowhere tangent to the vorticity $\boldsymbol{\omega}$. A sketch of a vortex line and a vortex tube are shown in Figure 2.1 and Figure 2.2 respectively. A vortex filament represents a vorticity field which is nonzero inside a tube-shaped region and zero outside the region. Usually on any cross-section of a vortex filament, the vorticity field points in roughly the same direction. The concept of two or more vortex filaments refers to the vorticity field obtained by superposing the vorticity field represented by each vortex filament. Thus it makes sense to talk about overlapping vortex filaments.

The circulation of a vortex tube is defined as

$$\Gamma = \oint_C \mathbf{u} \cdot d\mathbf{l}, \tag{2.6}$$

where C is a curve encircling the vortex tube. The circulation Γ defined by (2.6) is a constant independent of the shape and location of the contour C (Helmholtz's theorem) and is also independent of time (Kelvin's theorem). A related observation is that vortex tubes cannot terminate in a fluid. Vortex tubes either form loops entirely within a fluid, extend to infinity, or end at a solid boundary.

Since the vorticity transportation equation (2.5) involves the fluid velocity $\mathbf{u}$, it is essential that we determine the velocity $\mathbf{u}$ from the vorticity $\boldsymbol{\omega}$. To do this, we first find a

particular divergence free velocity field $\mathbf{u}$ satisfying $\nabla \times \mathbf{u} = \boldsymbol{\omega}$. Boundary conditions may be satisfied by adding a potential flow to $\mathbf{u}$.

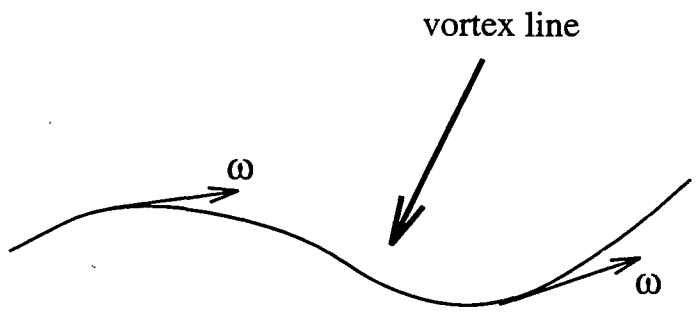

Figure 2.1: A vortex line.

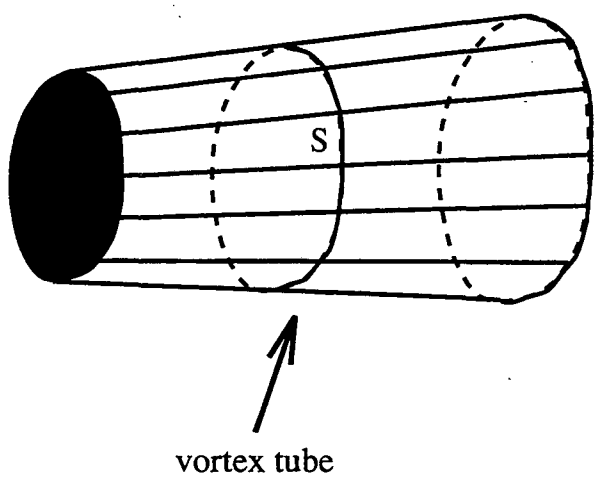

Figure 2.2: A vortex tube.

The vanishing of $\nabla \cdot \mathbf{u}$ in three dimensional space implies the existence of a vector potential function ϕ such that

$$\mathbf{u} = \nabla \times \phi, \tag{2.7}$$

$$\text{and} \qquad \nabla \cdot \phi = 0. \tag{2.8}$$

Consequently

$$\omega = \nabla \times \mathbf{u} = -\triangle\phi + \nabla(\nabla \cdot \phi) = -\triangle\phi, \tag{2.9}$$

where $\triangle = (\frac{\partial^2}{\partial x^2}, \frac{\partial^2}{\partial y^2}, \frac{\partial^2}{\partial z^2})$ is the Laplacian operator.

Equation (2.9) is a Poisson's equation for ϕ. A particular solution of equation (2.9) is given by the convolution of the vorticity ω with $G(\mathbf{x}) = \frac{1}{4\pi|\mathbf{x}|}$, the Green's function for the Laplace equation $\triangle\phi = 0$. So

$$\phi = G * \omega = \int_{R^3} G(\mathbf{x} - \mathbf{x}')\omega(\mathbf{x}')d\mathbf{x}'. \tag{2.10}$$

Taking the curl of equation (2.10) yields a particular solution for $\mathbf{u}$:

$$\mathbf{u} = \nabla \times \phi = \int K(\mathbf{x} - \mathbf{x}') \times \omega(\mathbf{x}')d\mathbf{x}', \tag{2.11}$$

where the convolution kernel $K(\mathbf{x})$ is

$$K(\mathbf{x}) = \nabla G(\mathbf{x}) = -\frac{1}{4\pi}\frac{\mathbf{x}}{|\mathbf{x}|^3}. \tag{2.12}$$

Equation (2.11) is called the *Biot-Savart law.* One can verify that the velocity $\mathbf{u}$ given by equation (2.11) satisfies the equation $\nabla \times \mathbf{u} = \omega$ and the incompressibility condition $\nabla \cdot \mathbf{u} = 0$. Furthermore, in the case where the vorticity field ω has compact support, the velocity $\mathbf{u}$ given by equation (2.11) vanishes at infinity. The significance of the Biot-Savart law lies in the fact that once the vorticity field ω has been found, the velocity field $\mathbf{u}$ may be readily obtained. This result is particularly useful for numerical computations of flow fields using vortex methods which will be introduced in the next section.

Finally, one can use the Biot-Savart law to evaluate the propagating velocity of a thin vortex ring. The term "vortex ring" refers to a torus-shaped region of vorticity in a fluid in which vortex lines form closed loops (see Figure 2.3). The torus-shaped region is usually called the core of the vortex ring.

We call a vortex ring *a thin vortex ring* if its core radius is small in comparison with its ring radius. In the absence of viscosity, a thin vortex ring of ring radius R and core radius δ will move at a constant rate along its axis of symmetry with no change of shape. The velocity of translation is [60]

$$U_T = \frac{\Gamma}{4\pi R}\left[\ln(\frac{8R}{\delta}) + C + O(\delta/R)\right], \tag{2.13}$$

where Γ is the circulation and the constant C depends on the distribution of vorticity within the ring. For a constant vorticity distribution, $C = -0.25$. For a second order Gaussian vorticity distribution, $C = -0.558$.

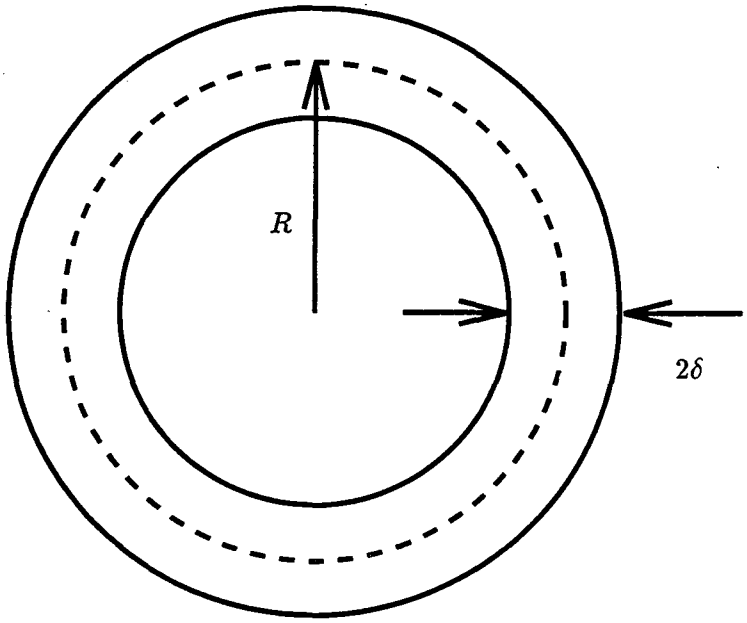

Figure 2.3: A front-on view of a vortex ring with ring radius R and core radius δ .

2.2 Vortex methods

Vortex methods [7], [13], [17], [40], [47], [62], [77], [80], [81], [93] are a type of numerical method for approximating the solution of the incompressible Euler or Navier-Stokes equations. In vortex methods, the underlying discretization is of the vorticity field rather than the velocity field. This discretization is Lagrangian in nature and usually consists of a collection of particles which carry concentrations of vorticity with them. The velocity field is approximately recovered by first evaluating the Biot-Savart law based on the discretized vorticity field and then imposing a potential flow field to satisfy the boundary condition. The vorticity field is then evolved in time according to the vorticity transport equation using the recovered velocity field.

Many incompressible flows at high Reynolds numbers are characterized by regions of concentrated vorticity embedded in irrotational fluid. If finite difference or finite element methods are applied to solve the Navier-Stokes equation in velocity-pressure form, the whole domain of the flow has to be covered by numerical grids since the velocity field is not localized. In the case where the flow is inviscid or has high Reynolds number, the grid size has to be very small at least in the region where the vorticity field is concentrated so that the numerically induced grid scale dissipation and dispersion will not change the physical

properties of the flow. To overcome these numerical difficulties, Chorin [18], [19], [20], [22] proposed the vortex methods which discretize the equation of fluid motion in vorticity form rather than in the usual velocity-pressure form. The inviscid motion of the vorticity is given by the local fluid velocity which in turn is determined from the vorticity field by the Biot-Savart law and the superposition of a potential velocity field to satisfy the boundary conditions. This technique has the advantage that the pressure is eliminated from the number of dependent variables to be computed and the velocity field recovered by the Biot-Savart law is automatically divergence free. In addition, the vorticity field is represented in terms of particles of vorticity, usually referred to as vortex blobs in the two dimensional case or as vortex segments in the three dimensional case. These particles are generally called vortex elements, which induce motion on each other. Thus the vortex methods are adaptive methods in the sense that numerical particles are automatically distributed in the regions where the vorticity is concentrated. Furthermore, the vortex methods are grid-free. Thus they have no numerical grid scale dissipation which is often associated with the finite difference methods and caused by repeatedly mapping the solution back onto a fixed numerical mesh. The representation of the vorticity field as particles of identical vorticity distribution at various locations is both mathematically appealing and relatively straightforward to implement. As a consequence of the Biot-Savart law, the velocity field is a linear combination of basic velocity functions which are the convolutions of an integral kernel with the vorticity distribution of particles and hence are identical to each other up to a shift.

We will restrict ourselves to the study of inviscid flows in three space dimensions. In the following we first give an introduction to the mathematical formulation of vortex methods. Then we describe two special kinds of vortex methods: the so-called thin tube vortex filament method and the standard vortex filament method. The main difference between them is that the thin tube vortex filament method uses one numerical filament to approximate the vorticity field and the core of the vortex filament is fixed, whereas the standard vortex filament method uses many numerical filaments of fixed core structure which can simulate the evolution of the core structure of the physical vortex filament.

2.2.1 Mathematical Formulation of Vortex Methods

In this section, we discuss the formulation of vortex methods for three-dimensional unbounded inviscid flow. Our approach follows the discussion by Chorin [29].

Suppose we approximate the vorticity field $\boldsymbol{\omega}$ by a collection of vortex lines and concentrate the vorticity on these lines. The divergence-free property of $\boldsymbol{\omega}$ implys that the flux of vorticity along a vortex line is a constant. Let Γ_i denote vorticity flux along the i-th line, then the Biot-Savart law (2.11) becomes

$$\mathbf{u}(\mathbf{x}) = \sum_i \Gamma_i \int_{\text{along } i\text{-th line}} K(\mathbf{x} - \mathbf{x}'(s)) \times ds. \tag{2.14}$$

This expression is difficult to approximate numerically because the kernel K typically becomes singular near the vortex filaments. Thus, if vortex filaments come close together, they can induce extremely large velocities on one another.

The basic idea behind vortex methods is to replace the singular kernel K by a smoother object K_δ to limit this singular interaction:

$$\mathbf{u}(\mathbf{x}) = \sum_i \Gamma_i \int_{\text{along } i\text{-th line}} K_\delta(\mathbf{x} - \mathbf{x}'(s)) \times ds. \tag{2.15}$$

The smooth kernel K_δ is a smooth function which approximates the singular kernel K in the distribution sense. A large number of smoothed kernels have been constructed, providing vortex methods of various orders of accuracy. In general, the smoothed kernel K_δ can be constructed as follows.

Let $g(\mathbf{x})$ be a radially symmetric function such that

1. $\int g(\mathbf{x})d\mathbf{x} = 1$,
2. $\int x_1^{\alpha_1} x_2^{\alpha_2} x_3^{\alpha_3} g(\mathbf{x})d\mathbf{x} = 0$, for $\alpha_i \geq 0$ $(i = 1, 2, 3)$ and $\alpha_1 + \alpha_2 + \alpha_3 < p$,

where p is an integer. Define a narrowly peaked function g_δ as:

$$g_\delta(\mathbf{x}) = \frac{1}{\delta^3} g(\frac{\mathbf{x}}{\delta}). \tag{2.16}$$

As δ goes to zero, function g_δ converges to the Dirac delta function in the sense of distribution. Thus, one can define the smooth kernel K_δ as the convolution of the original kernel K with function g_δ.

$$K_\delta(\mathbf{x}) = K * g_\delta(\mathbf{x}) = \int K(\mathbf{x} - \mathbf{x}')g_\delta(\mathbf{x}')d\mathbf{x}'. \tag{2.17}$$

Clearly, as δ goes to zero K_δ converges to K in the sense of distributions. In the theory of vortex methods, g_δ is called the *vorticity core cutoff function* or the *core function*, and the subscript δ refers to the *cutoff radius* or *numerical core size.* Using the fact that $g(\mathbf{x})$ is radially symmetric, equation (2.17) can be written as

$$\begin{aligned} K_\delta &= \int K(\mathbf{x}-\mathbf{x}')g_\delta(\mathbf{x}')d\mathbf{x}' \\ &= K(\mathbf{x})f(\frac{|\mathbf{x}|}{\delta}), \end{aligned} \tag{2.18}$$

where $f(r)$ is called the *velocity smoothing function* and is related to the vorticity core cutoff function $g(r)$ as

$$f'(r) = 4\pi r^2 g(r). \tag{2.19}$$

A standard example of an appropriate velocity smoothing function $f(r)$ is the fourth-order Beale-Majda smoothing function [10]:

$$f(r) = 1 + (\frac{3}{2}r^3 - 1)\, e^{-r^3}. \tag{2.20}$$

The accuracy of the vortex method depends on several factors: (1). the size of the mesh h used in the discretization of the initial vorticity distribution; (2). the cutoff radius δ; (3). the choice of smoothing function f; and (4). the ODE solver and the time step used to solve the ordinary differential equations for the particle trajectories. Since the introduction of smoothed vortex methods, considerable theory has been developed studying accuracy and convergence as a function of these parameters.

The first proof of the convergence of vortex methods in two space dimensions was constructed by Hald and del Prete [45]. In their work, several types of smoothed kernels were considered and short-time convergence was established. In 1979 Hald [43] gave the proof of long-time convergence of the vortex methods. He analyzed the relation between h, δ and the rate of convergence. He found that if $h = \delta^2$, then for a certain class of smoothing functions, the difference between the computed particle trajectories and the exact particle trajectories is of order $O(h^2)$. In other words, as one uses more vortex elements to resolve an initial vorticity approximation (that is, as $h \to 0$), linking the cutoff radius δ to the number of vortices yields convergence of the position of the vortices to their exact trajectories. On the basis of Hald's work, Beale and Majda [8], [9] showed that carefully designed vortex methods for smooth inviscid flow could provide results of any desired degree of accuracy in both two and three space dimensions. Their three-dimensional vortex method

updates three-dimensional vortex stretching by computing derivatives along the particle paths. Their proofs were technical, and much of work that followed was aimed at simplying the arguments. For example, Anderson and Greengard [3] gave a simpler consistency argument and a convergence proof which takes into account the time step error associated with the integration along particle trajectories. Hald [44] then showed convergence for an extremely wide class of two-dimensional methods, requiring only Holder continuity in the vorticity field, as well as fourth-order convergence for the classical Runge-Kutta techniques for the integration of ordinary differential equations. Proofs of the three-dimensional method with explicit differentiation were also provided by Beale and Majda [8], [9].

In tandem with these theoretical investigations, many numerical convergence studies have examined the actual accuracy obtained in practice (for example, see Sethian and Ghoniem [88]). Later in this thesis, we will present a careful, detailed study of the choice of time step $\triangle t$ and mesh size h for the thin tube vortex filament method.

2.2.2 Standard Vortex Filament Method and Thin tube Vortex Filament Method

For computational purposes, the standard vortex filament method algorithm starts with approximating the vorticity field $\boldsymbol{\omega}(\mathbf{x}, t)$ by a finite collection of overlapping numerical vortex filaments L_i $(i = 1, ..., N)$. Each of the filament L_i is approximated by n_i segments, i.e., short, thin, circular cylinders whose axis is tangent at a point to the vorticity vector. The (i, j)-th segment (the j-th element on the i-th filament, $1 \leq j \leq n_i$, $1 \leq i \leq N$) is represented by a circulation Γ_i and by two Lagrangian variables $\mathbf{x}_{i,j}$, $\mathbf{x}_{i,j+1}$ which describe the centers of the base and top of the segment respectively.

A sketch of a vortex segment is drawn in Figure 2.4 . No segment is allowed to be longer than a predetermined bound h, in other words, $|\mathbf{x}_{i,j+1} - \mathbf{x}_{i,j}| \leq h$ for $1 \leq j \leq n_i$, $1 \leq i \leq N$. If the length of a segment exceeds h, the segment is cut into two new segments. The coordinates of the new segments can be obtained by linear interpolation.

Denote the center of the (i, j)-th vortex segment by

$$\mathbf{x}^c_{i,j} = \frac{1}{2}(\mathbf{x}_{i,j} + \mathbf{x}_{i,j+1}). \tag{2.21}$$

The velocity at a point $\mathbf{x}$ can be approximated by

$$\mathbf{u}(\mathbf{x}, t) = -\frac{1}{4\pi} \sum_{i=1}^{N} \sum_{j=1}^{n_i} \Gamma_i \frac{(\mathbf{x}^c_{i,j} - \mathbf{x}) \times (\mathbf{x}_{i,j+1} - \mathbf{x}_{i,j})}{|\mathbf{x}^c_{i,j} - \mathbf{x}|^3} f(\frac{|\mathbf{x}^c_{i,j} - \mathbf{x}|}{\delta}), \tag{2.22}$$

which is a discrete version of (2.15).

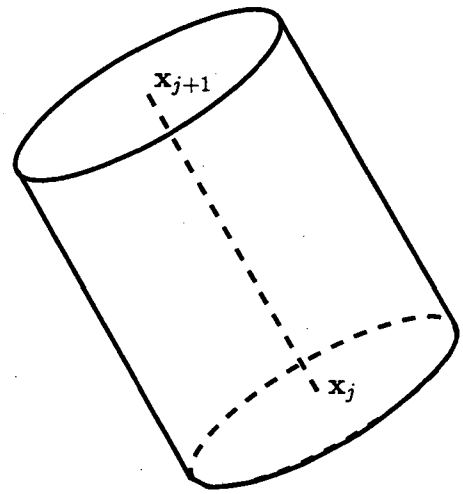

Figure 2.4: A vortex segment.

Once the velocity $\mathbf{u}(\mathbf{x}_{i,j})$ is calculated from the numerical filament configuration, one can advance $\mathbf{x}_{i,j}$ by solving an initial value problem :

$$\frac{d\mathbf{x}}{dt} = \mathbf{u}(\mathbf{x}). \tag{2.23}$$

If only one numerical filament is used instead of a collection of overlapping numerical filaments to approximate the vorticity field, the resulting method is called the *thin tube vortex filament method.* Later we will employ both the standard vortex filament method and the thin tube vortex filament method to study short wave instability.

Chapter 3

Instability of A Vortex Ring

In this chapter, we review some of Widnall's analysis of vortex ring instability. This review is important for our study of short wave instability on vortex filaments and our study of time and spatial discretization of vortex methods, which will be presented in the following chapters.

The behavior and inherent beauty of vortex rings have fascinated researchers for a long time (e.g. [48], [63], [69]). In nature, vortex rings are found to occur in various sizes. Perhaps the most familiar example is the smoke-ring which is produced when smoke is ejected suddenly through the lips of a smoker. Vortex rings have also been observed in the wakes of aircrafts. In a laboratory, the usual method of generating vortex rings is to eject fluid impulsively through some type of orifice into a quiescent fluid. In superfluid helium, experiments by Rayfield and Reif [78] found that accelerating ions can create quantized vortex rings.

Part of the fascination of vortex rings stems from their compact and persistent nature. It was this persistence and their apparent stability that prompted Lord Kelvin to propose the theory of vortex ring atoms, which explained spectral lines in terms of different modes of oscillation of vortex rings. Even though this theory was later superseded, it inspired much of the early analysis of vortex rings that is still relevant today. The compactness of vortex rings simplifies analytical, numerical and experimental studies. However, their nature is still complex enough to have provided ample material for research for well over one hundred years.

While many studies of vortex rings have been prompted by scientific curiosity, some studies have been made of technological applications. For example, vortex rings have

been suggested as a means for extinguishing gas and oil well fires [1] and cavitating vortex rings, produced by exciting cavitating jets, have been used for underwater cleaning and rock cutting [14].

The simple and robust nature of vortex rings also makes them ideal as simpler building blocks in the modeling of more complex flows, including the generation of sound, mixing in shear layers, and turbulence. Among many interesting arena of vortex rings, we are concerned with the stability of vortex rings. In this chapter we discuss some of the features of vortex ring instabilities. First we give a historical review of the study of vortex ring instabilities. Then we describe the theoretical study of vortex ring instabilities, which plays a guiding role in the later chapters of this thesis.

3.1 Historical Review of the Study of Vortex Ring Instabilities

Theoretical studies in the late 1800s suggested that wave-like perturbations on vortex rings were stable. Analyses of vortex rings, carried up through terms of $O(\delta/R)$, showed no instability. However, about half a century later, the experimental work of Krutzsch [59] showing the formation of unstable azimuthal waves on vortex rings brought these findings into questions. The significance of his observations was not fully appreciated at the time and it was not until Maxworthy [68] observed a similar azimuthal instability that researchers began to examine this phenomenon closely.

Maxworthy's experiments [68] revealed that a stable laminar vortex ring forms when the Reynolds number (based on the velocity and the diameter of the ring) is less than 600. Once formed, the ring does not translate with a constant velocity, as might be expected from inviscid theory, instead the velocity decays (Maxworthy [68], Sallet and Widmayer [83], and Glezer and Coles [39]). At moderate Reynolds number, experimental data indicate that a laminar vortex ring may subsequently become "turbulent".

Since Maxworthy's observation on vortex ring instabilities, a number of experimental studies have been made of this phenomenon (Widnall and Sullivan [96]; Leiss and Didden [61]; and Auerbach [5]). A detailed explanation of this phenomenon has gradually developed as the result of several studies.

In 1973 Widnall and Sullivan [96] investigated the stability of vortex rings both

theoretically and experimentally. They attempted to explain the instability by considering the behavior of an inviscid circular vortex filament with a thin core (as $\delta/R \rightarrow 0$). They examined the behavior of a small perturbation in the induced velocity field of the ring. A perturbation may grow, die out, or remain unchanged with time. Perturbations of different wavelengths will have different growth rates. In their analysis Widnall and Sullivan assumed that the wavelength of the perturbation wave was large in comparison with the core radius (i.e. $k\delta << 1$, where k is the wave number defined as 2π/wave length), since for long waves, the self-induced rotation frequency of the sinusoidal wave on a straight vortex filament has a simple asymptotic formula. Their analysis suggested that a thin vortex ring in an ideal fluid is almost always unstable to a small wave-like perturbation.

The approach of Widnall and Sullivan [96] had some success in predicting the amplification rates and mode shape of the instability. Their results were in agreement with their experimental measurements. They also showed that the number of waves around the perimeter in the unstable mode depends on the size of vortex core. For a given vortex core, only one mode is unstable and the wave number of the unstable mode increases with decreasing core size. Nevertheless, their prediction of the wave number was not accurate. As Widnall and Sullivan pointed out, the wavelength of the predicted unstable mode is of the order of the core size and, as a result, contradicts the assumption of long waves used in the analysis.

In order to address this shortcoming in the model of Widnall and Sullivan, Widnall et al. [95] proposed a new model in which it is possible for the wavelength of the unstable mode to be comparable with the size of the vortex core. In this modified model, they still examine the asymptotic limit of a thin core ($\delta/R \rightarrow 0$); however, here the wavelength of the perturbation is such that $k\delta$ is of order one, whereas in the previous case $k\delta << 1$ (as $\delta/R \rightarrow 0$).

The improved model relies on the important observation that the induced velocity on a displaced portion of the vortex ring due to the rest of the vortex ring is locally like a stagnation point flow (in the case of a perturbed vortex pair it is an exact stagnation point flow, however, in the case of a curved filament or ring the flow is only approximately like a stagnation point flow). This means that the perturbed filament is subject to a local plane straining. Widnall argued that if the perturbation is aligned with the strain, it will grow. However, a sinusoidal perturbation on a vortex filament is also subject to rotation due to its self-induced velocity field. Thus the problem is to find cases where the combination of

these two effects results in a perturbation which remains aligned with the strain. In their model, Widnall et al [95] considered one case in which this is automatically true, that is perturbations for which the self-induced rotation frequency is zero. They found that the first radial mode can not have a zero rotation frequency, and that it is the higher radial mode (second or higher) that is responsible for the instability. In their previous work, a spurious non-rotating first radial mode was predicted by the asymptotic formula for long waves outside its valid region.

In two subsequent papers Tsai and Widnall [92] and Widnall and Tsai [97] refined the ideas presented in Widnall et al. [95].

In particular, Tsai and Widnall [92] addressed the effect of the distortion of the core by the imposed strain. In addition to the modes with zero rotation frequency, two helical modes of opposite rotation frequency were included in their model. These two helical waves, when superposed, form a standing wave (the existence of these modes for a straight filament was pointed out by Moore and Saffman [74]). They also attempted to justify the assumption that it is the second radial mode that dominates over the higher radial modes. In this they were unsuccessful — they found that the second and third radial modes have similar amplification rates.

Widnall and Tsai [97] examined the effect of curvature using matched asymptotic expansions to order δ^2 for the frequencies of oscillations. They showed that the effects of curvature are much smaller than that of strain and therefore the mechanism of Widnall et al. [95] is basically correct.

The mechanism Widnall and her co-workers used to study short wave instabilities on a vortex ring is very technical and illustrative. We will use a similar mechanism to study short wave instabilities on a co-rotating vortex pair and short wave instabilities on vortex filaments of fixed core structure in a straining flow in Chapter 6. In the following section we restrict our attention to the study of vortex ring instabilities.

3.2 Vortex Ring Instabilities

In this section we briefly introduce the model for the experimentally observed instability of the vortex ring, which is subject to perturbations of azimuthal bending waves whose wavelength is comparable with the core size of the vortex ring. We shall closely follow the approach presented in Widnall et al. [95] where the short wave instability is studied for

both the vortex ring and the vortex pair. Instability for both the vortex ring and the vortex pair is predicted to occur when the waves on the filament have zero self-induced rotation frequency. This zero rotation frequency does not occur for the first radial bending mode of a vortex filament. However, it does occur for higher radial bending modes which have more complex radial structures with at least one node at some radius within the core of the filament. Here the word "node" represents a radius r_0 such that the disturbance velocity vanishes on the circle of radius $r = r_0$.

3.2.1 Vortex Pair Instability

To motivate the more complete stability analysis for the vortex ring, we first investigate the instability of a thin vortex pair. A thin vortex pair consists of two parallel vortex filaments of opposite circulation where the core size of each filament is small compared with the distance between the filaments. As shown in Figure 3.1, axes are taken with x span-wise, y horizontally outwards and z parallel to the undisturbed straight filament. The undisturbed pair moves inwards with velocity $\Gamma/2\pi b$, where b is the separation between two unperturbed filaments, and $\pm\Gamma$ is their circulation.

The instability of the vortex pair to bending wave perturbation was first considered by Crow [35]. Since the flow outside the vortex filament is potential, the stability calculation can be done by considering the motion of the filaments that results from the perturbation. To do this, we shift the coordinate system such that the origin coincides with one of the unperturbed filaments. Figure 3.2 shows a cross section of the vortex pair with the coordinate system. The vortex filaments move with a velocity that is a combination of the velocity induced by the other filament and the self-induced rotation Ω of the sinusoidally perturbed filament. For short waves, it is the presence of the neighboring filament rather than the perturbation on that filament that plays the dominant role in the instability. The presence of the other filament produces a stagnation-point flow in the neighborhood of the vortex, whereas the velocity induced at the vortex due to short wave perturbation of the other filament can be ignored.

The velocity at a point (x, y) induced by the other filament is

$$\mathbf{u}(x,y) = \frac{\Gamma}{2\pi}\frac{1}{(b+x)^2+y^2}\begin{bmatrix} y \\ -(b+x) \end{bmatrix}. \tag{3.1}$$

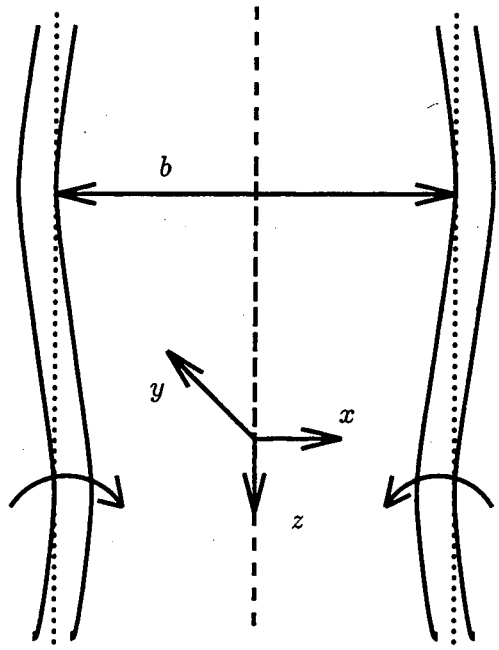

Figure 3.1: A perturbed vortex pair of opposite circulation.

Expanding **u** around $(0,0)$ yields

$$\mathbf{u}(x,y) = \frac{\Gamma}{2\pi b^2}\begin{bmatrix} 0 \\ -b \end{bmatrix} + \frac{\Gamma}{2\pi b^2}\begin{bmatrix} y \\ x \end{bmatrix} + O(x^2+y^2). \tag{3.2}$$

The second term on the right hand side of expression (3.2) is a stagnation point flow. It represents the velocity of the perturbed vortex at (x,y) relative to the unperturbed vortex position $(0,0)$, which is induced by the other filament. The stagnation point flow is sketched in Figure 3.2

In the local cylindrical (r,θ) coordinate system centered at the unperturbed position of the vortex filament, this stagnation-point (SP) flow has the following form:

$$u_r(SP) = \frac{\Gamma}{2\pi b^2} r \sin 2\theta, \tag{3.3}$$

$$u_\theta(SP) = \frac{\Gamma}{2\pi b^2} r \cos 2\theta, \tag{3.4}$$

where $u_r(SP)$ is the radial velocity and $u_\theta(SP)$ is the tangential velocity. Therefore, for the vortex cross-section which is at the position (r_0,θ_0), the velocity due to the stagnation

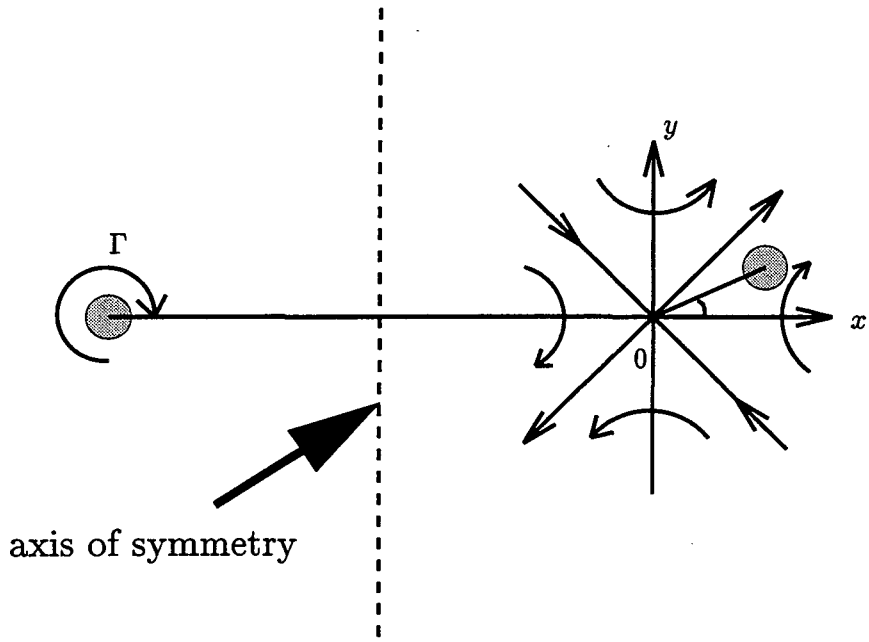

Figure 3.2: A cross-section of the vortex pair.

flow is

$$u_{r_0}(SP) = \frac{\Gamma}{2\pi b^2} r_0 \sin 2\theta_0, \tag{3.5}$$

$$u_{\theta_0}(SP) = \frac{\Gamma}{2\pi b^2} r_0 \cos 2\theta_0. \tag{3.6}$$

In addition to these components of velocity induced by the other filament, the displaced portion of the filament is also subject to its self-induced rotation (SR) around the unperturbed position $(0, 0)$. The self-induced tangential velocity is

$$u_{\theta_0}(SR) = r_0 \Omega, \tag{3.7}$$

where Ω is the rotation frequency of the perturbation wave. For long waves (i.e. the wavelength is much larger than the core size $k\delta << 1$) on a straight vortex filament with constant vorticity distribution, the frequency Ω has an asymptotic formula given by Lord Kelvin [49]

$$\Omega = -\frac{\Gamma}{4\pi} k^2 [\ln(\frac{1}{k\delta}) + \frac{1}{4} + \ln 2 - \gamma], \tag{3.8}$$

where γ is Euler's constant 0.5772.... For short waves, Ω has to be solved numerically from a transcendental equation (dispersion relation) and will be discussed later.

The combination of the stagnation point flow field and the self-induced rotation gives the total velocity of the vortex cross-section relative to the unperturbed position. We expect instability to occur when

$$\min_{\theta} u_\theta(SP) \leq -u_{\theta_0}(SR) \leq \max_{\theta} u_\theta(SP), \tag{3.9}$$

that is, when the velocity field of the stagnation point flow is sufficient to overcome the self-induced rotation. The argument goes as follows. When the self-induced rotation velocity falls between the minimum and maximum tangential velocity of the stagnation point flow, the total tangential velocity will carry the vortex cross-section to a new angle θ', where the total tangential velocity satisfies $u_{\theta'}(SP)+u_{\theta'}(SR) = 0$. The new angle θ' should also have the property that if the vortex is moved away from θ' by a small angle, the total tangential velocity will force it back to θ'. This is equivalent to

$$\frac{\partial(u_\theta(SP) + u_\theta(SR))}{\partial\theta}|_{\theta=\theta'} < 0, \tag{3.10}$$

from which it follows that

$$\sin 2\theta' > 0. \tag{3.11}$$

Thus we only need to consider the situation where $u_{\theta_0}(SP) = -u_{\theta_0}(SR)$ and $\sin 2\theta_0 > 0$.

When $u_{\theta_0}(SP) = -u_{\theta_0}(SR)$, the perturbation will diverge along the direction of $\theta = \theta_0$ with velocity $u_{r_0}(SP)$ and the position of the vortex is governed by the ordinary differential equation

$$\frac{dr_0}{dt} = u_{r_0}(SP) = \frac{\Gamma}{2\pi b^2} r_0 \sin 2\theta_0 > 0. \tag{3.12}$$

Integrating equation (3.12) with respect to time, we get

$$r_0(t) = r_0(0)e^{\alpha_\omega t} = r_0(0)e^{\frac{\Gamma}{2\pi b^2}\sin 2\theta_0 t}, \tag{3.13}$$

where $\alpha_\omega = \frac{\Gamma}{2\pi b^2}\sin 2\theta_0$. Thus the perturbation diverges along the direction θ_0 with a non-dimensional amplification rate

$$\bar{\alpha}_\omega = \frac{\alpha_\omega}{\Gamma/2\pi b^2} = \sin 2\theta_0 > 0. \tag{3.14}$$

For the vortex pair, Widnall et al. [95] noted that $\bar{\alpha}_\omega \approx 0.8$ and θ_0 is somewhat greater than 45° for the most unstable long waves, whereas $\bar{\alpha}_\omega = 1$ and $\theta_0 = 45^o$ for the most unstable short waves ($\Omega = 0$). Here it should be pointed out that for long waves, the velocity at the vortex filament due to long-wave perturbations of the other filament is not negligible and

has to be taken into account. For short waves, the condition for the most unstable mode ($\Omega = 0$) requires that $\cos 2\theta_0 = 0$. Thus $\theta_0 = 45^o$ and it follows that $\bar{\alpha}_\omega = 1$.

From the discussion above, one can see that the self-induced rotation frequency Ω of the sinusoidal waves on a straight vortex filament determines whether or not a mode is stable, what the growth rate is, and which mode is most unstable. In the next subsection we shall focus our attention on the dispersion relation which relates Ω to wave number and core size.

3.2.2 Dispersion Relations

We now discuss the dispersion relation of the infinitesimal perturbations of a uniform rectilinear vortex filament.

To proceed, consider a straight circular vortex filament of radius δ parallel to the z-axis. In the cylindrical polar coordinate system (r, θ, z), the components of the unperturbed velocity field are $(0, V(r), W(r))$. We consider infinitesimal perturbations (u_r, u_θ, u_z), which satisfy the Euler equations linearized about the unperturbed flow and the incompressibility constraint. We search for solutions of the form

$$u_r = u(r)e^{i(kz+m\theta-\Omega t)}, \tag{3.15}$$

$$u_\theta = v(r)e^{i(kz+m\theta-\Omega t)}, \tag{3.16}$$

$$u_z = w(r)e^{i(kz+m\theta-\Omega t)}, \tag{3.17}$$

$$P = p(r)e^{i(kz+m\theta-\Omega t)}, \tag{3.18}$$

where P is the pressure. The axial wave number is k. m is the azimuthal wave number, which must be an integer. The solutions for Ω are the eigenvalues and the corresponding solutions for (u, v, w, P) are the eigenfunctions.

For a filament of uniform vorticity distribution with zero axial flow, the unperturbed velocity field $(0, V(r), W(r))$ is

$$W(r) = 0, \tag{3.19}$$

$$V(r) = \begin{cases} \Omega_0 r, & r \leq \delta \\ \Omega_0 \delta^2/r, & r > \delta \end{cases} \tag{3.20}$$

where

$$\Omega_0 = \Gamma/2\pi\delta^2 \tag{3.21}$$

is the angular velocity of the solid body rotation of the unperturbed vortex core. The dispersion relation which relates Ω to k, m and δ is the following transcendental equation (see Moore and Saffman [73]):

$$\frac{g^2}{4\Omega_0^2 - g^2}\left[\frac{\beta\delta J'_{|m|}(\beta\delta)}{J_{|m|}(\beta\delta)} + \frac{2m\Omega_0}{g}\right] = -\delta|k|\frac{K'_{|m|}(|k|\delta)}{K_{|m|}(|k|\delta)}, \tag{3.22}$$

where

$$g = -\Omega + m\Omega_0, \tag{3.23}$$

$$\beta^2 = k^2(4\Omega_0^2 - g^2)/g^2, \tag{3.24}$$

$J_{|m|}$ is the $|m|$-th order Bessel function of the first kind, and $K_{|m|}$ is the $|m|$-th order modified Bessel function of the second kind.

The nature of the disturbance depends dramatically on the value of azimuthal wave number m. The deformed core is given by

$$r = \delta + De^{i(kz+m\theta-\Omega t)}. \tag{3.25}$$

If $m = 0$, the disturbance is axisymmetric and is called bulge wave. For $|m| \geq 2$, the boundary of the vortex core is perturbed, but the core as an entity is not shifted. These modes are called shape-change waves. For example, when $m = 2$, by taking the real part of (3.25), one can see that the core cross-section is deformed into an ellipse which rotates around z axis. In the case of $m = 0$ or $|m| \geq 2$, we have $u = v = 0$ at $r = 0$, and the axis of the vortex is undisturbed. The modes with $|m| = 1$ are very special. They are called the bending modes and are the perturbations we will be concerned with. When $|m| = 1$, the axis of the vortex is deformed and the velocity perturbation does not vanish at $r = 0$. Again, taking the real part of (3.25) with $m = 1$ and assuming that D is real, one obtains a circle with center at $r = D$ in the direction $\theta = -(kz - \Omega t)$. This is a left-handed spiral (helical wave). Figure 3.3 shows the core cross-sections before and after the disturbance for the azimuthal wave number $m = 0, 1, 2, 3, 4, 5$, respectively.

Now we study the dispersion relation (3.22) for the bending waves, i.e. $|m| = 1$. From the symmetry of the equation (3.22), we know that

$$\Omega(k; m = 1) = \Omega(-k; m = 1) = -\Omega(k; m = -1). \tag{3.26}$$

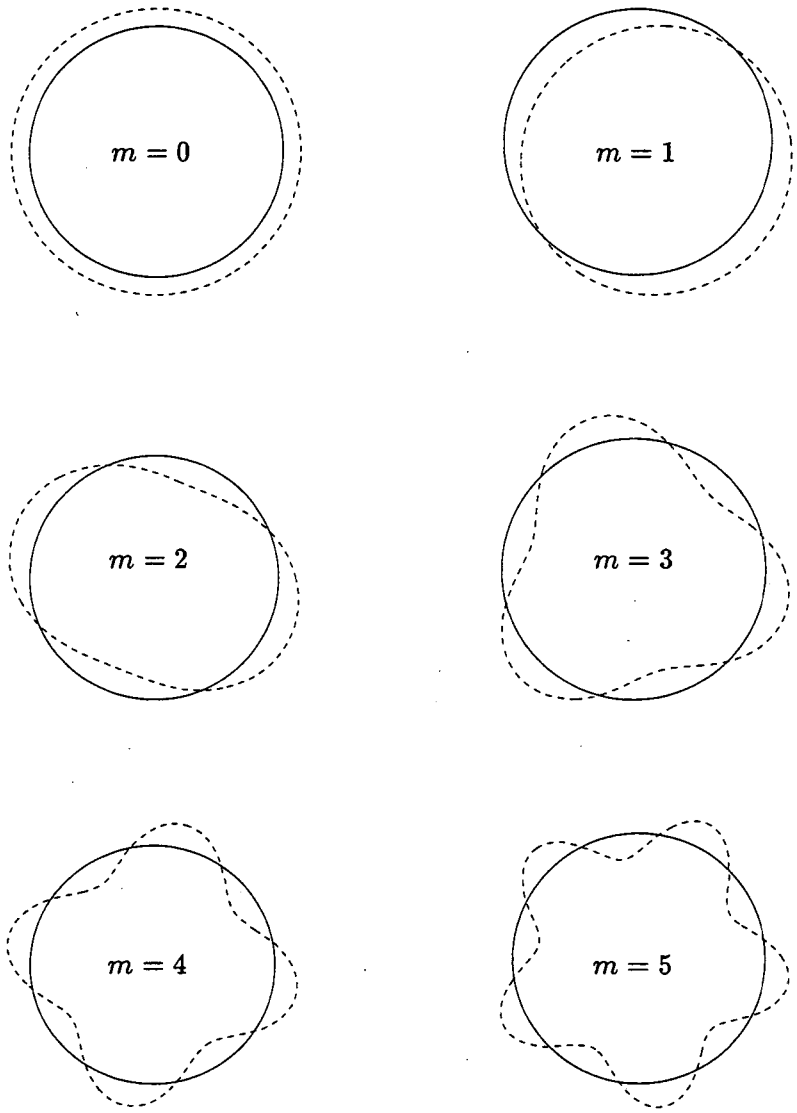

Figure 3.3: The core cross-sections before and after the perturbation for various azimuthal wave numbers. The solid curves denote the unperturbed core, the dashed curves denote the perturbed core.

Thus there is no loss of generality in taking k positive and $m = 1$. Solving g from equation (3.24), one has

$$g = \sqrt{\frac{4\Omega_0^2 k^2}{\beta^2 + k^2}} = \frac{2\Omega_0 k\delta s}{\sqrt{(\beta\delta)^2 + (k\delta)^2}}, \tag{3.27}$$

where $s = \pm 1$. When $s = 1$, as a result of equations (3.27) and (3.23), we have $\Omega < \Omega_0$, i.e. the rotation Ω of the disturbance is slower than or even in the opposite direction of the solid body rotation Ω_0 of the unperturbed vortex core. In this case, the disturbance is called retrograde. If $s = -1$, it also follows from (3.27) and (3.23) that the disturbance Ω rotates faster than the solid body rotation of the core Ω_0 and is called co-grade. For the co-grade modes, the rotation frequency Ω is of the same order as Ω_0, which is much larger than the maximum angular velocity of the stagnation point flow:

$$\Omega^{co-grade} \sim \Omega_0 = \frac{\Gamma}{2\pi\delta^2} >> \frac{\max_\theta u_\theta(SP)}{r}. \tag{3.28}$$

The inequality (3.28) holds because

$$\frac{\max_\theta u_\theta(SP)}{r} = \frac{\Gamma}{2\pi b^2} \tag{3.29}$$

from equation (3.4) and we have assumed that $\delta << b$. Since the unstable modes are those with zero or small rotation frequency (when the self-induced rotation can be overcome by the stagnation point flow), the co-grade modes are not candidates for unstable modes and will not be discussed here.

Taking $s = 1$, $m = 1$, and substituting (3.27) into equation (3.22) gives a transcendental equation for β:

$$\frac{1}{\beta\delta}\frac{J_1'(\beta\delta)}{J_1(\beta\delta)} + \frac{\sqrt{(\beta\delta)^2 + (k\delta)^2}}{(k\delta)(\beta\delta)^2} = -\frac{K_1'(k\delta)}{k\delta K_1(k\delta)}. \tag{3.30}$$

The left hand side and the right hand side are sketched as functions of $\beta\delta$ in Figure 3.4, which shows that for any $k\delta$, equation (3.30) has infinite number of roots $\{(\beta\delta)_n, n = 1, 2, 3, ...\}$.

Combining equation (3.27) and equation (3.23), one can see immediately that for any $k\delta$, the dispersion relation (3.22) also has infinite number of roots $\{\Omega_n, n = 1, 2, 3, ...\}$, given by

$$\Omega_n = \Omega_0 - g_n = \Omega_0 - \frac{2\Omega_0 k\delta}{\sqrt{(\beta\delta)_n^2 + (k\delta)^2}}. \tag{3.31}$$

These roots Ω_n are the eigenvalues of the linearized Euler equations. They are the rotation frequencies of the corresponding eigenfunctions (disturbances) which are called the first radial mode ($n = 1$), the second radial mode ($n = 2$) and so on.

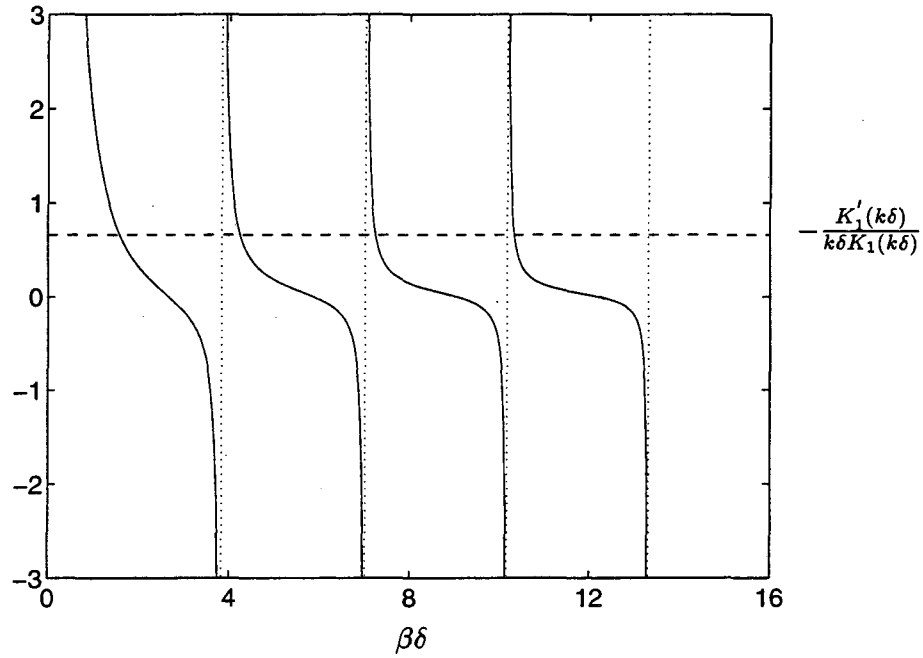

Figure 3.4: The left hand side (solid curve) and the right hand side (dashed curve) of equation (3.30) as functions of $\beta\delta$.

In the long wave limit $k\delta \to 0$, the right hand side of equation (3.30) $-\frac{K_1'(k\delta)}{k\delta K_1(k\delta)}$ is asymptotically $\frac{1}{(k\delta)^2}$, which implies that the n-th root $(\beta\delta)_n$ of equation (3.30) converges to the n-th root j_n of $J_1(x) = 0$. Therefore, as $k\delta$ goes to zero, the n-th root Ω_n of the dispersion relation given by (3.31) approaches Ω_0, except for the first root Ω_1 which has a different behavior because the first root j_1 of $J_1(x)$ is zero. When $k\delta$ is small (long waves), the first root $(\beta\delta)_1$ of equation (3.30) is also small and the rotation frequency Ω_1 of the first radial mode has a simple asymptotic formula which is given below.

For both $k\delta$ and $\beta\delta$ small, the two terms in equation (3.30) which involve the Bessel functions J_1 and K_1 can be expanded into the power series:

$$\frac{1}{\beta\delta}\frac{J_1'(\beta\delta)}{J_1(\beta\delta)} = \frac{1}{(\beta\delta)^2} - \frac{1}{4} + O(\beta^2\delta^2), \tag{3.32}$$

$$-\frac{1}{k\delta}\frac{K_1'(k\delta)}{K_1(k\delta)} = \frac{1}{(k\delta)^2} + [\log(\frac{1}{k\delta}) - \gamma] + O(k^2\delta^2), \tag{3.33}$$

where γ is Euler's constant as before. Substituting (3.32) and (3.33) into equation (3.30),

assuming $\beta\delta$ is of the form $c_1(k\delta) + c_2(k\delta)^3$ and solving for c_1 and c_2, we obtain

$$\beta\delta = \sqrt{3}\left\{k\delta - \frac{2}{3}[\log(\frac{2}{k\delta}) + \frac{1}{4} - \gamma](k\delta)^3\right\} + O(k^5\delta^5). \tag{3.34}$$

Combining (3.34) and (3.27) yields

$$\begin{aligned}\Omega = \Omega_0 - g &= \Omega_0 - \frac{2\Omega_0(k\delta)}{\sqrt{(\beta\delta)^2 + (k\delta)^2}} \\ &= -\frac{1}{2}\Omega_0 k^2\delta^2[\log(\frac{2}{k\delta}) + \frac{1}{4} - \gamma].\end{aligned} \tag{3.35}$$

Equation (3.35) is the asymptotic formula for the rotation frequency of long waves of the first radial mode [49].

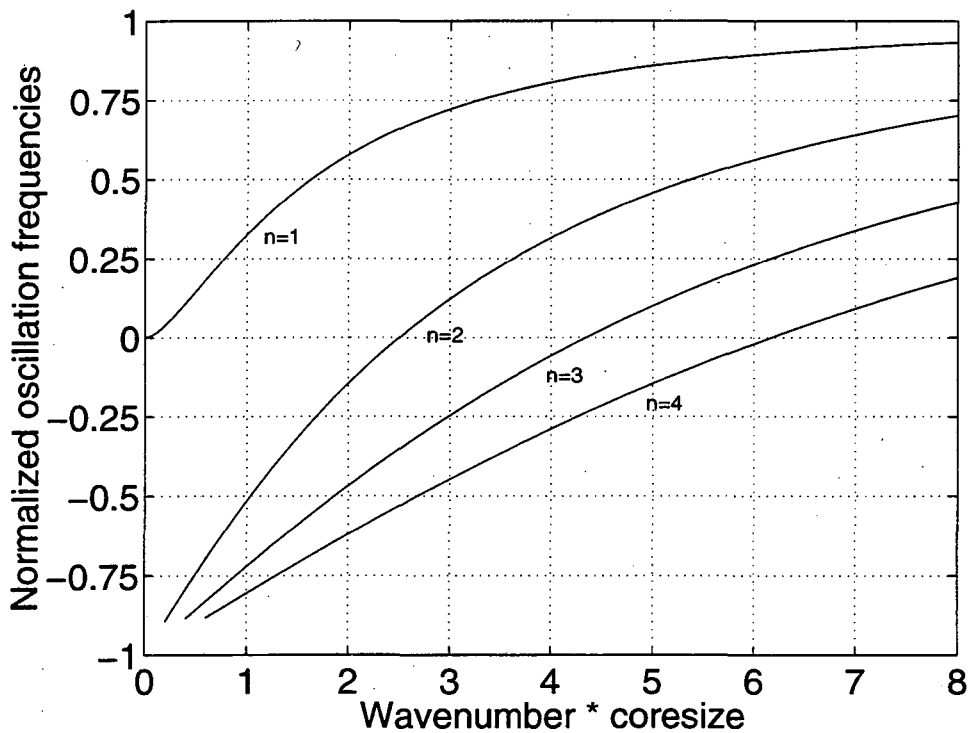

Figure 3.5: Oscillation frequencies of the first four radial modes on a filament with constant vorticity.

The rotation frequencies Ω of the first four radial modes on a vortex filament with constant vorticity are calculated numerically from the dispersion relation (3.22) and plotted as functions of $(k\delta)$ in Figure 3.5. It is important to notice that there are non-zero wave numbers for which the rotation frequency is zero. The zero rotation frequency is not possible for the lowest radial mode (the wave with wave number equal to zero is not an

interesting case here), however it does occur for the more complicated higher radial modes. If the rotation frequency Ω is zero, then equation (3.27), together with equation (3.23), yields

$$\beta\delta = \sqrt{3}k\delta \tag{3.36}$$

and the value of $(k\delta)$ can be obtained by solving the equation

$$\frac{1}{\sqrt{3}k\delta}\frac{J_1'(\sqrt{3}k\delta)}{J_1(\sqrt{3}k\delta)} + \frac{2}{3k^2\delta^2} = -\frac{1}{k\delta}\frac{K_1'(k\delta)}{K_1(k\delta)}. \tag{3.37}$$

The values of $(k\delta)$ corresponding to non-rotating second, third and fourth radial modes are 2.5, 4.4 and 6.2, which can also be seen from Figure 3.5.

In Figure 3.6 we compare the exact and the asymptotic dispersion relations for waves on a vortex filament with constant vorticity. It is clear that the asymptotic formula should not be used for $k\delta$ not small (short waves). In particular, the zero rotation frequency predicted by the asymptotic formula (3.35) at $k\delta = 2e^{\frac{1}{4}-\gamma} = 1.44$ is spurious. This is not surprising, since the predicted $k\delta$ is far away from the valid region of the asymptotic formula ($k\delta << 1$.)

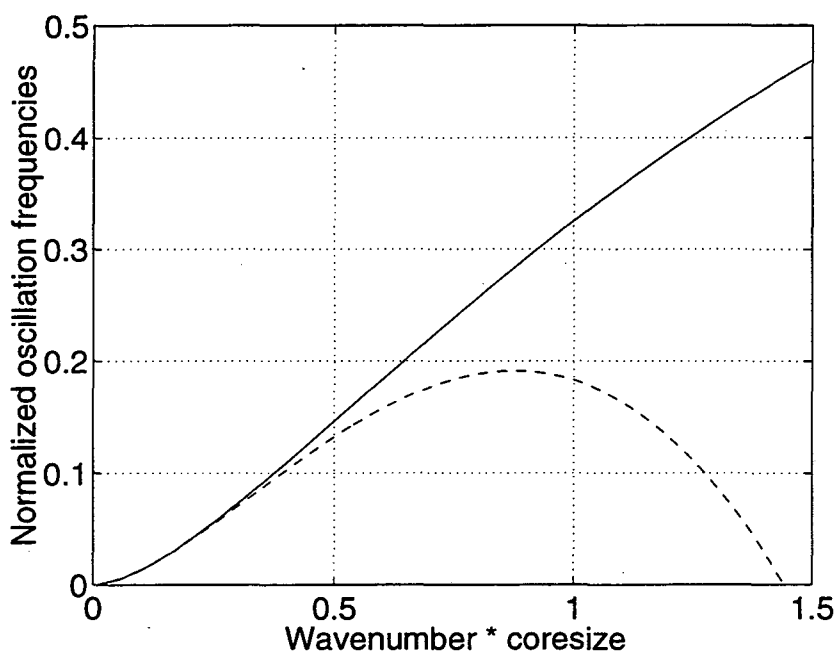

Figure 3.6: Comparison of the exact (solid line) and asymptotic (dashed line) dispersion relations for waves on a vortex filament with constant vorticity.

Higher radial modes have more complicated radial structure in the sense that they have at least one node at some radius within the core of the filament. In the first mode, the inner and outer crests of the disturbance translate in the same direction and thus there are no nodes within the core. In the second radial mode, the outer and inner crests of the disturbance translate in opposite directions and thus there is one node in the core.

Figure 3.7 shows the radial velocities at various locations for the first and the second radial modes. Note that the radial velocity also depends on the angle θ through $u_r = u(r)\cos\theta$. So the radial velocity at $\theta + \pi$ is exactly the opposite of that at θ.

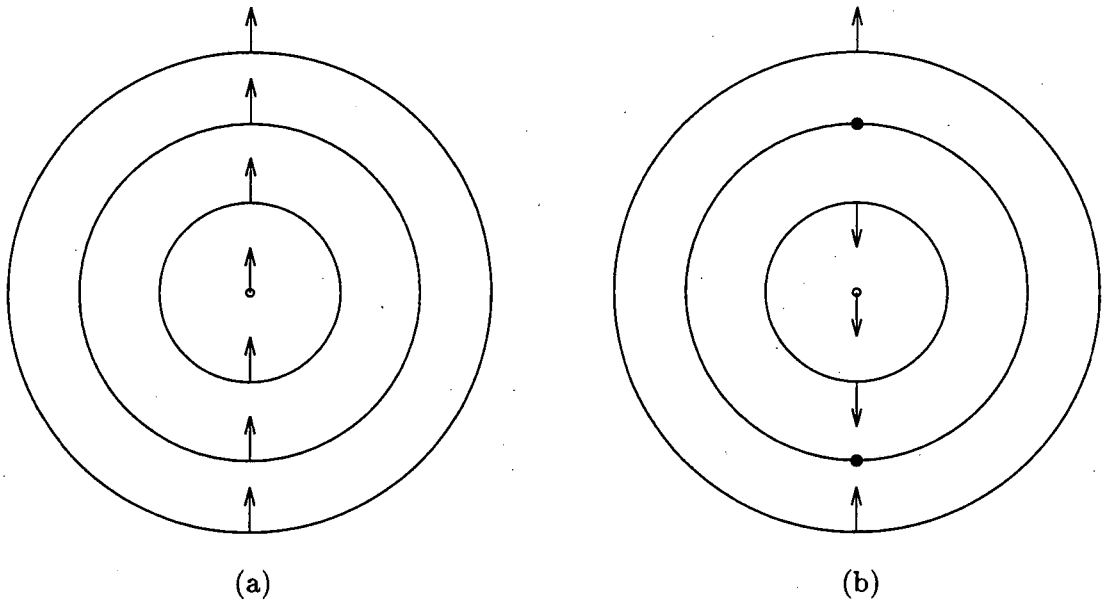

Figure 3.7: Radial velocities at various locations for the first (a) and the second (b) radial modes.

For the vortex pair of constant vorticity distribution, we conclude that the most unstable waves are those with zero rotation frequency. Short waves of the first radial modes are always stable. For the second radial mode, the most unstable wave satisfies $k\delta = 2.5$ while for the third radial mode, it occurs at $k\delta = 4.4$.

3.2.3 Vortex Ring Instability

The purpose of this subsection is to examine the stability of the vortex ring to azimuthal bending waves of wavelength comparable to the core size.

In the limits $\delta/R \to 0$ and $kR \to \infty$, to the lowest order, sinusoidal waves on a slender bent filament will rotate around the filament at the same frequency as if they were on a straight filament. Here R denotes a typical radius of curvature of the filament curve. For short waves on a thin vortex ring, we have $k\delta \sim O(1)$ and $kR = k\delta(\frac{R}{\delta}) \to \infty$ as $\frac{\delta}{R} \to 0$. Hence the self-induced rotation frequencies of short waves on a thin vortex ring are approximately the roots of the dispersion relation (3.22), which have been shown as functions of $k\delta$ in Figure 3.5. Here the self-induced rotation is due to the velocity induced by a part of perturbed ring, the length of which is small in comparison with the circumference of the vortex ring but large in comparison with the wavelength. One can analyze the vortex-ring instability in the same manner as the vortex-pair instability. That is to examine whether or not the self-induced rotation can be balanced by the stagnation point flow at the vortex due to the presence of and the perturbations on the remainder of the ring. The part of the vortex ring which is responsible for the self-induced rotation and the remainder of the ring are sketched in Figure 3.8.

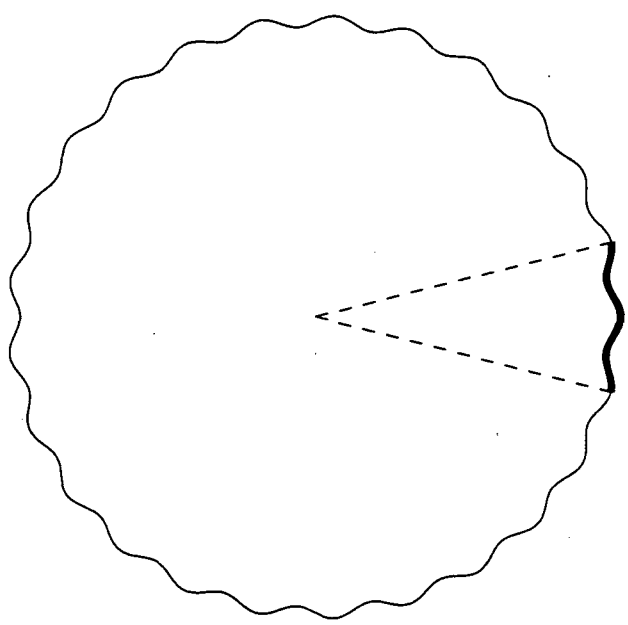

Figure 3.8: Thick curve: the part of the filament curve responsible for the self-induced rotation of the waves around the ring; thin curve: the remainder of the ring.

We expect that for short waves, such as those unstable waves observed on vortex rings, the velocities induced at the core boundary due to perturbations on the remainder of

the ring are negligible. Bliss [12] expanded the velocity field near a vortex filament ring. As in the vortex-pair instability previously discussed, the terms that are relevant to the vortex ring instability are the stagnation point flow induced in the neighborhood of the vortex core by the presence of the ring. From Bliss's analysis, the radial and tangential velocity components of this flow are given by

$$u_r = \frac{\Gamma}{4\pi R^2}\frac{3}{4} r \sin 2\theta [\ln \frac{8R}{r} - \frac{4}{3}], \tag{3.38}$$

$$u_\theta = \frac{\Gamma}{4\pi R^2}\frac{3}{4} r \cos 2\theta [\ln \frac{8R}{r} - \frac{5}{6}]. \tag{3.39}$$

The velocity field (3.38) and (3.39) for the vortex ring is analogous to the field (3.3) and (3.4) for the vortex pair. Strictly speaking, due to the presence of the term $\ln r$ and the different constants inside the brackets for u_r and u_θ, the velocity field (3.38) and (3.39) is not exactly a stagnation point flow.

To illustrate the essential mechanism in the vortex-ring instability, we consider the net translational motion of a cylinder of radius δ, representing the vortex core boundary, displaced in this field. Because of the presence of the logarithm in the velocity field, to evaluate the net translational velocity, we require that the displacement of the vortex core boundary be small in comparison with the core radius (this is true for infinitesimal perturbations). In the appendix of [95], Widnall et al. showed that the net translation of the cylinder of radius δ perturbed in the "stagnation point" flow (3.38) and (3.39) is given by

$$u_{r_0} = \frac{\Gamma}{4\pi R^2}\frac{3}{4} r_0 \sin 2\theta_0 [\ln \frac{8R}{\delta} - \frac{25}{12}], \tag{3.40}$$

$$u_{\theta_0} = \frac{\Gamma}{4\pi R^2}\frac{3}{4} r_0 \cos 2\theta_0 [\ln \frac{8R}{\delta} - \frac{25}{12}]. \tag{3.41}$$

These expansions are of the same form as the expressions in (3.5) and (3.6) which are used in the discussion of the vortex-pair instability.

We now suppose that instability of the vortex ring to short-wave perturbations around the azimuth occurs whenever the self-induced rotation Ω of the waves can be overcome by the net translational velocity (3.40) and (3.41). If the self-induced rotation Ω is zero, the rotation will stop at $\theta_0 = 45^o$, where $u_{\theta_0} = 0$, and the vortex will diverge at a velocity u_{r_0} given by (3.40). The growth rate u_{r_0} is maximized at the angle $\theta_0 = 45^o$.

We take as the condition for instability that $\Omega = 0$ for some $k\delta$. From Figure 3.5 it can be seen that zero rotation frequency $\Omega = 0$ is possible only for the second and higher radial modes. Assuming that the lowest of these modes (i.e. the second mode) is the

most likely to occur, one can draw the conclusion that the wave number k of the instability satisfies $k\delta = 2.5$ for a uniform distribution of vorticity in the core. This theoretical result agrees well with the experimental results of Widnall and Sullivan [96].

In summary, we have reviewed Widnall's study of vortex ring instabilities. In the next chapter we will carry out a numerical study of the problem.

Chapter 4

Numerical Results Obtained with the Thin Tube Vortex Filament Method

In this chapter numerical simulations are carried out for the problem of vortex ring instability. The numerical method used here is the vortex method with one numerical vortex filament, which is called the thin tube vortex filament method. In this method, the cross section of the physical vortex filament, with core radius σ, is represented by one numerical vortex filament with core radius $\delta = \sigma$. In effect, the core structure of the physical vortex filament is fixed. The thin filament approximation of vorticity structures has been employed before in many numerical simulations. For example, Chorin [22] has used this method to follow the evolution of a turbulent vortex; Siggia [89] has applied it to simulate the collapse and amplification of a vortex filament; Pumir and Siggia [76] have used it to study the existence of solutions to the Navier-Stokes equations. Several years ago, Knio and Ghoniem [57] investigated the accuracy and convergence of this method by comparing numerical solutions to analytical results on the propagation and stability of vortex rings. In this chapter we will modify some of their results.

In the first section we present a static simulation of the velocity of a vortex ring. The goal of this section is to demonstrate that for a reasonable approximation of the vortex ring velocity, a certain condition should be satisfied by the spatial discretization.

In the second section, we further show that the criterion discussed in the first sec-

tion cannot be simply extended to other numerical simulations. We compare our numerical results with those obtained by Knio and Ghoniem [57] who used a similar method. The significant differences in the behaviors of the numerical results are evident. In particular, the neutrally stable (i.e. non-rotating and stable) wave found by Knio and Ghoniem is inconsistent with Widnall's stability theory which has been reviewed in the previous chapter. According to Widnall's theory, a wave is unstable when the self-induced rotation is balanced by the stagnation point flow induced by the ring (i.e. when it is not rotating). We find that the neutrally stable wave is actually caused by the underresolved spatial mesh size. With refined meshes, the wave is rotating and stable. Furthermore, contrary to Knio and Ghoniem's results, for thin vortex rings the unstable mode does not grow without bound, instead it exhibits a periodic behavior in time.

The mechanism of the instability and the periodic behavior in time of the unstable mode is explained in detail in the third section with the help of the dispersion relation for sinusoidal waves on a vortex filament with fixed core structure. Our analysis supports our numerical results.

At the end of this chapter, we summarize our work and draw some conclusions.

4.1 Static Simulation of the Velocity of A Vortex Ring

In this section, we use the thin tube vortex filament method to calculate the translational velocity of an unperturbed vortex ring.

The vortex ring, of radius R, is divided along its circumference into N vortex segments, each of length $h = (\delta \mathbf{x})_i = 2\pi R/N$, $i = 1, 2, ..., N$. The core radius σ of the vortex ring is used as the numerical core size δ and the velocity smoothing function is taken as

$$f(r) = 1.0 - e^{-r^3} \tag{4.1}$$

which has been shown to yield a second order discretization by Beale and Majda [8].

In the absence of viscosity, a thin vortex ring (the inner radius σ is small in comparison with the outer radius R) propagates at a constant rate along its axis of symmetry. The velocity of translation is asymptotically [82]

$$V = \frac{\Gamma}{4\pi R}\left[\log(\frac{8R}{\sigma}) + C\right], \tag{4.2}$$

where Γ is the circulation of the ring, and the constant C depends on the distribution of vorticity within the ring. For the velocity smoothing function given in equation (4.1), in the limit $h \to 0$, the numerical vorticity distribution is given by

$$\omega(\mathbf{x}) = \frac{\Gamma}{\delta^3} \int_{\text{ring}} g(\frac{|\mathbf{x} - \mathbf{x}(s)|}{\delta}) \mathbf{x}'(s) ds, \tag{4.3}$$

where
$$g(r) = \frac{f'(r)}{4\pi r^2} = \frac{3}{4\pi} e^{-r^3} \tag{4.4}$$

represents the vorticity distribution of a vortex element with unit cut-off radius and unit vorticity. For this vorticity distribution, the constant C in equation(4.2) is -0.50074. For a second order Gaussian vorticity distribution, $C = -0.558$.

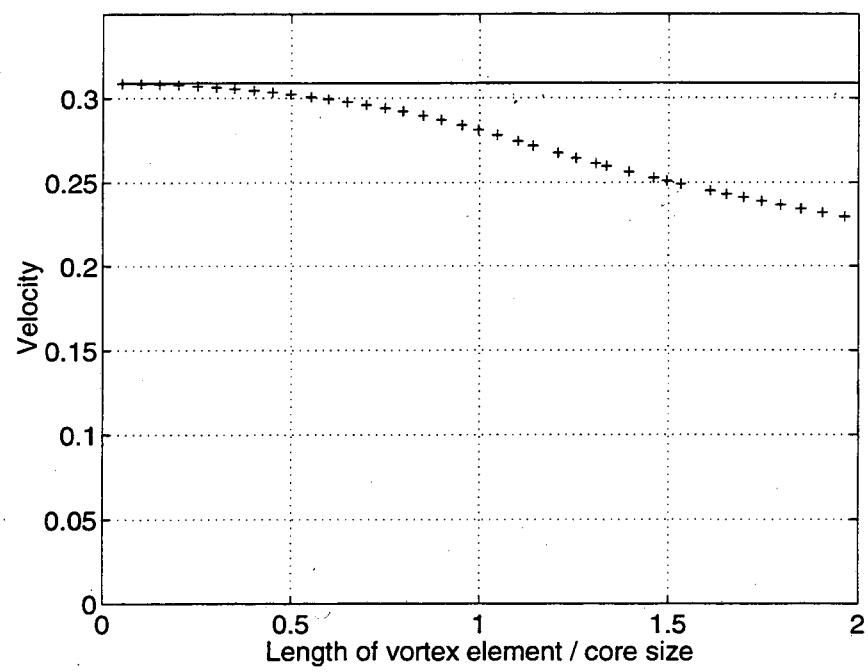

Figure 4.1: Comparison of the numerical velocity and the asymptotic velocity of a vortex ring. Here the "+" denotes the numerical velocity while the solid line denotes the asymptotic velocity.

The numerical velocity, obtained by summing the velocities induced by all vortex elements around the ring, is

$$V_{\text{numerical}} = -\frac{\Gamma}{4\pi} \sum_{i=1}^{N} \frac{(\mathbf{x} - \mathbf{x}_{i+\frac{1}{2}}) \times \delta \mathbf{x}_{i+\frac{1}{2}}}{|\mathbf{x} - \mathbf{x}_{i+\frac{1}{2}}|^3} f(\frac{|\mathbf{x} - \mathbf{x}_{i+\frac{1}{2}}|}{\delta}), \tag{4.5}$$

where $\mathbf{x}_{i+\frac{1}{2}} = \frac{1}{2}(\mathbf{x}_i + \mathbf{x}_{i+1})$ is the center of the i-th vortex element and $\Gamma\delta\mathbf{x}_{i+\frac{1}{2}}$ is the vorticity carried by the i-th vortex element.

In Figure 4.1, we compare the asymptotic velocity of the vortex ring V with the numerical velocity $V_{\text{numerical}}$ for different values of h/δ. The calculation is done with $R = 1$, $\Gamma = 1$ and $\sigma = 0.1$. Figure 4.1 shows that when $h/\delta < 0.5$, the numerical velocity agrees well with the asymptotic velocity; when $h/\delta > 0.5$, the numerical velocity is inaccurate.

This numerical experiment of calculating the velocity of a vortex ring indicates that overlapping between neighboring vortex elements (i.e. $h \sim \frac{\delta}{2}$) is necessary for the accurate evaluation of V. However, it should be emphasized that $h \sim \frac{\delta}{2}$ may not be sufficient to yield correct results for other problems. As we will see in the following sections, such an empirical criterion is obviously insufficient for the numerical simulations of vortex ring instability.

4.2 Numerical Simulations of the Instability of Vortex Rings Subject to Perturbations of Azimuthal Waves.

The purpose of this section is to simulate the growth of small sinusoidal perturbations on a vortex ring using the thin tube vortex filament method.

We choose the same initial conditions as in [57]. At time $t = 0$, a cosine wave perturbation with amplitude ε and wave number n is imposed on the circumference of a vortex ring with radius R. The ring lies on the x-y plane, the z-direction being the streamwise direction. Let ρ denote the radial direction in the plane of the ring and θ be the azimuthal angle as shown in Figure 4.2. The size of the perturbation varies in the azimuthal direction as $\Delta\rho = \varepsilon\cos(n\theta)$. In other words, initially the perturbed ring can be described by the parametric equations:

$$\begin{cases} x = (R + \varepsilon\cos(n\theta))\cos(\theta), \\ y = (R + \varepsilon\cos(n\theta))\sin(\theta), \\ z = 0, \end{cases}$$

where $0 \leq \theta \leq 2\pi$.

We discretize the perturbed ring by dividing it into N pieces according to azimuthal angle. Each piece corresponds to an angle $\triangle\theta = 2\pi/N$ in the azimuthal direction. The length of vortex element h is approximately $\triangle\theta \cdot R$ (it is exactly $\triangle\theta \cdot R$ if the ring is

unperturbed). This yields a ratio $h/\delta = \frac{2\pi}{N}\frac{R}{\delta}$. In our numerical simulations, the initial discretization is specified by the ratio h/δ. Given a ratio h/δ, the number of vortex elements N is taken as the integer which is closest to $2\pi(\frac{R}{\delta})/(\frac{h}{\delta})$ and the increment in the azimuthal angle $\triangle\theta$ is $\frac{2\pi}{N}$. The numerical discretization of the initial condition is given by

$$\begin{cases} x_j = (R + \varepsilon\cos(nj\triangle\theta))\cos(j\triangle\theta), \\ y_j = (R + \varepsilon\cos(nj\triangle\theta))\sin(j\triangle\theta), \\ z_j = 0, \end{cases}$$

for $j = 1, 2, ..., N$.

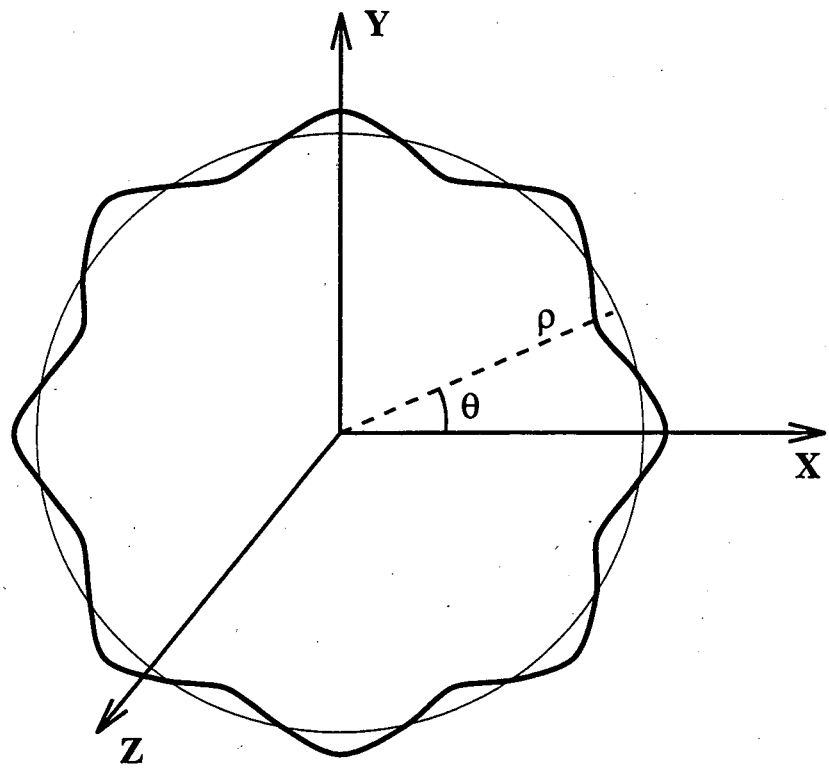

Figure 4.2: The perturbed vortex ring and the coordinate system

Besides the parameter h/δ, there is another parameter h_{cut} which affects the numerical representation of the filament during its evolution. When the length of the j-th vortex element $|\mathbf{x}_{j+1} - \mathbf{x}_j|$ is larger than h_{cut}, to keep a uniform numerical resolution, we cut the j-th element into two halves of equal length by adding a new point between the

nodes $\mathbf{x}_j$ and $\mathbf{x}_{j+1}$. The coordinates of the new point are obtained by linear interpolation. This process is repeated after each time step.

For time integration, a four stage fourth order Runge Kutta method is employed to advance the filament according to the velocity obtained by summing the contributions of all vortex elements. The time step is determined by $\Delta t = 4.0\delta^2/\Gamma$. The issue of ODE solver, time step and numerical stability is the major subject of next chapter.

In the following calculations, the radius of the ring is $R = 1$ and the selected value of circulation is $\Gamma = 1$. We start with the core size $\delta = 0.1R$ and the amplitude of the cosine wave perturbation $\varepsilon = 0.02R$. The evolution of the perturbation is analyzed in terms of its components in the radial and the streamwise directions.

For $n < n^*$, where n^* is the wave number of the unstable mode, the perturbation wave rotates around the unperturbed ring at a frequency Ω which depends on the wave number n. The trajectory of any point on the perturbed ring, observed relative to the unperturbed axis of the ring, is an ellipse whose major axis is in the radial direction and whose minor axis is in the streamwise direction. The rotation frequency Ω, starts low at small n, increases with n to a maximum, and then decreases as n approaches n^*. The sense of rotation of the perturbation wave is opposite to that of the vortex core rotation. The amplitudes in the ρ-direction and z-direction are shown in Figure 4.3 for wave numbers $n = 2$, 5, 8, 10, 12, and 13. The calculations are performed with $h/\delta = 0.05$, which is much smaller than the criterion $h/\delta < 0.5$ discussed in the first section of this chapter. We will come back to this issue later on. Figure 4.3 shows that as the wave rotates, the amplitudes in the ρ-direction and z-direction fluctuate periodically between a maximum and a minimum values. The maximum amplitude in the ρ-direction is the half length of the major axis of the ellipse traced out by the crest of the perturbation wave, while the maximum amplitude in the z-direction corresponds to the half length of the minor axis. These modes ($n < n^*$) are characterized as being stable. We will give a clear definition of "stable" and "unstable" modes at the end of this section.

At $n = n^*$ (for $\delta/R = 0.1$, the unstable wavenumber $n^* = 14$), the perturbation wave first rotates in the same direction as the vortex core rotation. After a while it reverses its rotation direction, then it reverses the rotation direction the second time and the perturbation wave goes back to its original position and starts to repeat the cycle. The net rotation around the unperturbed ring is not observed. The wave grows initially in both the radial and streamwise directions. After a while it continues growing in the radial direction

but decreases in the streamwise direction, then reverses the pattern and starts the cycle again. This mode is characterized as being unstable. Figure 4.4 illustrates the time evolution of the amplitudes in the ρ-direction and z-direction for the unstable mode $n = n^* = 14$ using $h/\delta = 0.05$.

For the higher values of n, $n > n^*$, the perturbation wave again rotates around the unperturbed ring at a frequency Ω. However, they behave quite differently from the case where $n < n^*$ in that the sense of rotation is now the same as that of the vortex core rotation and that the rotation frequency Ω grows monotonically with the wave number n. Another difference is that for $n > n^*$ the ellipse traced out by the rotating wave has its major axis in the streamwise direction and its minor axis in the radial direction. Figure 4.5 depicts the time histories of the amplitudes in the ρ-direction and z-direction for wave numbers $n = 15$, 16, 17, and 19. In the calculations, the discretization parameter h/δ is chosen as 0.05. These modes ($n > n^*$) are also characterized as being stable.

In their numerical experiments [57] Knio and Ghoniem obtained a neutrally stable mode. For $\delta/R = 0.1$ and $n = 13$, their results show that the perturbation wave neither rotates nor grows and the perturbation ring remains its original shape (see Fig. 3 in [57]). This conclusion contradicts Widnall's analysis which predicts that a mode becomes unstable when the rotation induced by the presence of the ring balances the self-induced rotation of the wave. Our calculations as plotted in Figure 4.3 show that for $\delta/R = 0.1$ and $n = 13$, the perturbation wave rotates in the opposite direction of the vortex core rotation and is stable, which matches Widnall's prediction.

For the unstable mode ($n = 14$ for $\delta/R = 0.1$), Knio and Ghoniem observed that the wave grows in the streamwise direction and then in the radial direction so that the total amplitude grows exponentially in time (see Fig. 4 in [57]). Our results in Figure 4.4 show that the wave grows first in both the streamwise and the radial directions, but the total amplitude does not grow without bound, rather it increases to a maximum and then decreases to its original value in a periodic fashion.

In order to determine the origin of these discrepancies between Knio and Ghoniem's results and ours, we ran the calculations with the discretization parameter $h/\delta = 0.35$, 0.2, 0.1, and 0.05. The amplitudes in the ρ-direction and the z-direction obtained with various discretization parameter h/δ's are drawn in Figure 4.6 and Figure 4.7 respectively for wave number $n = 13$ and $n = 14$. It can be seen that the results based on the coarse grid $h/\delta = 0.35$ are almost the same as those obtained by Knio and Ghoniem (Fig. 3 and Fig.

4 in [57]). However, Figure 4.6 and Figure 4.7 also show that when the grid is refined, the numerical solution changes dramatically. The mode of $n = 13$ is in fact rotating and stable, consistent with Widnall's analysis. The mode of $n = 14$ grows and decays periodically in time. It is clear that any conclusions drawn from Figure 4.6(a) and Figure 4.7(a) are artifacts of the numerics since a sufficient refinement of the mesh invalidates them.

To conclude this section, we want to clarify the definitions of "stable" and "unstable" modes mentioned in this section. Note from Figure 4.3, Figure 4.4, and Figure 4.5 that the amplitudes of all modes are bounded. In fact, the absolute boundedness of the amplitude of a mode is not used here as a rule to judge the stability of a mode. Instead, we examine whether or not the amplitude of a mode can be bounded by its initial amplitude multiplied by a constant coefficient. If this is true, we say that the mode is stable; otherwise the mode is unstable. Numerical simulations were carried out for initial perturbation amplitudes $\varepsilon = 0.02R$, $0.01R$, and $0.005R$ with wave numbers $n = 10$, 13, 14, and 15, respectively. The amplitudes vs time for wave numbers $n = 10$ and $n = 13$ are plotted in Figure 4.8 , and those for wave numbers $n = 14$ and $n = 15$ are shown in Figure 4.9. The results indicate that for both $n < 14$ and $n > 14$, the total amplitude of the mode is always bounded by its initial amplitude multiplied by a constant. For $n = 14$, the total amplitude of the mode grows to a maximum of about 0.5δ, regardless of the amplitude of the initial perturbation. Thus, the modes of $n < 14$ or $n > 14$ are classified as stable, whereas the mode of $n = 14$ is classified as unstable.

To fully understand why a mode is stable or unstable, and why the unstable mode ($n = 14$, for $\delta = 0.1R$) has a periodic behavior rather than growing without bound, we continue our discussions in the next section.

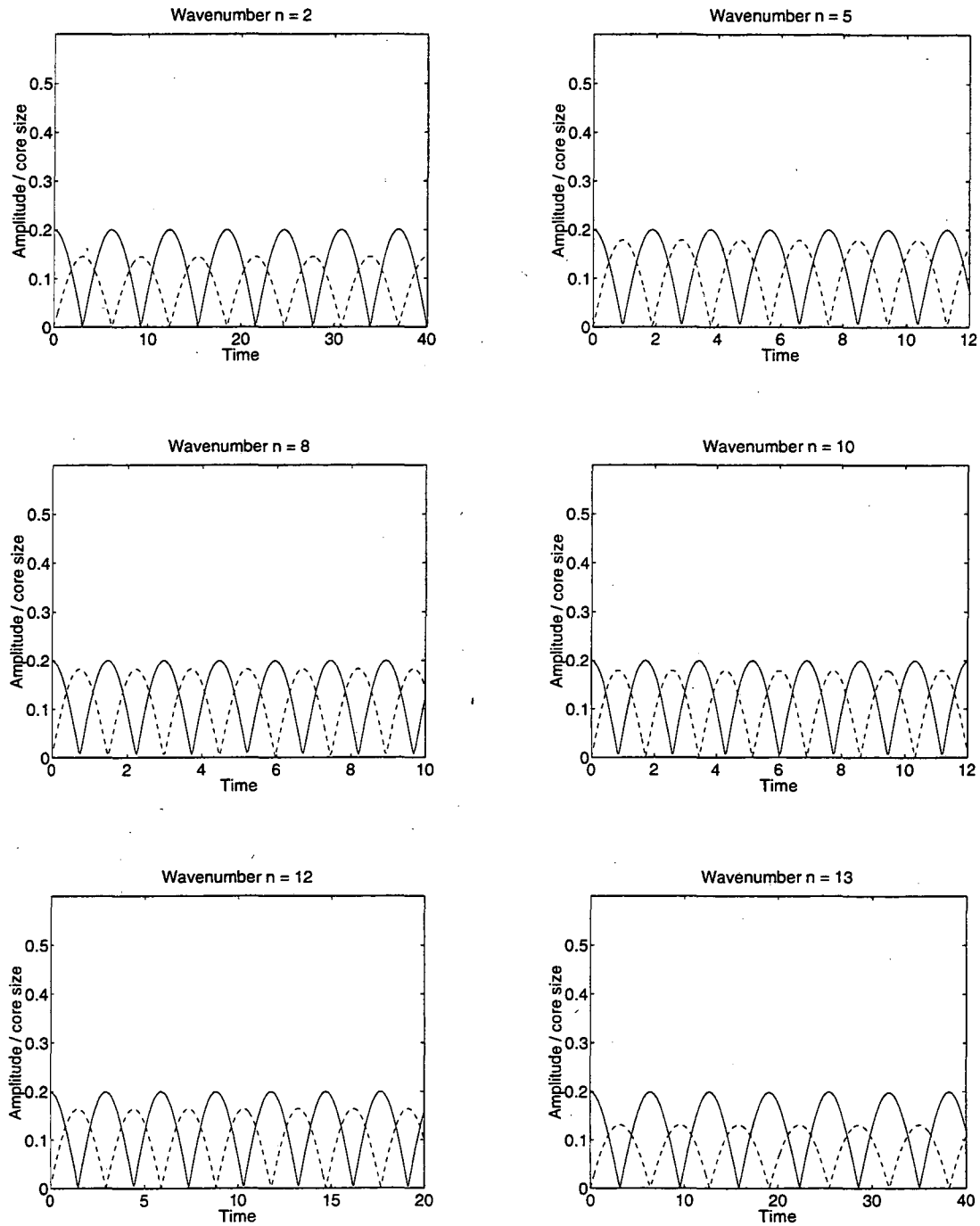

Figure 4.3: Evolution of the amplitude of the perturbation for the ring perturbed at wavenumber $n = 2, 5, 8, 10, 12, 13$, respectively. The solid line denotes the amplitude $\triangle\rho$ in the radial direction and the dashed line denotes the amplitude $\triangle z$ in the streamwise direction.

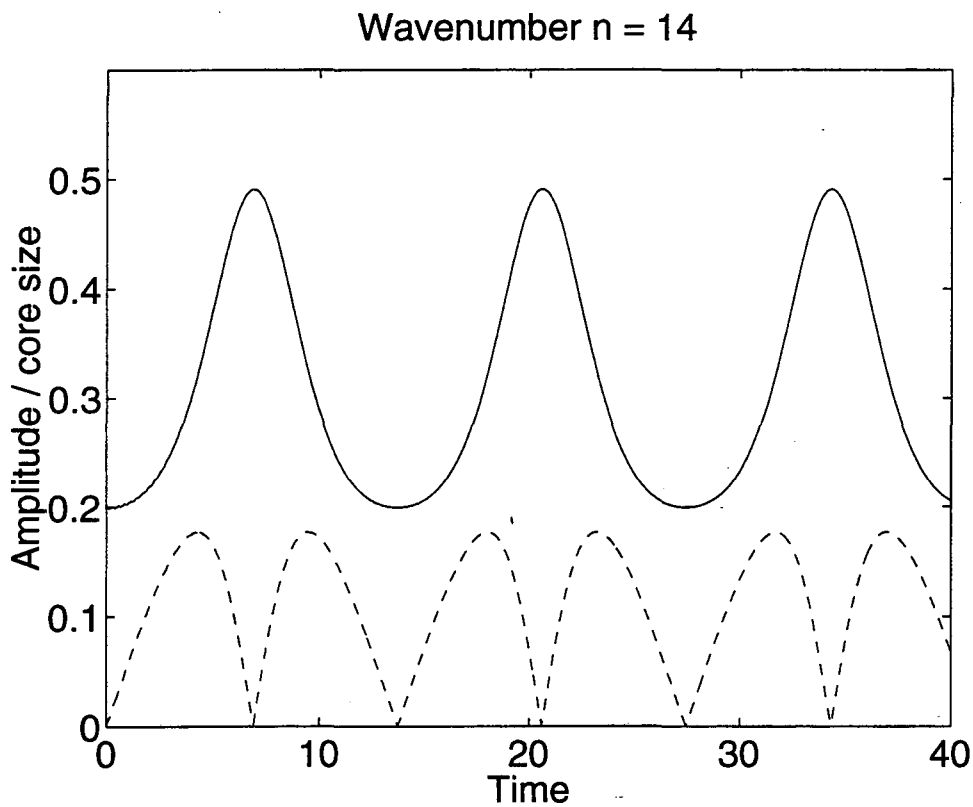

Figure 4.4: Evolution of the amplitude of the perturbation for the ring perturbed at $n = 14$. Notice the periodic behavior of the evolution, which is in contrast with Knio and Ghenoiem's result.

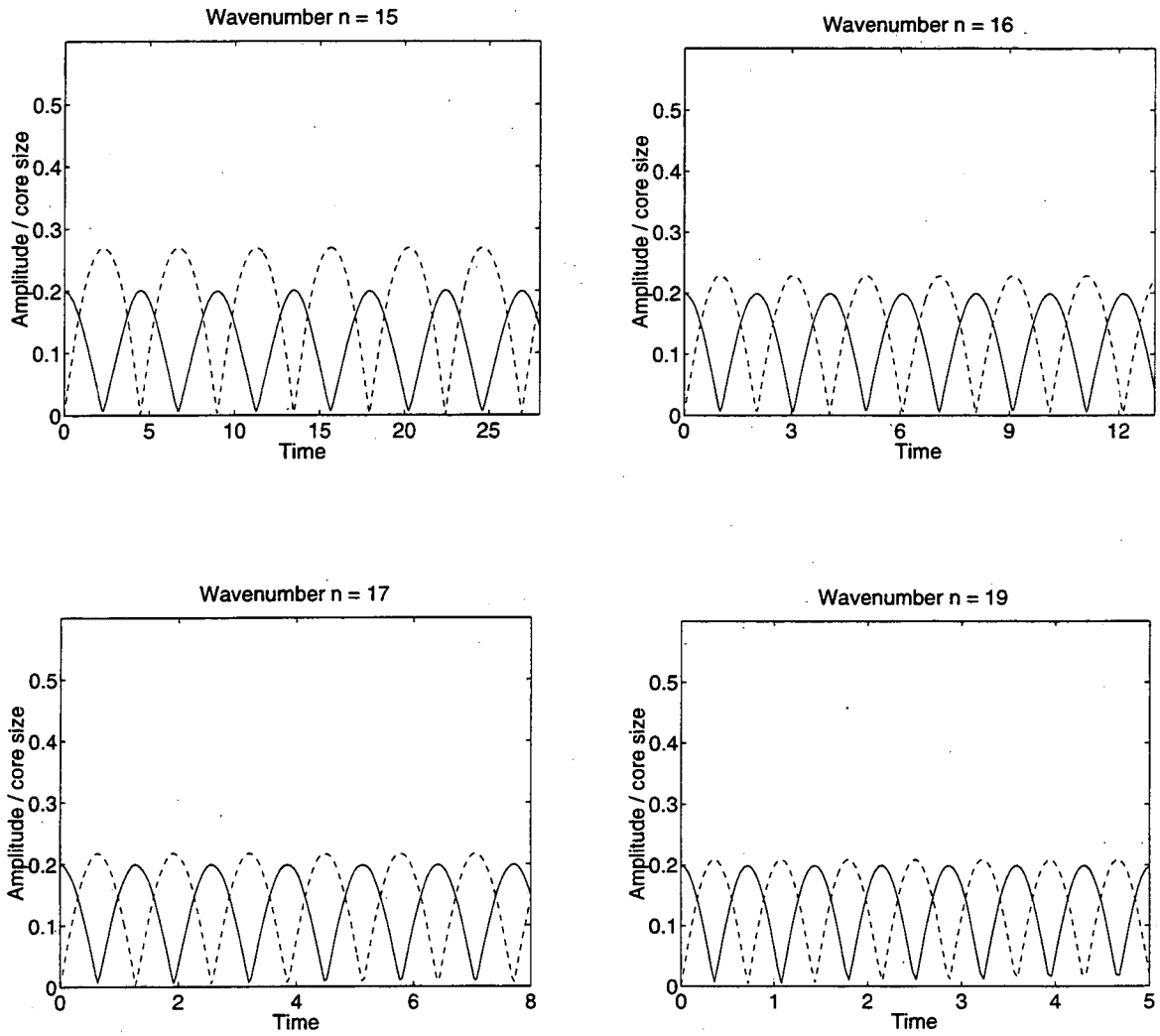

Figure 4.5: Evolution of the amplitude of the perturbation for the ring perturbed at $n = 14$, 15, 17, and 19. The solid line corresponds to the amplitude in the radial direction and the dashed line corresponds to the amplitude in the streamwise direction.

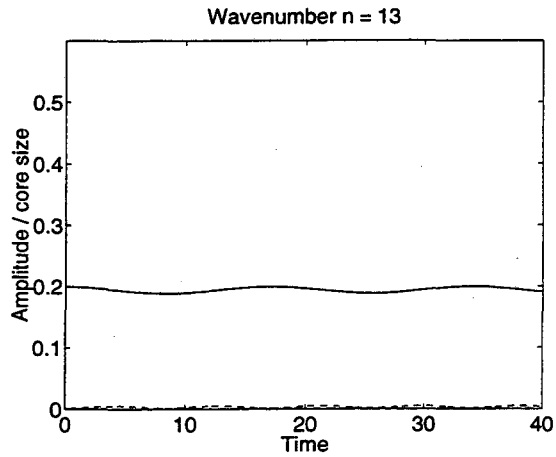

(a). $h/\delta = 0.35$

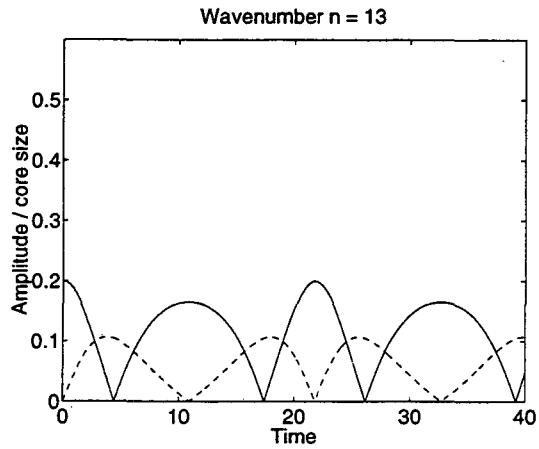

(b). $h/\delta = 0.20$

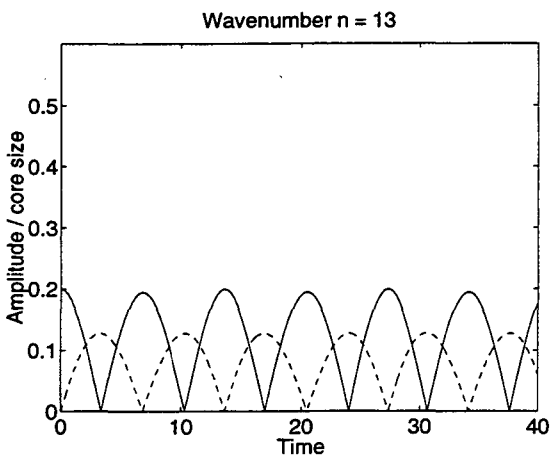

(c). $h/\delta = 0.10$

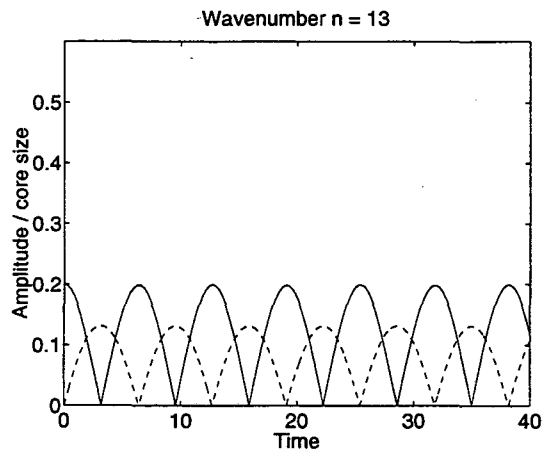

(d). $h/\delta = 0.05$

Figure 4.6: Comparison of the numerical results with different values of h/δ for the evolution of the perturbation wave. The ring is perturbed at wave number $n = 13$. The solid line corresponds to the amplitude in the radial direction and the dashed line corresponds to the amplitude in the streamwise direction.

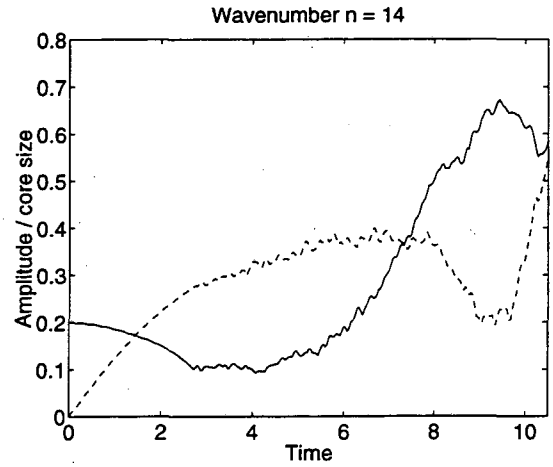

(a). $h/\delta = 0.35$

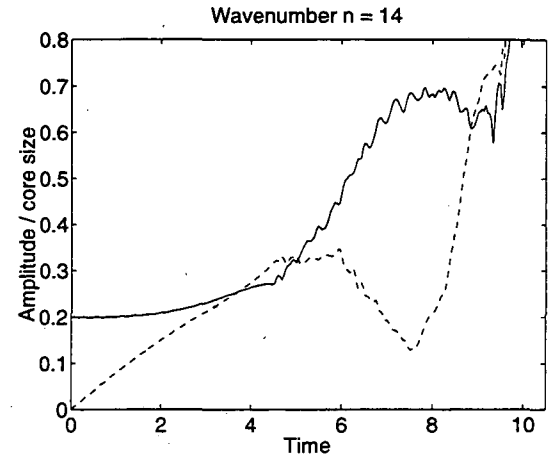

(b). $h/\delta = 0.20$

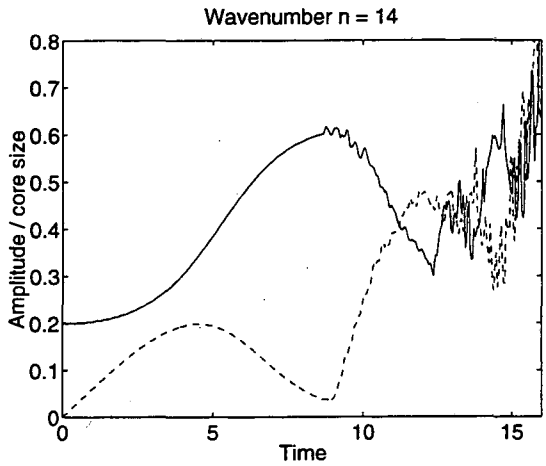

(c). $h/\delta = 0.10$

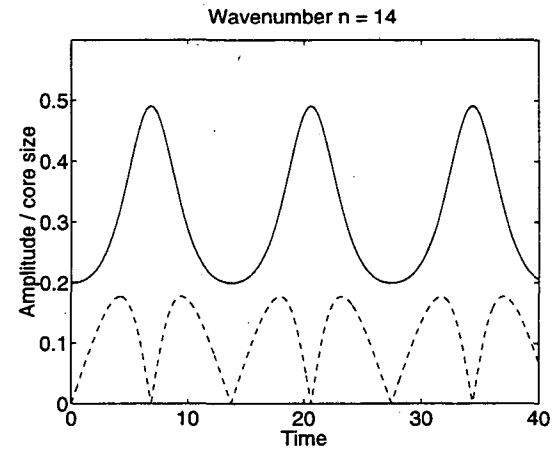

(d). $h/\delta = 0.05$

Figure 4.7: Comparison of the numerical results with different values of h/δ for the evolution of the perturbation. The ring is perturbed at wave number $n = 14$. The solid line corresponds to the amplitude in the radial direction and the dashed line corresponds to the amplitude in the streamwise direction.

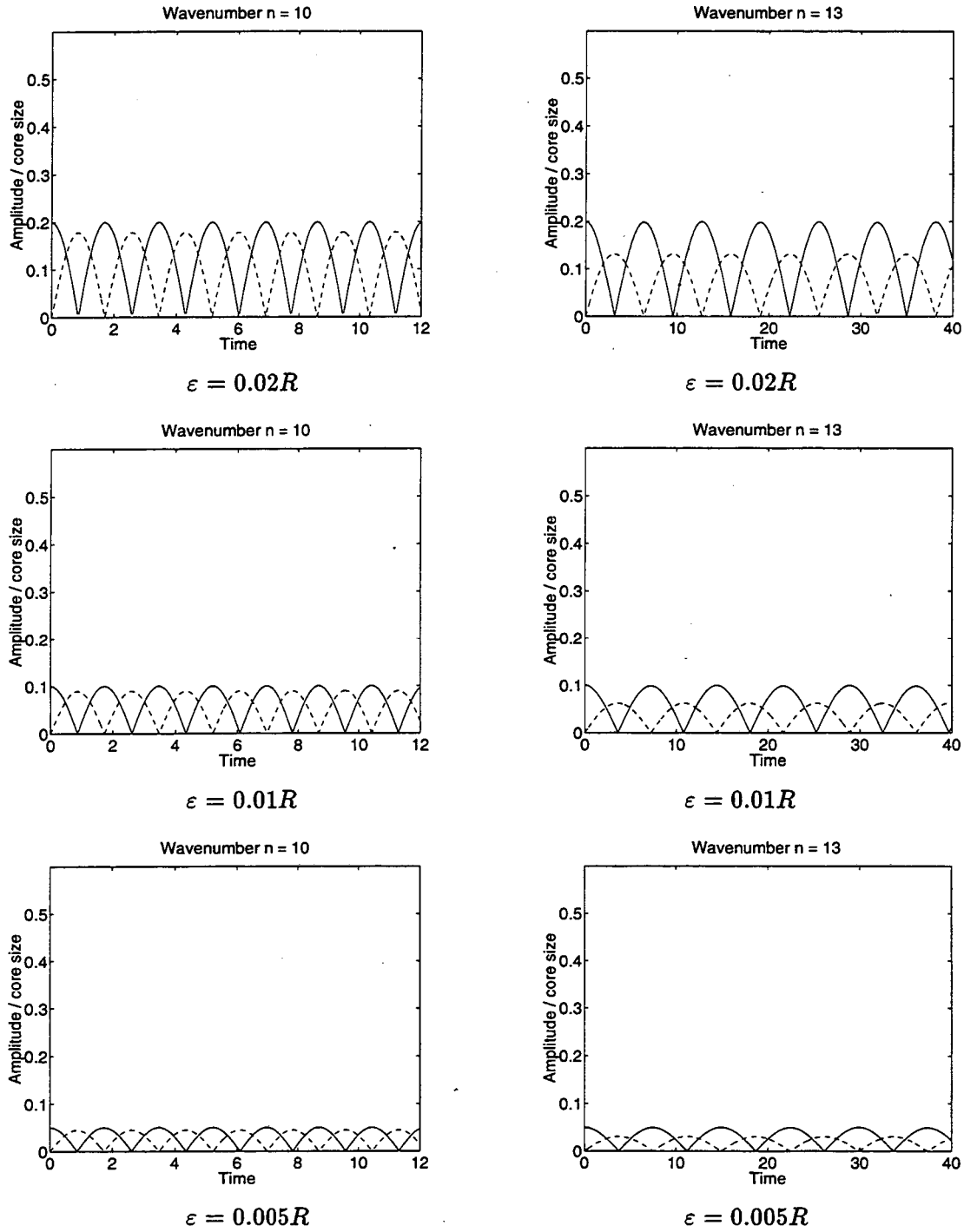

Figure 4.8: Evolution of the perturbation corresponding to different values of the initial amplitude. Notice that the amplitudes for $n = 10$ and $n = 13$ are bounded by their initial values so $n = 10$ and $n = 13$ are both stable modes.

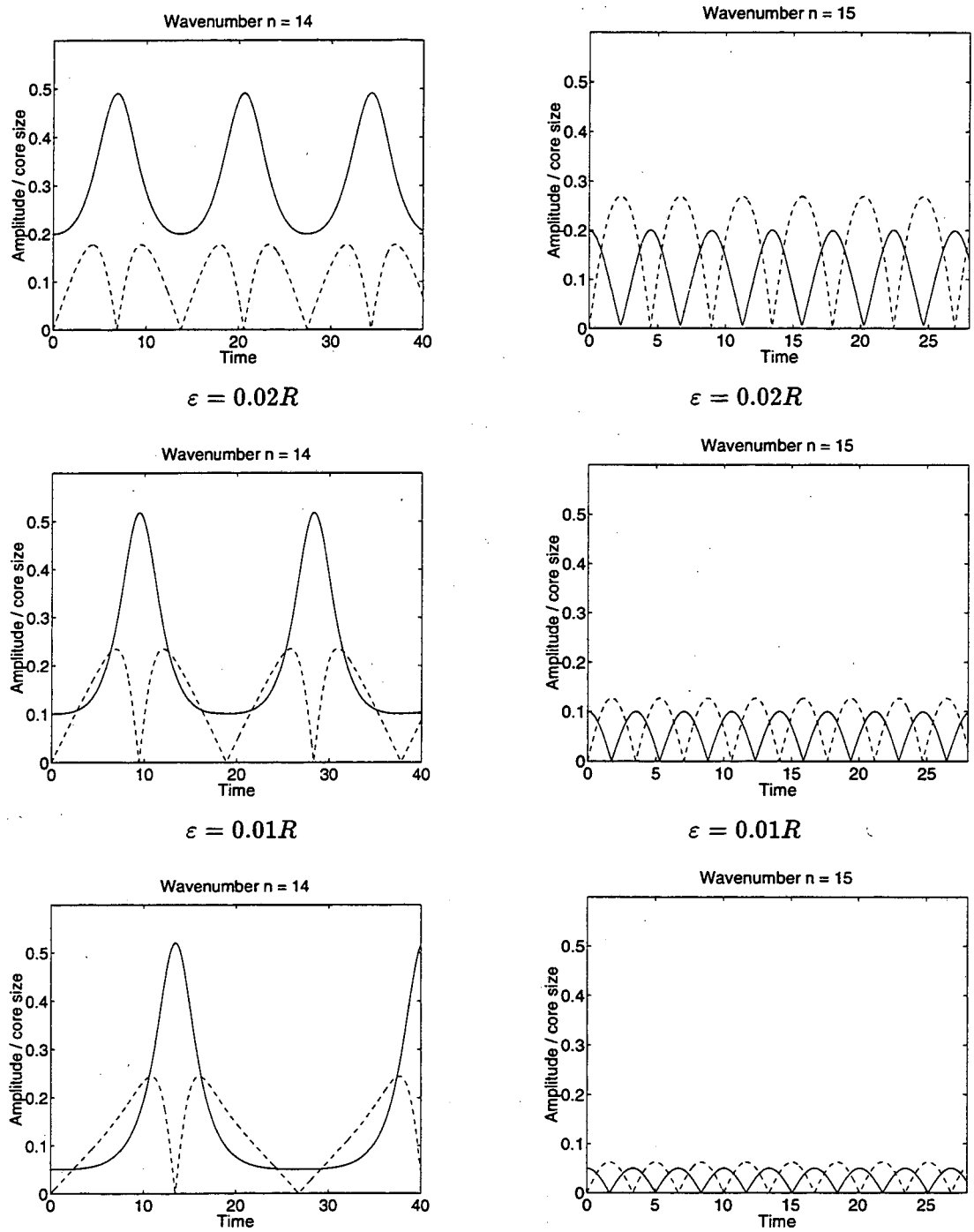

Figure 4.9: Evolution of the perturbation for various initial values. Notice that the amplitudes for $n = 15$ are bounded by their initial values, whereas the amplitudes for $n = 14$ always grow to the same maximum values regardless of the initial values. Hence $n = 14$ is an unstable mode while $n = 15$ is a stable mode.

4.3 Dispersion Relation and Stability Analysis for Thin Tube Vortex Filaments

In this section we try to analyze the evolution of a perturbation wave on a vortex ring. In particular, we will find out which is the unstable mode, what causes it to grow, and why the amplitude of the unstable mode goes up and down in a periodic fashion where the maximum amplitude is bounded by the core size instead of by the initial amplitude.

The analysis is based on the assumptions that (1). the core size δ is small compared with the ring radius; (2). the perturbation wave is a short wave, i.e. $k\delta \sim O(1)$, where k is the wave number; (3). the amplitude of the perturbation wave is small in comparison with the ring radius. The motion of the perturbation wave is the superposition of the self-induced rotation of the wave and the flow caused by the presence of the ring. Under the above assumptions, the self-induced rotation of a sinusoidal wave on a vortex ring is approximately that of a sinusoidal wave on a straight vortex filament, and the flow caused by the presence of the ring is approximately a stagnation point flow.

First, we study numerically the dispersion relation of a sinusoidal wave on a straight thin tube vortex filament, which relates the rotation frequency to the wavenumber and the core radius. A sinusoidal wave of wavenumber k on vortex filaments of core size δ is discretized and the rotation velocity is calculated. The rotation frequency Ω is normalized with respect to $\Gamma/2\pi\delta^2$ which is the solid body rotation frequency of a vortex filament of radius δ and circulation Γ with uniform vorticity distribution. The normalized rotation frequency is plotted as a function of wavenumber times core size ($k\delta$). Figure 4.10 shows the results for sinusoidal waves of small amplitude (i.e. the amplitude is much smaller than the wavelength). The interesting region is $k\delta \sim O(1)$, since for a vortex ring the long waves $k\delta \sim o(1)$ are outside the valid region of the approach of self-induced rotation plus stagnation point flow.

The behavior of the perturbation wave can be understood by investigating the motion of the perturbed filament relative to its unperturbed position. A cross-section of the perturbed vortex ring with a local coordinate system is shown in Figure 4.11. In the new local coordinate system, the origin is the position of the unperturbed filament, the $\tilde{x}$-axis is the radial direction and the $\tilde{y}$-axis is along the axis of symmetry of the ring.

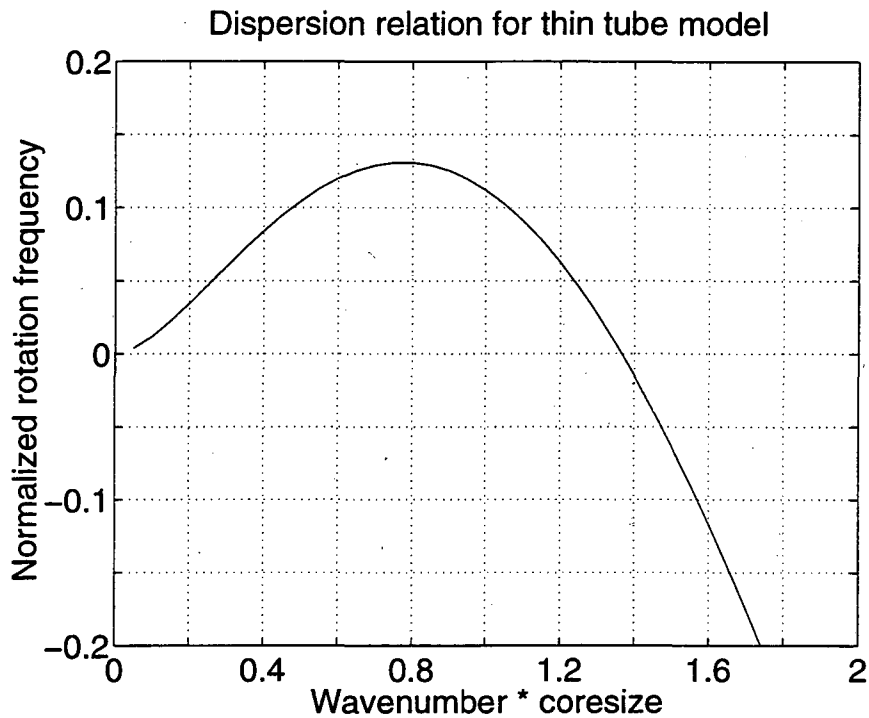

Figure 4.10: Frequency vs wavenumber.

A stagnation point flow of the form

$$u_{\tilde{\theta}}(SP) = -c\tilde{r}\cos(2\tilde{\theta}), \tag{4.6}$$

$$u_{\tilde{r}}(SP) = -c\tilde{r}\sin(2\tilde{\theta}), \tag{4.7}$$

is also sketched in Figure 4.11, where the constant c depends on R, δ, and Γ.

When the self-induced rotation velocity $\Omega\tilde{r}$ of the perturbation wave is small enough such that it can be overcome by the tangential velocity $u_{\tilde{\theta}}(SP)$ of the stagnation point flow, the stagnation point flow will bring the filament to an angle $\tilde{\theta}$ where the total rotation velocity is zero and the perturbation wave grows in the radial direction $\tilde{r}$ with velocity $u_{\tilde{r}}(SP)$. This causes instability. For $\delta = 0.1R$, the wavenumber corresponding to the smallest self-induced rotation frequency is $k = 14/R$, keeping in mind that for a vortex ring, the wave number must satisfy the condition that an integer number of these waves can be fit around the ring, i.e. $k = n/R$. When the self-induced rotation velocity $\Omega\tilde{r}$ of the perturbation wave cannot be balanced by the tangential velocity $u_{\tilde{\theta}}(SP)$ of the stagnation point flow, the filament will rotate around its unperturbed position. In this case, the am-

plitude of the perturbation wave fluctuates and is bounded by a constant multiple of the initial amplitude. Thus the wave is stable.

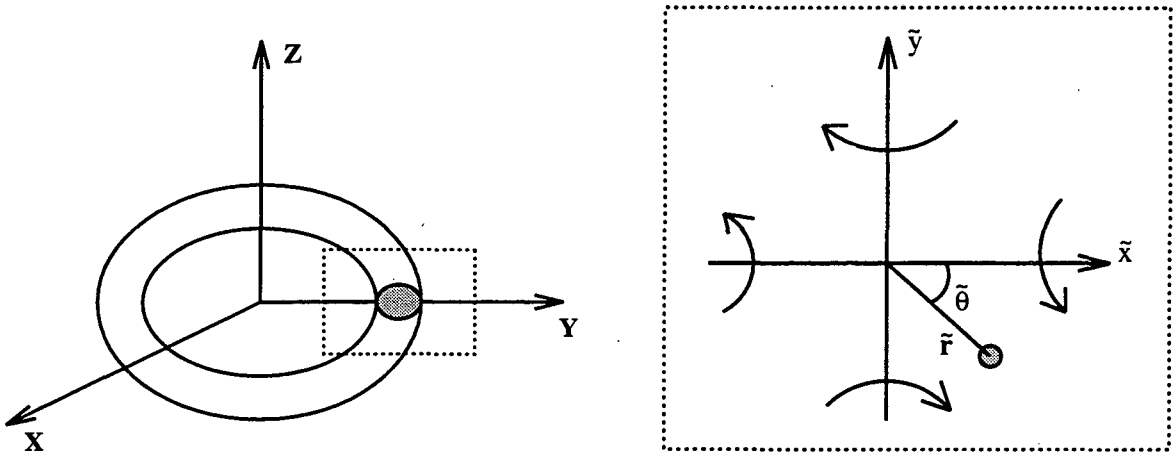

Figure 4.11: A cross-section of the perturbed vortex ring (left) with a local coordinate system (right).

The motion of the filament is the sum of a circular rotation and a stagnation point flow. The total velocity is given by

$$u_{\tilde{\theta}} = -c\tilde{r}\cos(2\tilde{\theta}) + \Omega\tilde{r}, \tag{4.8}$$

$$u_{\tilde{r}} = -c\tilde{r}\sin(2\tilde{\theta}). \tag{4.9}$$

This leads to a system of ODEs for $\tilde{x}$ and $\tilde{y}$:

$$\tilde{x}' = -(\Omega + c)\tilde{y}, \tag{4.10}$$

$$\tilde{y}' = (\Omega - c)\tilde{x}. \tag{4.11}$$

Solving equations (4.10) and (4.11) with the initial conditions

$$\tilde{x}(0) = \varepsilon, \tag{4.12}$$

$$\tilde{y}(0) = 0, \tag{4.13}$$

we find that

$$\frac{\tilde{x}^2}{\varepsilon^2} + \frac{\tilde{y}^2}{\varepsilon^2(\frac{\Omega-c}{\Omega+c})} = 1, \tag{4.14}$$

where ε is the initial amplitude. In the case of $|\Omega| > c$, equation (4.14) represents a family of ellipses corresponding to different initial amplitude ε. For $\Omega > c$, the perturbation wave rotates anti-clockwise (opposite to the vortex core rotation) around the unperturbed filament. Its trajectory is an ellipse whose major axis is the $\tilde{x}$-axis and whose minor axis is the $\tilde{y}$-axis. For $\Omega < -c$, the perturbation wave rotates clockwise (the same as the vortex core rotation) on an ellipse with the $\tilde{y}$-axis as the major axis and the $\tilde{x}$-axis as the minor axis. This result has also been verified by our numerical simulations. The motions of the perturbation waves with respect to the unperturbed axis of the ring, obtained from the numerical solutions, are shown in Figure 4.12 for $n = 13$ and $n = 15$.

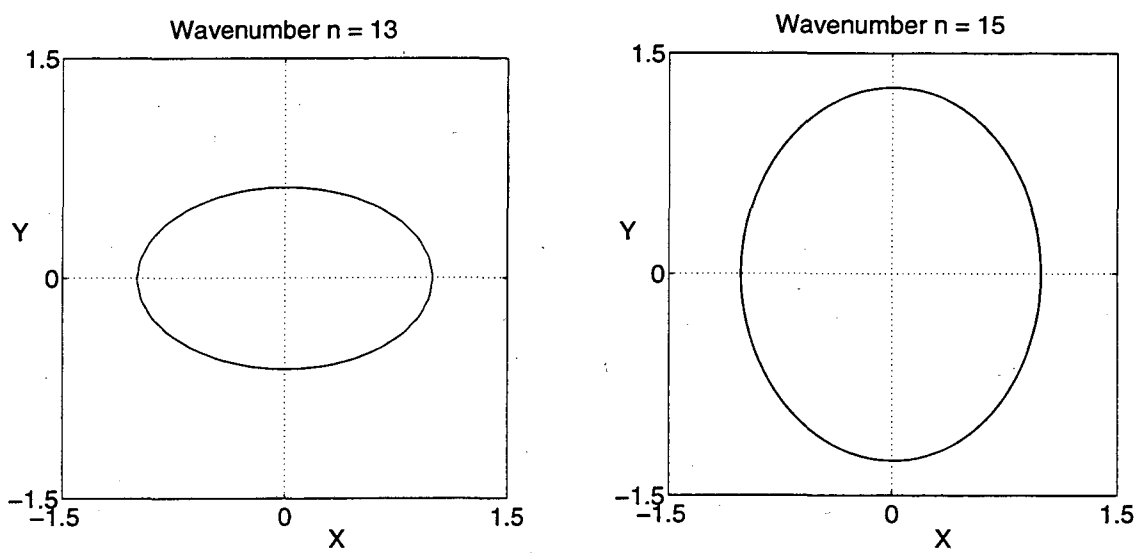

Figure 4.12: Trajectories of the waves ($n = 13$ and $n = 15$) with respect to the unperturbed position. All coordinates have been normalized by the initial amplitude.

In the case of $|\Omega| < c$, equation (4.14) represents a family of hyperbolas with the initial amplitude ε as the independent parameter. The perturbation wave grows on a hyperbola as long as its amplitude is still small in comparison with the vortex core size. It is clear that the amplitude of the wave is not bounded by a constant multiple of the initial amplitude. This can be best seen by considering an initial perturbation of infinitesimal amplitude. It remains to be explained why the amplitude of the unstable mode grows to a maximum and then decreases. In Figure 4.10 we showed the dispersion relation of sinusoidal waves with infinitesimal amplitude. However, the self-induced rotation frequency

may also depend on the amplitude. For $\delta = 0.1R$, the unstable mode has wave number $k = 14/R$. For the combinations of $k\delta = 1.35$, 1.375, and 1.4, we studied numerically the relationship between the self-induced rotation frequency and the amplitude. Figure 4.13 shows the normalized rotation frequencies vs the normalized amplitude, where the normalized amplitude is defined as $amplitude/\delta$. Figure 4.13 indicates that as the amplitude grows, the rotation frequency also increases. This result can be used to explain the periodic behavior of the unstable mode.

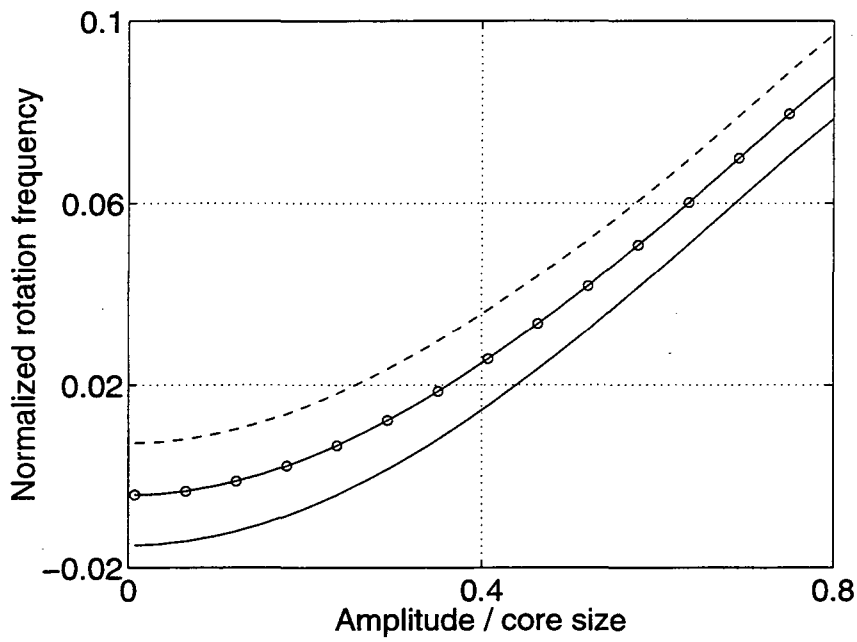

Figure 4.13: Frequency vs perturbation amplitude. $-$: $k\delta = 1.4$, $-o-$: $k\delta = 1.375$, $--$: $k\delta = 1.35$, where k is wave number and δ is the core size

The perturbation wave first follows a hyperbola. As its amplitude grows, its self-induced rotation frequency starts to increase. Hence the total motion of the wave is the motion along a hyperbola plus an anti-clockwise rotation due to the increased rotation frequency. When the amplitude becomes comparable to the core size, the added rotation dominates the motion along hyperbolas. This extra rotation carries the wave above the $\tilde{x}$-axis where the motion along hyperbolas causes a decrease in the amplitude. The family of hyperbolas and the motions on them are sketched in Figure 4.14(a). The decrease in

the amplitudes reduces the self-induced rotation of the wave, which in turn slows down the added rotation. Eventually, the filament goes back to the position where it started with and begins a new cycle.

Now we check this analysis with numerical simulations. Figure 4.14 (b) shows the motion of perturbation waves of various initial amplitudes relative to the unperturbed filament. The trajectories are obtained from the numerical solutions of the unstable mode $n = 14$. We see that the wave first follows a hyperbola, then rotates counter clockwise due to the increase in amplitude and finally follows a hyperbola back to where it started. This is in good agreement with the analysis. In particular, Figure 4.14(b) shows that the amplitude goes up to a maximum, then decreases to its original velue. The maximum amplitude is bounded by a fraction of the core size.

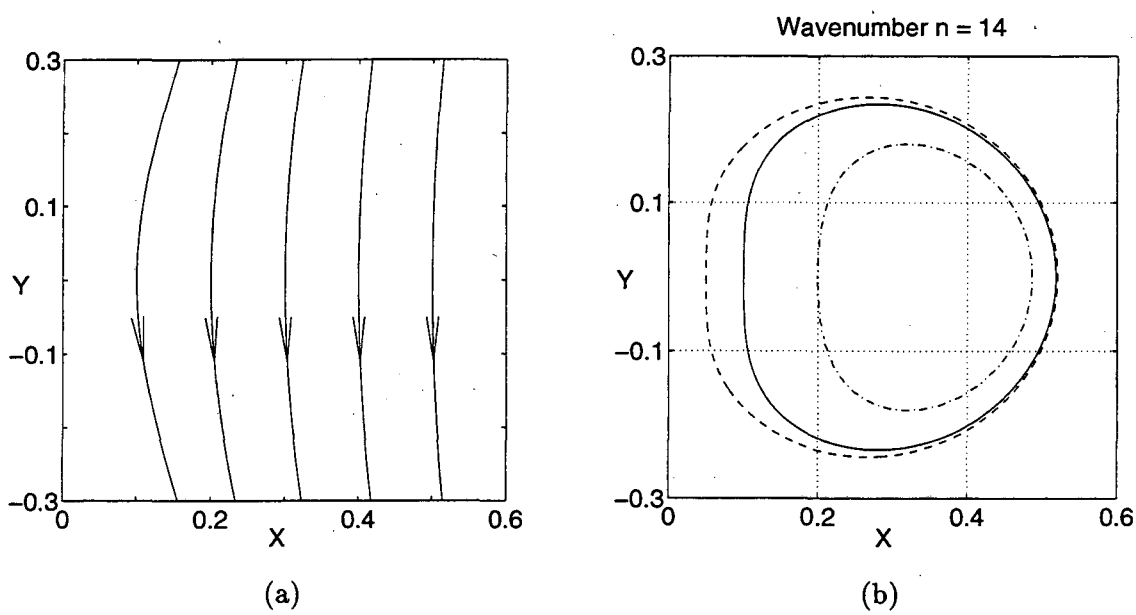

Figure 4.14: (a). A family of hyperbolas and the direction of the motion on them, predicted by the stagnation point flow plus the dispersion relation of sinusoidal waves with small amplitude. (b). The motion of perturbation waves, with respect to the unperturbed filament, obtained in the numerical simulations. $-.-$: initial amplitude $\varepsilon = 0.2\delta$, $-$: $\varepsilon = 0.1\delta$, $--$: $\varepsilon = 0.05\delta$. All coordinates have been normalized by the core size.

More simulations were carried out for various core sizes between $\delta = 0.03R$ and $\delta = 0.20R$. The amplitudes in the ρ-direction and z-direction of the corresponding unstable mode for each core size are shown in Figure 4.15, Figure 4.16, and Figure 4.17. The

results presented in these Figures confirm that the maximum amplitude of the unstable mode is always bounded by a fraction of the core size. Actually the maximum amplitude is bounded by a smaller fraction of the core size as core size gets smaller. This again can be explained by the relation between frequency and amplitude shown in Figure 4.13. The perturbation wave grows initially because the stagnation point flow prevails over the self-induced rotation. The increase of the amplitude causes an increase in the rotation frequency. The wave eventually stops growing when the self-induced rotation is strong enough to counter the stagnation point flow. Recall that the normalized rotation frequency is $2\pi\delta^2/\Gamma$ times the actual rotation frequency. Hence, for smaller core size, the normalized rotation frequency only needs to increase by a smaller amount to stop the growing of the perturbation wave. Translating the increase in the normalized rotation frequency to the increase in the normalized amplitude (see Figure 4.13), we see that for smaller core size, the amplitude can only increase to a smaller fraction of the core size before it stops growing.

We also ran simulations with $\delta = 0.25R$. In this case, the unstable mode $n = 6$ grows without bound and the periodic behavior in time is not observed. This should not be viewed as an evidence against the prediction of the periodic behavior in time of the unstable mode, which is based on the analysis of stagnation point flow plus self-induced rotation and confirmed by numerical simulations for $\delta \leq 0.2R$. The analysis in this chapter and in the previous chapter is for thin vortex rings. They are valid only for small δ/R.

In the numerical simulations up to this point, the initial perturbation wave had a small amplitude, i.e. the amplitude is small in comparison with the core size ($\varepsilon = 0.2\delta$, 0.1δ, or 0.05δ). To find out the behavior of the large initial perturbation, we also carried out simulations with $\delta = 0.1R$, $\varepsilon = \delta$, $n = 14$. Figure 4.18 shows the amplitudes in the ρ-direction and z-direction. The perturbation wave grows without bound. Again we emphasize that this finding does not invalidate the theoretical prediction or the numerical simulations of perturbation waves with small amplitude. The approximation of the flow field around the unperturbed ring filament by a stagnation point flow (an asymptotic expansion) depends on the assumption that the perturbation is small in comparison with the core size. Also for large amplitude perturbations, the rotation frequency of a sinusoidal wave is not well defined because the wave will not keep its shape as it rotates.

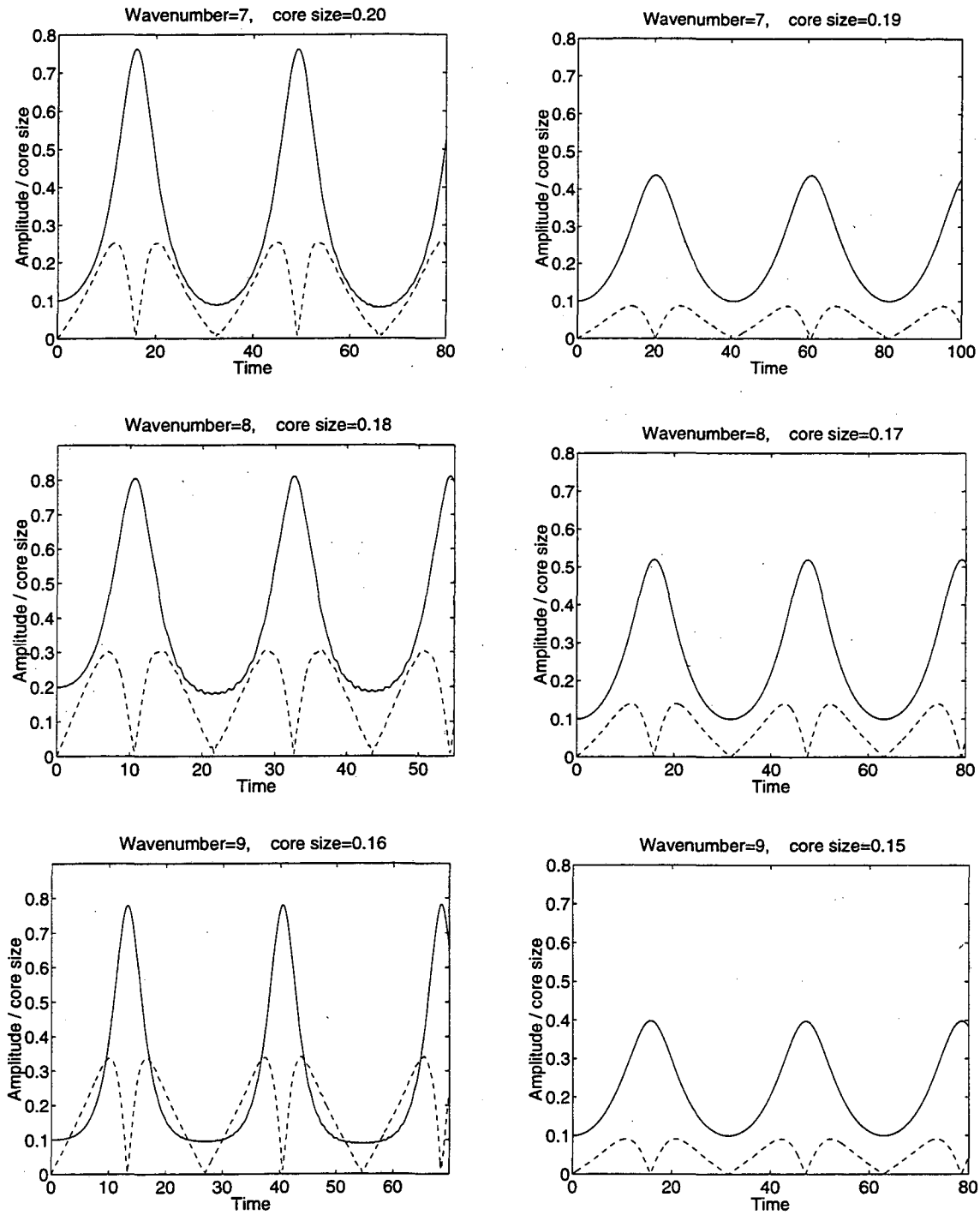

Figure 4.15: Comparison of the evolution of the corresponding unstable mode on a vortex ring for different core sizes. The solid line represents the amplitude in the radial direction and the dashed line represents the amplitude in the streamwise direction.

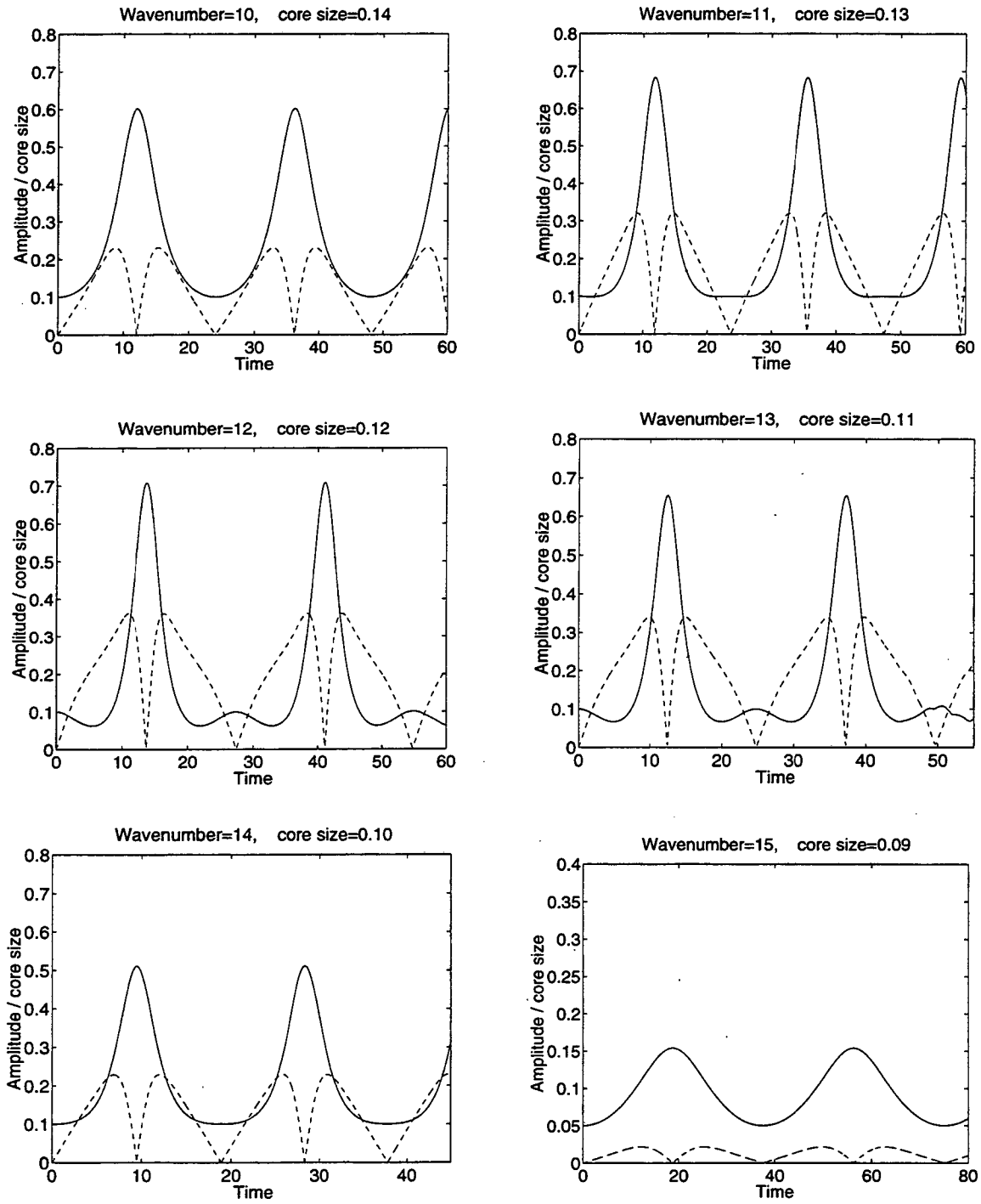

Figure 4.16: Comparison of the evolution of the corresponding unstable mode on a vortex ring for different core sizes. The solid line represents the amplitude in the radial direction and the dashed line represents the amplitude in the streamwise direction.

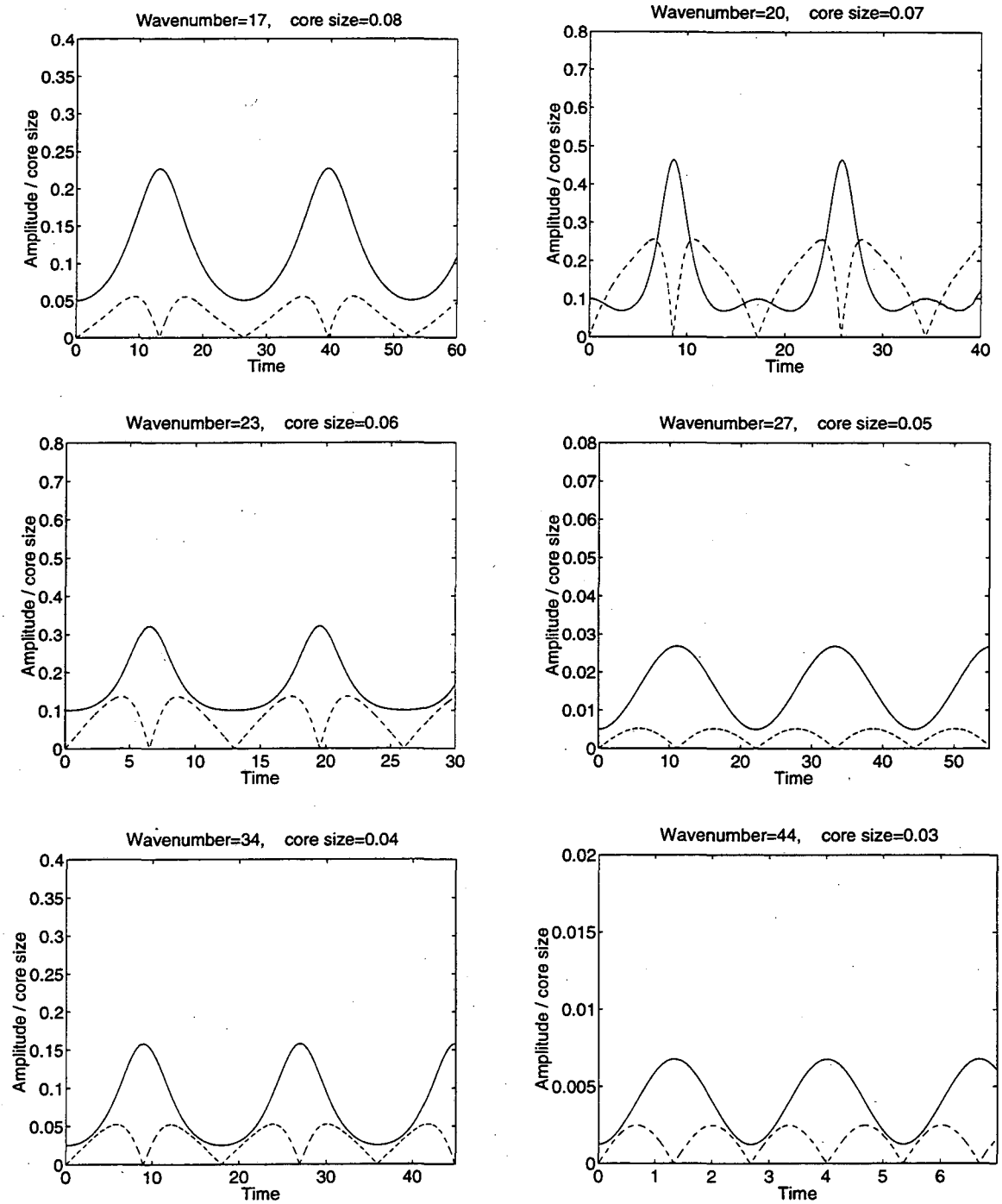

Figure 4.17: Comparison of the evolution of the corresponding unstable mode on a vortex ring for different core sizes. The solid line represents the amplitude in the radial direction and the dashed line represents the amplitude in the streamwise direction.

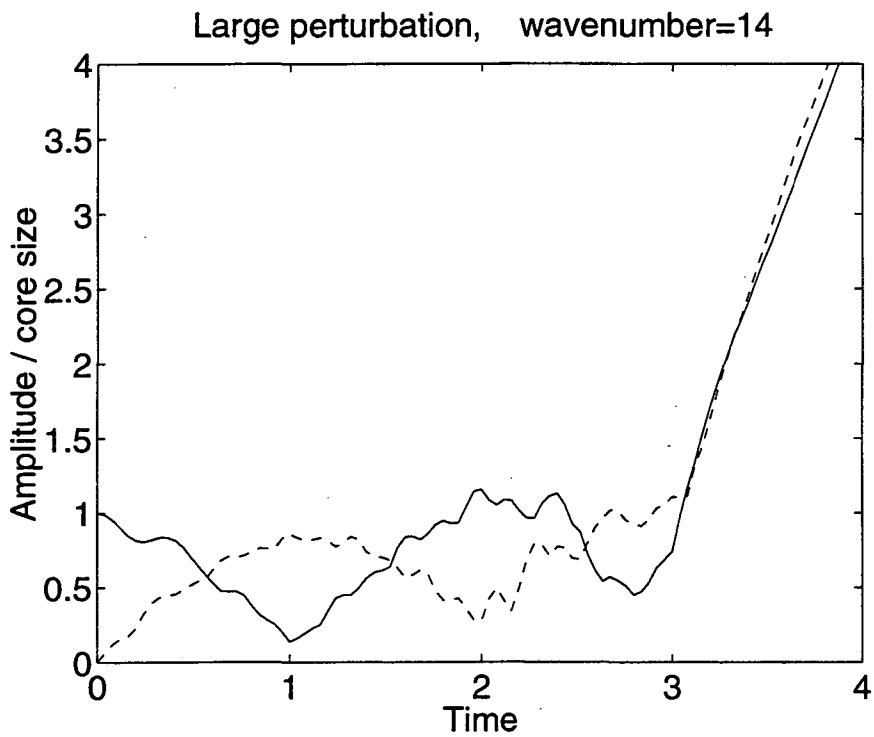

Figure 4.18: Numerical result for the large initial perturbation. The solid line represents the amplitude in the radial direction and the dashed line represents the amplitude in the streamwise direction.

4.4 Concluding Remarks

In this chapter we have performed numerical experiments on vortex rings using the thin tube vortex filament method. Our numerical results were successfully explained by a theoretical stability analysis similar to that given by Widnall et al [95]. We first obtained numerically the dispersion relation for sinusoidal waves on a thin tube filament and then used this in the theoretical analysis to determine the unstable wave number and to explain the behavior of the unstable mode. In contrast to Knio and Ghoniem's results, we found that the amplitude of the unstable mode is bounded by a fraction of the core size and that stable modes always rotates around the unperturbed axis of the vortex ring. The differences between their results and ours are due to their under-resolved spatial mesh.

The main conclusions of this chapter can be summarized as follows:

1. For small perturbation amplitudes and small core sizes ($\delta \leq 0.20R$), the amplitude of the unstable mode grows to a maximum and then decreases, demonstrating a periodic behavior in time. The perturbed vortex ring returns to the shape it started with after a while and then starts a new cycle.

2. For small perturbation amplitudes and small core sizes ($\delta \leq 0.20R$), there exists only one unstable mode corresponding to each core size. The unstable wave number satisfies that an integer number of waves can be fit on the vortex ring and that the mode has the smallest self-induced rotation frequency.

3. For small perturbation amplitudes and a fixed small core size ($\delta \leq 0.20R$), the maximum amplitude of the unstable wave is independent of the initial amplitude. More specifically, no matter how small the initial amplitude is, the perturbation wave eventually reaches the same maximum value and then decreases. That is why we label it "unstable".

4. For small perturbation amplitudes and small core sizes ($\delta \leq 0.20R$), the maximum amplitude of the unstable wave is bounded by a fraction of the filament core size. Furthermore, the ratio of the maximum amplitude to the core size decreases as the normalized core size δ/R decreases.

5. For large core sizes (e.g. $\delta = 0.25R$), the amplitude of the unstable mode grows without bound and the perturbed vortex ring never recovers its initial configuration.

6. For large perturbation amplitudes and small core size, the unstable mode grows without bound and the periodic behavior in time is not observed.

In the next chapter we will discuss the effects of the ODE solver and the time step size on the numerical stability of the vortex method.

Chapter 5

Numerical Stability, ODE Solver, Time Step, Spatial Step and Accuracy

In this chapter we present a careful study of the numerical stability and accuracy of the thin tube vortex filament method. The goal is to analyze the effect of the choice of ODE solver, time step, and spatial step on the computed solution. The criteria for selecting the time integrator and the time step size is obtained. It is based on a theoretical analysis and then verified by numerical simulations.

In the Fourier analysis of stability of linear numerical methods, the maximum amplification rate is usually attained by the discrete mode with the highest wave number on the numerical grid. In most cases, the numerical stability of a method can be predicted by the behavior of the highest numerical mode. Motivated by this observation, we analyze the behavior of the highest discrete mode on a straight vortex filament and arrive at a model equation for this numerical mode. Various Runge-Kutta methods with different time steps are tested on this model equation and the criteria for the selection of ODE solver and time step is established. The goal is to control the growth of the highest numerical mode. From the methods we tested, the classical four stage fourth order Runger-Kutta method turns out to be the best performer. We find that the restriction on the time step is

$$\triangle t \leq C\frac{\delta^2}{\Gamma}, \tag{5.1}$$

where $\triangle t$ is the time step, Γ is the circulation, δ is the core size of the vortex filament and C is

a constant depending on the ODE solver and the cut-off function used in the discretization of the vortex method. This restriction on the time step works well in the numerical simulations we have done. If the time step is above the critical value, the numerical solution blows up very quickly. If the time step is less than the critical value, the numerical solution behaves well. In addition, we find that it is unnecessary to take the time step much smaller than the critical value. This approach of suppressing the growth of the highest numerical mode by selecting a suitable ODE solver and time step size is justified and shown numerically to have no artificial effect on the physical solution we are simulating.

The selection of spatial step size is problem-dependent. In practice, one needs to compare the numerical results of coarse and fine grids to determine whether a step size is small enough. This is the general approach in the numerical simulations of complicated nonlinear problems.

The outline of this chapter is as follows. In the first section, we start by relating the stability of a numerical method to the behavior of the highest discrete mode through examples of Fourier analysis of stability. We then go on to investigate the behavior of the highest discrete mode on a numerical grid on a straight vortex filament. This is followed by the derivation of the evolution equation for this numerical mode. In the second section, various Runge-Kutta type methods are applied to solve this evolution equation and judged in terms of their ability to control the growth of the highest numerical mode. The restriction on the time step is obtained and tested in numerical simulations. In the third section, we consider the effect of spatial step size on numerical solutions.

5.1 Fourier Analysis of Stability and the Highest Discrete Mode on a Numerical Grid

In this section we first review the Fourier series technique for the stability analysis of linear numerical methods and point out the connection between the behavior of the highest numerical mode and the stability of a numerical method. Applying this heuristic principle to the vortex method, we then investigate the evolution of the highest discrete mode on a numerical grid on a straight vortex filament. An approximate equation is obtained for the highest numerical mode.

As a starting point, we consider the heat equation in one space dimension

$$\frac{\partial u}{\partial t} = \frac{\partial^2 u}{\partial x^2}. \tag{5.2}$$

A simple straightforward finite difference scheme for solving equation (5.2) can be constructed as

$$\frac{u_j^{n+1} - u_j^n}{\triangle t} = \frac{u_{j+1}^n - 2u_j^n + u_{j-1}^n}{(\triangle x)^2}. \tag{5.3}$$

Solving for u_j^{n+1} from equation (5.3) gives the equation

$$u_j^{n+1} = u_j^n + \lambda(u_{j+1}^n - 2u_j^n + u_{j-1}^n). \tag{5.4}$$

Here u_j^n is the approximate value for $u(j\triangle x, n\triangle t)$, $\triangle x$ is the spatial step size, $\triangle t$ is the time step size, and $\lambda = \triangle t/(\triangle x)^2$.

The numerical stability of the difference scheme (5.3) can be analyzed by examining a family of particular solutions of the form

$$u_j^n = \rho(\xi, \lambda)^n e^{ij\xi}, \tag{5.5}$$

where $i = \sqrt{-1}$ and the function $\rho(\xi, \lambda)$ is called the amplification factor (for details, see lecture notes by Chorin [16], see also the lecture notes by Sethian [85] and Hald [42]). Equation (5.5) represents a discrete sinusoidal mode on the numerical grid with wave number

$$(\mathrm{mod}(\xi + \pi, 2\pi) - \pi)/(2\pi\triangle x) \tag{5.6}$$

since

$$e^{ij\xi} = e^{i(\frac{\mathrm{mod}\,(\xi+\pi,2\pi)-\pi}{2\pi\triangle x})(j\triangle x)}. \tag{5.7}$$

On a fixed spatial grid, the highest possible wave number of discrete modes is $1/(2\triangle x)$. Substituting (5.5) into (5.4), one obtains immediately

$$\rho(\xi, \lambda) = 1 - 4\lambda \sin^2(\frac{\xi}{2}). \tag{5.8}$$

The requirement for stability is that the amplification factor $\rho(\xi, \lambda)$ be bounded by 1 for any value of ξ (i.e. $|\rho(\xi, \lambda)| < 1$). This requirement results in the stability condition $\lambda \leq \frac{1}{2}$. When this condition is violated, the numerical scheme (5.4) is unstable. In this case, it is interesting to look at the amplification factor $\rho(\xi, \lambda)$ and find out which numerical mode has the maximum amplification rate. In Figure 5.1 (a) we plot the absolute value of the

amplification factor $|\rho(\xi,\lambda)|$ as a function of ξ for $\lambda = 3/4$. Figure 5.1 (a) shows that the maximum amplification rate occurs at $\xi = \xi_0 = \pi$. The corresponding unstable mode is

$$u_j^n = \rho^n(-1)^j. \tag{5.9}$$

Equation (5.9) represents the discrete mode with the highest wave number on the numerical grid, whose value is alternately positive and negative. The amplification factor $|\rho(\xi,\lambda)|$ as a function of λ is shown in Figure 5.1 (b) for the highest numerical mode (5.9). Figure 5.1 (b) illustrates how the stability condition $\lambda \leq 1/2$ can be derived from the amplification rate of the highest discrete mode. This is not surprising. As we will see shortly, this is a common property of many numerical methods.

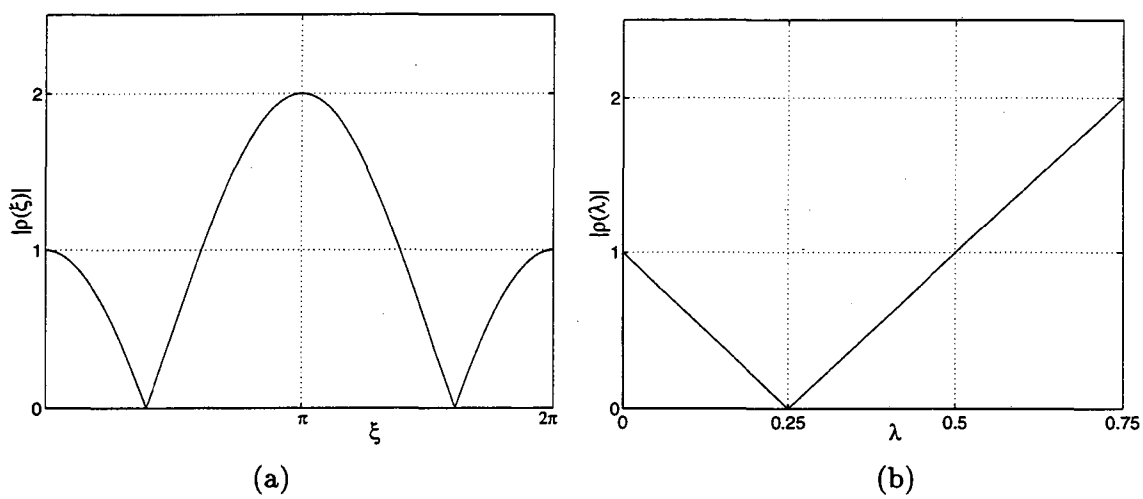

Figure 5.1: (a). The amplification factor $|\rho(\xi,\lambda)|$ vs ξ for $\lambda = 3/4$. (b). The amplification factor $|\rho(\xi,\lambda)|$ vs λ for the most unstable mode $\xi = \pi$.

In a similar way, we can examine the numerical stability of the methods for solving the linear hyperbolic conservation law in one space dimension:

$$\frac{\partial u}{\partial t} + \frac{\partial u}{\partial x} = 0. \tag{5.10}$$

We take two methods as examples, namely, the upwind scheme and the Lax-Wendroff scheme:

$$\text{upwind:} \quad u_j^{n+1} = u_j^n - \lambda(u_j^n - u_{j-1}^n), \tag{5.11}$$

$$\text{Lax-Wendroff:} \quad u_j^{n+1} = u_j^n - \frac{\lambda}{2}(u_{j+1}^n - u_{j-1}^n) + \frac{\lambda^2}{2}(u_{j+1}^n - 2u_j^n + u_{j-1}^n), \tag{5.12}$$

where, for hyperbolic conservation laws, $\lambda = \triangle t/\triangle x$.

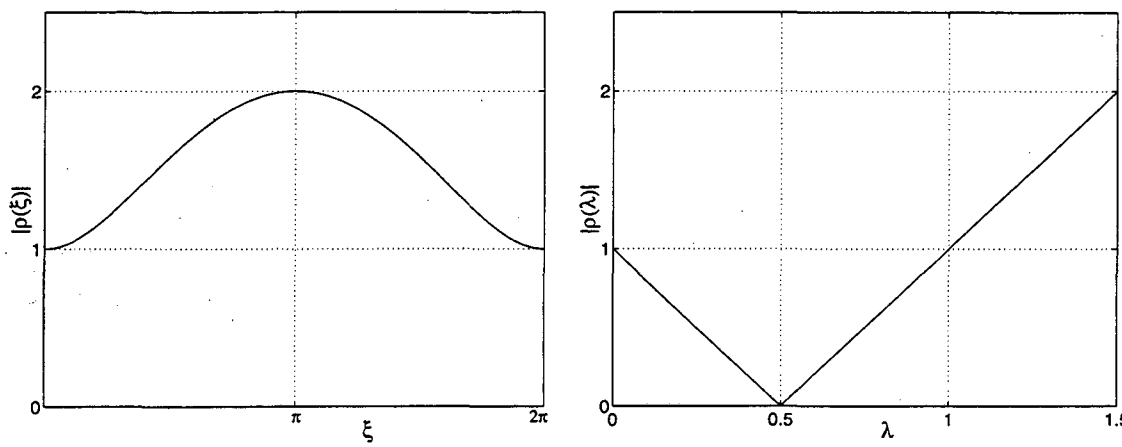

Figure 5.2: Upwind scheme: (a). The amplification factor $|\rho(\xi,\lambda)|$ vs ξ for $\lambda = 3/2$; (b). The amplification factor $|\rho(\xi,\lambda)|$ vs λ for the most unstable mode $\xi = \pi$.

Substituting (5.5) into (5.11) and (5.12) yields their amplification factors respectively:

$$\text{upwind:} \quad \rho(\xi,\lambda) = (1-\lambda) + \lambda e^{-i\xi}. \tag{5.13}$$

$$\text{Lax-Wendroff:} \quad \rho(\xi,\lambda) = 1 - 2\lambda^2 \sin^2(\xi/2) - i\lambda \sin(\xi). \tag{5.14}$$

When $\lambda > 1$, both methods are unstable. For $\lambda = 3/2$, we plot their amplification factors $|\rho(\xi,\lambda)|$ vs ξ in Figure 5.2 (a) and 5.3 (a) respectively.

For both the upwind scheme and the Lax-Wendroff scheme, the maximum amplification rate occurs at $\xi = \xi_0 = \pi$. The amplification factors $|\rho(\xi,\lambda)|$ of the highest discrete mode (5.9) vs λ are shown in Figure 5.2 (b) and Figure 5.3 (b). Again the stability condition $\lambda \leq 1$ is accurately predicted by the amplification rate of the highest discrete mode.

The above examples suggest that the amplification rate of the discrete mode with the highest wave number on the numerical grid can provide useful insights into the numerical stability. For the linear equations and the linear numerical methods we just considered above, the stability condition is actually determined by the behavior of the highest numerical mode. Of course, for these numerical methods, the stability condition can be precisely obtained by rigorous analysis. The important point is that the idea of analyzing the numer-

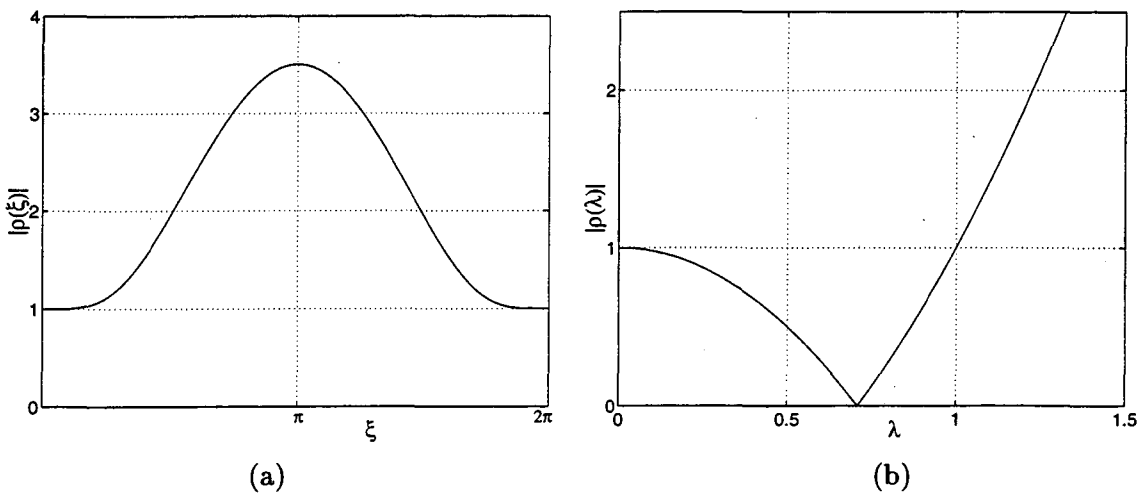

Figure 5.3: Lax-Wendroff scheme: (a). The amplification factor $|\rho(\xi,\lambda)|$ vs ξ for $\lambda = 3/2$; (b). The amplification factor $|\rho(\xi,\lambda)|$ vs λ for the most unstable mode $\xi = \pi$.

ical stability by examining the highest numerical mode goes beyond these linear problems. It can be applied to complicated nonlinear problems. Strictly speaking, it has not been proved that the numerical stability is totally determined by the behavior of the highest numerical mode. Nevertheless, the stability condition of the highest numerical mode can be taken, at least, as a necessary condition for the stability of the numerical method. The situation here is very similar to the approach of judging the numerical stability by the CFL condition, which theoretically is only a necessary condition but often turns out to be the precise condition for the stability of the numerical methods.

We now try to use this approach to analyze the numerical stability of the vortex method. We consider the discrete mode with the highest wave number for the numerical grid on a straight thin tube vortex filament. As sketched in Figure 5.4, a straight vortex filament of core radius δ is divided into elements of length h. To ensure the overlapping of the neighboring elements, we require $h < \delta/2$. At time $t = 0$, the highest discrete mode with small amplitude is imposed on the filament in the x-y plane. More specifically, the initial position of the j-th point is

$$\mathbf{x}_j(0) = (x_j(0), y_j(0), z_j(0)) = (jh, (-1)^j\varepsilon, 0), \tag{5.15}$$

where ε is the amplitude.

By the symmetry of the initial configuration, we know that the perturbation wave

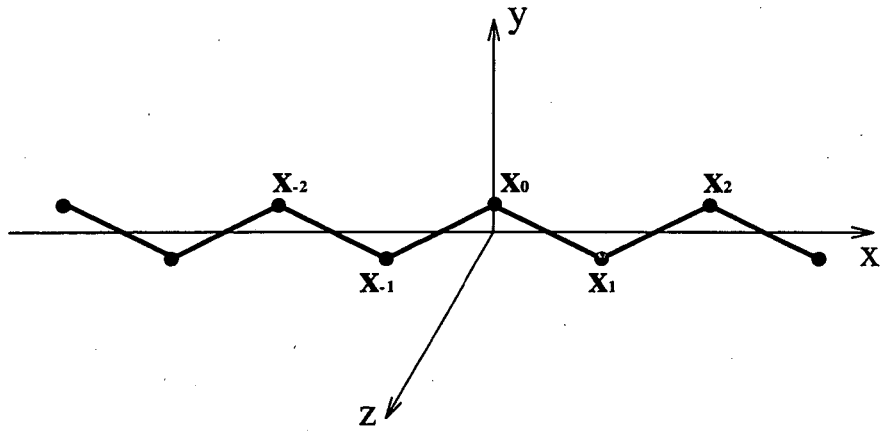

Figure 5.4: A sketch of the highest discrete mode.

will remain on a plane rotating around the x-axis. From the Biot-Savart integral, it can be seen that the velocity induced by the entire filament at $\mathbf{x}_j$ is always perpendicular to the wave plane. Thus if the ODE system is solved exactly in time, the perturbation wave will rotate around the x-axis without any growth in its amplitude. Furthermore, the rotating angular velocity Ω is time independent, since the perturbation wave keeps its original shape. These arguments give rise to the following evolution equation for $\mathbf{x}_j(t) = (x_j(t), y_j(t), z_j(t))$

$$\begin{cases} x_j'(t) &= 0, \\ y_j'(t) &= -\Omega z_j(t), \\ z_j'(t) &= \Omega y_j(t), \end{cases} \tag{5.16}$$

with the initial conditions

$$\begin{cases} x_j(0) &= jh, \\ y_j(0) &= (-1)^j \varepsilon, \\ z_j(0) &= 0. \end{cases} \tag{5.17}$$

The angular velocity Ω is determined by the amplitude ε, the length of vortex element h, the core size δ, the circulation Γ, and the cut-off function f, i.e. $\Omega = \Omega(\varepsilon, h, \delta, \Gamma; f)$. Since the dimension of Ω is 1/time, a rescaling of length will not change Ω. After the rescaling of length $\tilde{L} = L/\delta$, which makes the new core size equal to 1, the new amplitude, the new length of vortex element and the new circulation are

$$\tilde{\varepsilon} = \varepsilon/\delta, \quad \tilde{h} = h/\delta, \quad \tilde{\Gamma} = \Gamma/\delta^2. \tag{5.18}$$

Consequently, the angular velocity Ω can be expressed as

$$\Omega = \Omega(\tilde{\varepsilon}, \tilde{h}, \tilde{\Gamma}; f). \tag{5.19}$$

On the other hand, the angular velocity Ω is proportional to the velocity induced by the vortex filament, which in turn is proportional to the circulation. Hence

$$\Omega = \tilde{\Gamma} \cdot F(\tilde{\varepsilon}, \tilde{h}; f) = \frac{\Gamma}{\delta^2} F(\frac{\varepsilon}{\delta}, \frac{h}{\delta}; f), \tag{5.20}$$

where F is some function which may depend on $\tilde{\varepsilon}$, $\tilde{h}$ and the cut-off function f.

To find out the actual dependence of F on parameters $\tilde{\varepsilon}$, and $\tilde{h}$, we calculate $F(\tilde{\varepsilon}, \tilde{h}; f) = \Omega/\tilde{\Gamma}$ for $0 \leq \tilde{\varepsilon} \leq 0.2$ and $0 < \tilde{h} \leq 0.4$. This region of $(\tilde{\varepsilon}, \tilde{h})$ is a suitable one for the study of numerical stability, since the unstable mode usually starts with a small amplitude and the overlapping condition requires that $h < \delta/2$.

In Table 5.1 we display the values of $F(\tilde{\varepsilon}, \tilde{h})$ for different combinations of $\tilde{\varepsilon}$ and $\tilde{h}$. The cut-off function used in the calculation is $f(r) = 1 - e^{-r^3}$. Table 5.1 demonstrates that $F(\tilde{\varepsilon}, \tilde{h})$ is approximately a constant function of $\tilde{\varepsilon}$ and $\tilde{h}$ in the region of interest.

From the above arguments and numerical calculations, we conclude that, for $\varepsilon/\delta \leq 0.2$ and $h/\delta \leq 0.4$, the angular velocity is given approximately by

$$\Omega = F \cdot \frac{\Gamma}{\delta^2}, \tag{5.21}$$

where F is a constant determined by the cut-off function f. Table 5.2 lists the values of F for several cut-off functions.

Substituting (5.21) into (5.16), we get the governing equation for the crest of the highest discrete mode $(y(t), z(t))$:

$$\begin{cases} y'(t) &= -F \dfrac{\Gamma}{\delta^2} z(t), \quad y(0) = \varepsilon, \\ z'(t) &= F \dfrac{\Gamma}{\delta^2} y(t), \quad z(0) = 0. \end{cases} \tag{5.22}$$

Rescaling the time by $\tilde{t} = t \cdot \dfrac{\delta^2}{F \cdot \Gamma}$ and letting $\zeta(\tilde{t}) = y(\tilde{t}) + iz(\tilde{t})$, we obtain

$$\zeta'(t) = i\zeta(t). \tag{5.23}$$

This is the equation that the highest discrete mode satisfies up to a rescaling of time. In the next section we will compare the performance of various Runge-Kutta type methods on this model equation.

Table 5.1: The values of F as a function of $\tilde{\varepsilon}$ and $\tilde{h}$.

$\tilde{\varepsilon}$	0.200	0.100	0.050	0.020	0.010	0.005	0.002	0.001
$\tilde{h}$	$F(\tilde{\varepsilon}, \tilde{h})$							
0.400	0.2096	0.2122	0.2128	0.2130	0.2130	0.2130	0.2130	0.2130
0.360	0.2098	0.2124	0.2130	0.2132	0.2132	0.2132	0.2132	0.2132
0.320	0.2100	0.2126	0.2132	0.2134	0.2134	0.2134	0.2134	0.2134
0.280	0.2100	0.2125	0.2131	0.2133	0.2133	0.2134	0.2134	0.2134
0.240	0.2099	0.2124	0.2131	0.2132	0.2133	0.2133	0.2133	0.2133
0.200	0.2099	0.2124	0.2130	0.2132	0.2132	0.2132	0.2132	0.2132
0.160	0.2099	0.2124	0.2130	0.2132	0.2132	0.2132	0.2132	0.2132
0.120	0.2099	0.2124	0.2130	0.2132	0.2132	0.2132	0.2132	0.2132
0.080	0.2099	0.2124	0.2130	0.2132	0.2132	0.2132	0.2132	0.2132
0.040	0.2099	0.2124	0.2130	0.2132	0.2132	0.2132	0.2132	0.2132
0.020	0.2099	0.2124	0.2130	0.2132	0.2132	0.2132	0.2132	0.2132
0.010	0.2099	0.2124	0.2130	0.2132	0.2132	0.2132	0.2132	0.2132
0.005	0.2099	0.2124	0.2130	0.2132	0.2132	0.2132	0.2132	0.2132
0.002	0.2099	0.2124	0.2130	0.2132	0.2132	0.2132	0.2132	0.2132
0.001	0.2099	0.2124	0.2130	0.2132	0.2132	0.2132	0.2132	0.2132

Table 5.2: The values of F corresponding to different cut-off functions.

cut-off function $f(r)$	value of constant F
$f(r) = 1 - e^{-r^3}$	$F = 0.213$
$f(r) = 1 + (\frac{3}{2}r^3 - 1)e^{-r^3}$	$F = 0.426$
$f(r) = \tanh(r^3)$	$F = 0.228$
$f(r) = \tanh(r^3) + \frac{3}{2}\frac{r^3}{\cosh^2(r^3)}$	$F = 0.456$

5.2 Comparison of Various Runge-Kutta Methods on the Model Equation $\zeta'(t) = i\zeta(t)$

We have just established that the highest discrete mode satisfies $\zeta'(t) = i\zeta(t)$. Caused primarily by numerical noises, the highest discrete mode starts with very small amplitude. It contributes little to the accuracy of the numerical method as long as its amplitude remains small. As shown in the previous section, if the time integration is carried out exactly, the highest discrete mode will rotate around the vortex filament without growing. The accurate resolution of the highest discrete mode, which usually requires a very small time step size, is irrelevant to the improvement of the overall accuracy. Thus it is not worth the computational effort. However, the highest discrete mode plays a vital role in the numerical stability. If it grows catastrophically under an ODE solver, it will totally ruin the numerical accuracy. Therefore, when selecting a numerical ODE solver and a time step size, our first concern is to control the growth of the highest discrete mode.

We are now ready to test several Runge-Kutta type methods on the model equation (5.23), whose exact solution describes a point rotating around the origin on the complex plane. These methods will be judged not only by their ability to resolve the solution accurately with a small time step, but also by their ability to yield a bounded numerical solution when the time step is fairly large. We consider the following Runge-Kutta methods.

- Forward Euler method (one stage, first order):

$$K_0 = i\zeta^n \Delta t, \tag{5.24}$$
$$\zeta^{n+1} = \zeta^n + K_0. \tag{5.25}$$

- Prediction-correction method (two stages, second order):

$$K_0 = i\zeta^n \Delta t, \tag{5.26}$$
$$K_1 = i(\zeta^n + K_0)\Delta t, \tag{5.27}$$
$$\zeta^{n+1} = \zeta^n + \frac{1}{2}(K_0 + K_1). \tag{5.28}$$

- Heun method (three stages, third order)

$$K_0 = i\zeta^n \Delta t, \tag{5.29}$$
$$K_1 = i(\zeta^n + \frac{1}{3}K_0)\Delta t, \tag{5.30}$$
$$K_2 = i(\zeta^n + \frac{2}{3}K_0)\Delta t, \tag{5.31}$$
$$\zeta^{n+1} = \zeta^n + \frac{1}{4}(K_0 + 3K_2). \tag{5.32}$$

- Classical Runge-Kutta method (four stages, fourth order)

$$K_0 = i\zeta^n \Delta t, \tag{5.33}$$
$$K_1 = i(\zeta^n + \frac{1}{2}K_0)\Delta t, \tag{5.34}$$
$$K_2 = i(\zeta^n + \frac{1}{2}K_1)\Delta t, \tag{5.35}$$
$$K_3 = i(\zeta^n + K_2)\Delta t, \tag{5.36}$$
$$\zeta^{n+1} = \zeta^n + \frac{1}{6}(K_0 + 2K_1 + 2K_2 + K_3). \tag{5.37}$$

- Prince-Dormand fifth order method used in Dopri 5(4) (six stages):

$$K_0 = i\zeta^n \Delta t, \tag{5.38}$$
$$K_1 = i(\zeta^n + \frac{1}{5}K_0)\Delta t, \tag{5.39}$$
$$K_2 = i(\zeta^n + \frac{3}{40}K_0 + \frac{9}{40}K_1)\Delta t, \tag{5.40}$$
$$K_3 = i(\zeta^n + \frac{44}{45}K_0 - \frac{56}{15}K_1 + \frac{32}{9}K_2)\Delta t, \tag{5.41}$$

$$K_4 = i(\zeta^n + \frac{19372}{6561}K_0 - \frac{25360}{2187}K_1 + \frac{64448}{6561}K_2 - \frac{212}{729}K_3)\Delta t, \tag{5.42}$$

$$K_5 = i(\zeta^n + \frac{9017}{3168}K_0 - \frac{355}{33}K_1 + \frac{46732}{5247}K_2 + \frac{49}{176}K_3 - \frac{5103}{18656}K_4)\Delta t, \tag{5.43}$$

$$\zeta^{n+1} = \zeta^n + \frac{35}{384}K_0 + \frac{500}{1113}K_2 + \frac{125}{192}K_3 - \frac{2187}{6784}K_4 + \frac{11}{84}K_5 \tag{5.44}$$

Note that the fourth order method used in Dopri 5(4) has seven stages. Thus the full Dopri 5(4) is a seven-stage method. It has been argued that, for Dopri 5(4), the last stage (i.e. the seventh stage) of the current time step coincides with the first stage of the next time step and consequently the Dopri 5(4) is essentially a six-stage method. This is true if the input of the next time step is exactly the output of the current time step. However, for the vortex method, a lot of things may happen between the end of the current time step and the beginning of the next time step. For example, new numerical points are added where the vortex line has been stretched, in order to maintain a reasonable resolution in spatial dimensions. Also if the hairpin removal technique is combined with the vortex method, numerical points are deleted where hairpins have formed. So in practice, Dopri 5(4) is a seven-stage method.

Now define $\rho(\Delta t) = \zeta^{n+1}/\zeta^n$ as the amplification factor. For the above Runge-Kutta methods, the amplification factors against time step Δt are plotted in Figures 5.5, 5.6, 5.7, 5.8, and 5.9 respectively.

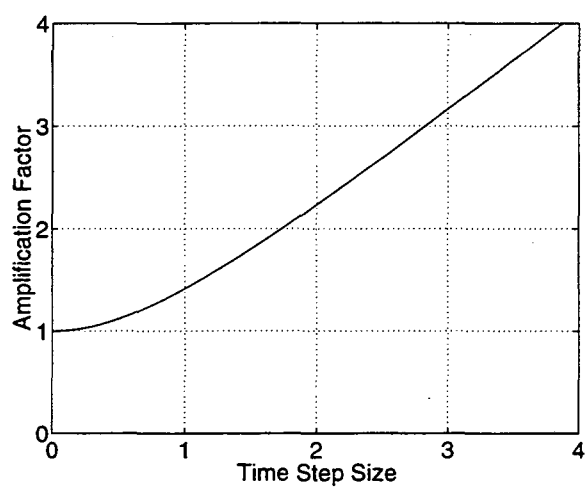

Figure 5.5: Amplification factor of the forward Euler method.

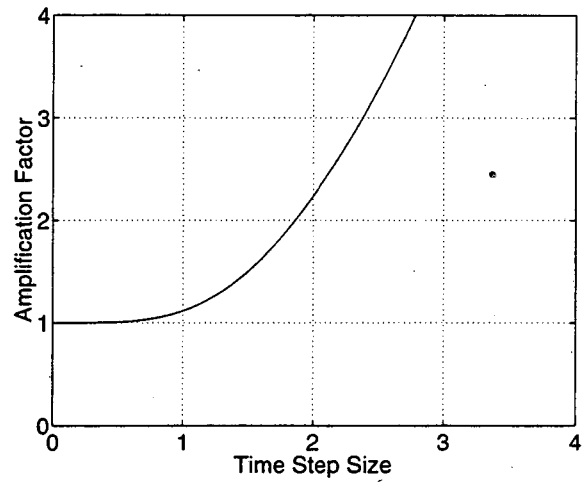

Figure 5.6: Amplification factor of the prediction-correction method.

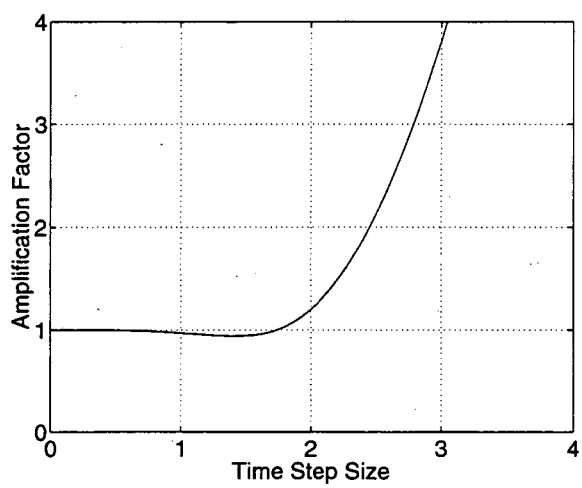

Figure 5.7: Amplification factor of the Heun third order method.

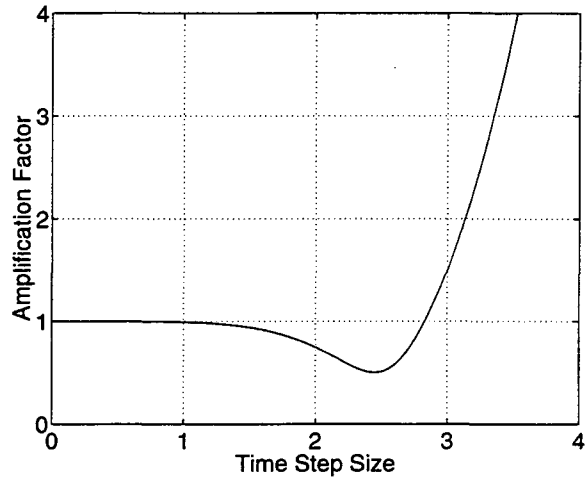

Figure 5.8: Amplification factor of the classical Runge-Kutta method.

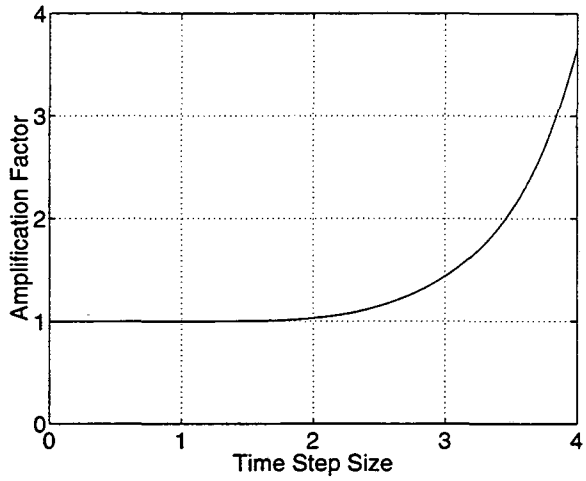

Figure 5.9: Amplification factor of the Prince-Dormand 5(4) method.

The amplification factor $\rho(\triangle t)$ is the multiplier by which the numerical solution is amplified at each time step. For $|\rho(\triangle t)| < 1$, the numerical solution is actually diminished. If $|\rho(\triangle t)|$ is well above 1, the numerical solution blows up in a few time steps. This is clearly unacceptable in numerical simulations and should be avoided by any means necessary. When $|\rho(\triangle t)|$ is above but very close to 1, the numerical solution will grow exponentially but at a slow pace. In this case, the numerical solution is theoretically without bound and will eventually become very large. However, whether this kind of amplification factor (i.e. $|\rho(\triangle t)|$ is slightly above 1) is acceptable in applications depends on the scale of the interesting time period of the underlying physical problem. For the simulations of long time behaviors, it is best to have an amplification factor not larger than 1. In this way, we can be sure that at least a particular form of numerical noise — the highest discrete mode — will not grow exponentially.

Let I be the interval of time step $\triangle t$, where the amplification factor $\rho(\triangle t)$ is bounded by 1. Mathematically the interval I can be expressed as

$$I \equiv \left\{ \triangle t \;\middle|\; |\rho(\triangle t)| \leq 1 \right\} . \tag{5.45}$$

The size of the interval I gives roughly the largest time step size which could be used if we do not want the numerical solution to increase. Keep in mind that the numerical solution here corresponds to the amplitude of the highest discrete mode. We have argued that it is unnecessary to resolve the highest discrete mode accurately but it is crucial to keep the amplitude of this mode small. Table 5.3 shows the interval I for various Runge-Kutta methods. Note that the classical Runge-Kutta method has the largest interval I.

In order to speed up numerical methods, it is desirable to have a time step as large as the accuracy allows. The time step is generally restricted by

(a) the local truncation error in the time direction, which is the new error associated with the time discretization in one time step ;

(b) the amplification factor of the previous error, which determines how the error propagates in time.

Often **(b)** is more restrictive on the time step size than **(a)**. This can be explained by the following argument. If the local truncation error is large, the total error will grow linearly at a large rate. When the amplification factor is well above 1, the total error grows

exponentially and very soon gets out of control. We have already shown that it is the highest numerical mode that most likely has the maximum amplification factor. So the interval I plays a central role in determining the time step size. To be able to use a large time step, we first need to make the interval I as large as possible. Hence we choose the classical four stage fourth order Runge-Kutta method as our ODE solver.

Table 5.3: The interval I for different ODE solvers.

Numerical ODE solver	The interval I
Euler method	$I = \{0\}$
Prediction-correction method	$I = \{0\}$
Heun third order method	$I = [0, 1.73]$
Classical Runge-Kutta method	$I = [0, 2.83]$
Prince-Dormand 5(4) method	$I = [0, 0.997]$

When an ODE solver is applied to solve the equation $\zeta'(t) = i\zeta(t)$, in order to have a non-increasing numerical solution, the time step $\triangle t$ has to fall in the interval I, that is,

$$\triangle t \leq |I|. \tag{5.46}$$

Taking the rescaling of the time $\tilde{t} = t \cdot \dfrac{\delta^2}{F \cdot \Gamma}$ into consideration, we obtain that the time step $\triangle t$ for solving the governing equation of the highest numerical mode (5.22) should satisfy

$$\triangle t \leq \frac{|I|}{F} \frac{\delta^2}{\Gamma}, \tag{5.47}$$

where F is the constant determined by the cut-off function (see Table 5.2), I is the interval related to the ODE solver (see Table 5.3), Γ is the circulation, and δ is the core size of the vortex filament. Expression (5.47) is the constraint on the time step $\triangle t$ of the vortex method, if we want to keep the highest discrete mode under control. It has to be emphasized

that this approach of suppressing the highest discrete mode by a careful selection of ODE solver and time step will not affect the real growth of the physical modes. In a valid numerical simulation, the wavelength of the physical mode should be large in comparison with the spatial step size, which is comparable to the wavelength of the highest discrete mode. In other words, to achieve a reasonable accuracy in spatial dimension, we need to distribute many numerical points in regions of the characteristic length scale of the problem. As a result, the physical mode is far away from the highest numerical mode.

5.3 Numerical Verifications

In this section we carry out numerical simulations to verify the restriction on the time step $\triangle t$ obtained in last section

$$\triangle t \leq \frac{|I|}{F}\frac{\delta^2}{\Gamma} \equiv \triangle t_c, \tag{5.48}$$

where F is a constant determined by the cut-off function (Table 5.2), I is the A-stable interval of the ODE solver for the model equation $\zeta'(t) = i\zeta(t)$, Γ is the circulation and δ is the core size of the vortex filament. We find that the constraint (5.48) agrees very well with the numerical results. For time step $\triangle t$ larger than the critical value $\triangle t_c$, the numerical solution blows up very quickly. For time step $\triangle t$ smaller than the critical value $\triangle t_c$, the numerical solution behaves well. A comparison of the result obtained using a time step slight below the critical value $\triangle t_c$ with the result obtained using a very small time step suggests that it is unnecessary to take the time step much smaller than the critical value $\triangle t_c$. At the end of this section, we discuss the issue of the spatial step size.

We use the Widnall's vortex ring instability as a test problem. As in Chapter 4, we take the initial condition as

$$\begin{cases} x_j = (R + \varepsilon\cos(nj\triangle\theta))\cos(j\triangle\theta), \\ y_j = (R + \varepsilon\cos(nj\triangle\theta))\sin(j\triangle\theta), \\ z_j = 0, \end{cases}$$

for $j = 1, 2, ..., N$, where $\triangle\theta = 2\pi/N$. The circulation is chosen to be $\Gamma = 1$, the core size $\delta = 0.1$, the perturbation wave number $n = 14$ and the initial amplitude $\varepsilon = 0.1\delta$. Initially, the ratio of the distance between two adjacent numerical nodes to the core size is $h/\delta = 0.05$. As we will see later in this section, this seemingly very small h is needed

to achieve the numerical convergence in spatial dimensions for this problem. The cut-off function is the second order one: $f(r) = 1.0 - e^{-r^3}$. The constant F associated with this cut-off function is 0.213, as seen from Table 5.2.

We test two numerical ODE solvers, namely Heun third order method and the classical fourth order Runge-Kutta method. For Heun method, the interval $I = [0, 1.73]$ (see Table 5.3). The critical time step $\triangle t_c$ is given by equation (5.48) as

$$\triangle t_c = \frac{|I|}{F}\frac{\delta^2}{\Gamma} = 0.081. \tag{5.49}$$

We run the simulations with four different time steps. The first choice of time step $\triangle t = 0.09$ is above the critical time step $\triangle t_c$, the second choice of time step $\triangle t = 0.08$ is very close to $\triangle t_c$, the third choice of time step $\triangle t = 0.07$ is below $\triangle t_c$, and the fourth choice of time step $\triangle t = 0.01$ is much smaller than $\triangle t_c$. The numerical results obtained by Heun method using these four time steps are shown in Figure 5.10.

For the classical Runge-Kutta method, the interval $I = [0, 2.83]$ (see Table 5.3). The critical time step $\triangle t_c$ as predicted by equation (5.48) becomes

$$\triangle t_c = \frac{|I|}{F}\frac{\delta^2}{\Gamma} = 0.13. \tag{5.50}$$

The four choices of time step are taken as $\triangle t = 0.14$, $\triangle t = 0.13$, $\triangle t = 0.12$, and $\triangle t = 0.01$. Figure 5.11 presents the numerical results obtained by the classical Runge-Kutta method with these time steps. From Figure 5.10 and Figure 5.11, we see that for time steps larger than or very close to the critical time step $\triangle t_c$, the numerical noise grows very quickly and soon ruins the numerical solution. For time steps below the critical time step $\triangle t_c$, the numerical noise is under control and the numerical solution converges.

Equation (5.48) is a very important guideline for selecting a suitable time step size. The fact that the spatial step size h does not appear in equation (5.48) implies that a smaller time step is not necessarily required for a smaller spatial step. This is in complete contrast with the traditional constraint on time step size that $\triangle t \leq C \cdot h/u$. However, the core size has a fundamental influence on the numerical stability and thus limits the time step size. As seen in equation (5.48), the time step size is proportional to the square of the core size. It follows that the time step has to be very small when the vortex filament is thin. This could be too restrictive and lead to extremely expensive computations. Other methods are needed to circumvent this obstacle for very thin vortex filaments.

Now we examine the effect of the spatial step size on the accuracy. We do not have a general guide for selecting a suitable spatial step size. As a matter of fact, the empirical rule obtained by studying a simple model problem cannot be simply extended to other problems. For example, the choice of $h/\delta \leq 0.5$ is adequate for calculating the propagation velocity of a vortex ring, whereas to simulate the Widnall's vortex ring instability, we have to use $h/\delta \leq 0.05$. To pick a suitable spatial step size, we compare numerical results obtained with different spatial step sizes to determine whether the numerical solution has converged. Through numerical experiments, we find that different problems require different step sizes to catch the main features of the physical process. We again use the Widnall's vortex ring instability problem to test the spatial step sizes. First we take the perturbation wavenumber $n = 2$ (a stable mode) and run simulations with the ratio of space step to core size $h/\delta = 0.40$, 0.20, 0.10 and 0.05. Figure 5.12 shows the numerical results. Clearly, for wavenumber $n = 2$, the numerical solution has already converged for $h/\delta = 0.40$. Then we take the perturbation wavenumber $n = 14$ (the unstable mode) and run simulations with $h/\delta = 0.20$, 0.10, 0.05 and 0.025. As shown in Figure 5.13, for the unstable mode $n = 14$, the numerical solution does not converge until h/δ is reduced to 0.05.

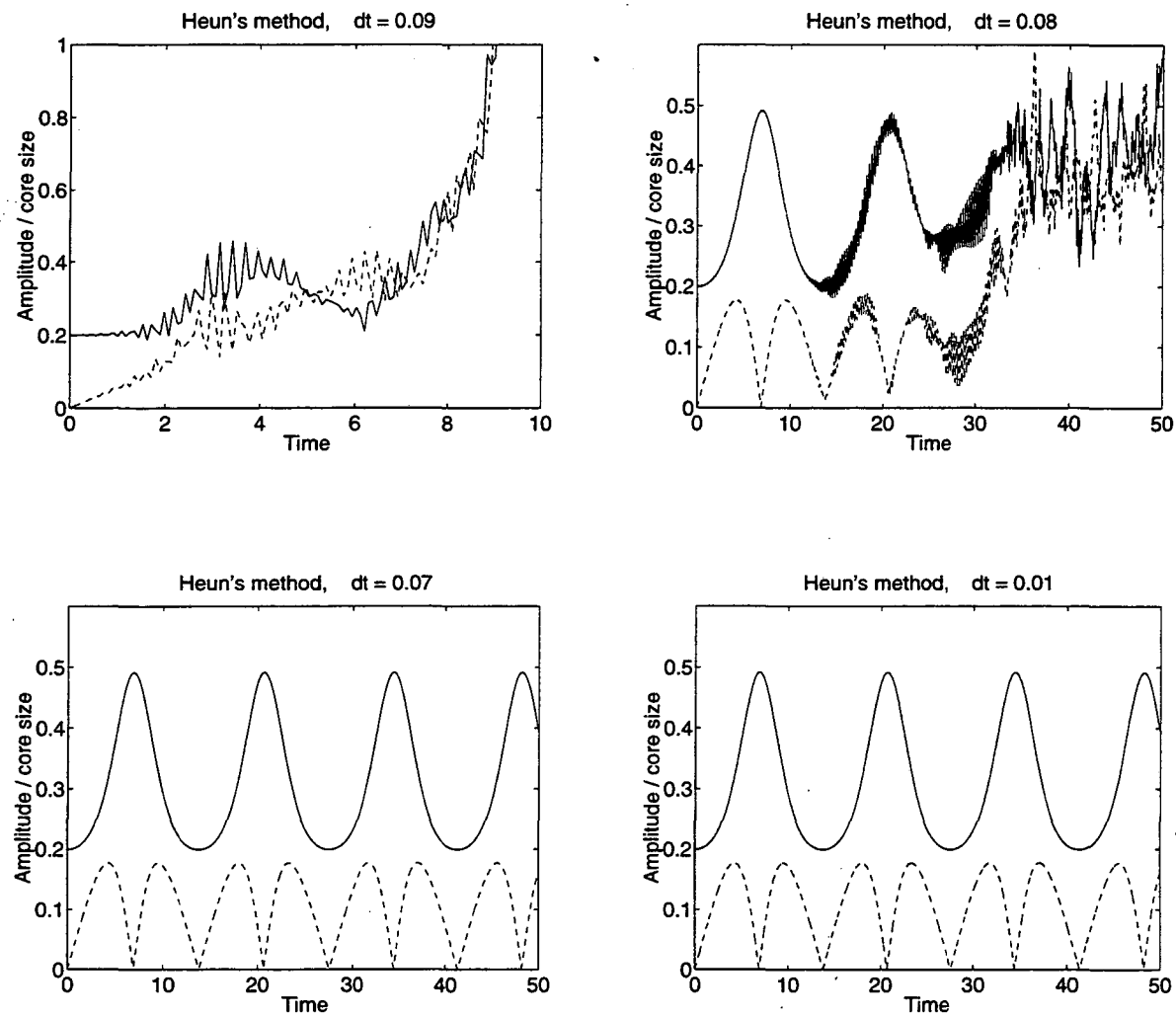

Figure 5.10: Heun third order method: Comparison of numerical results for different time steps.

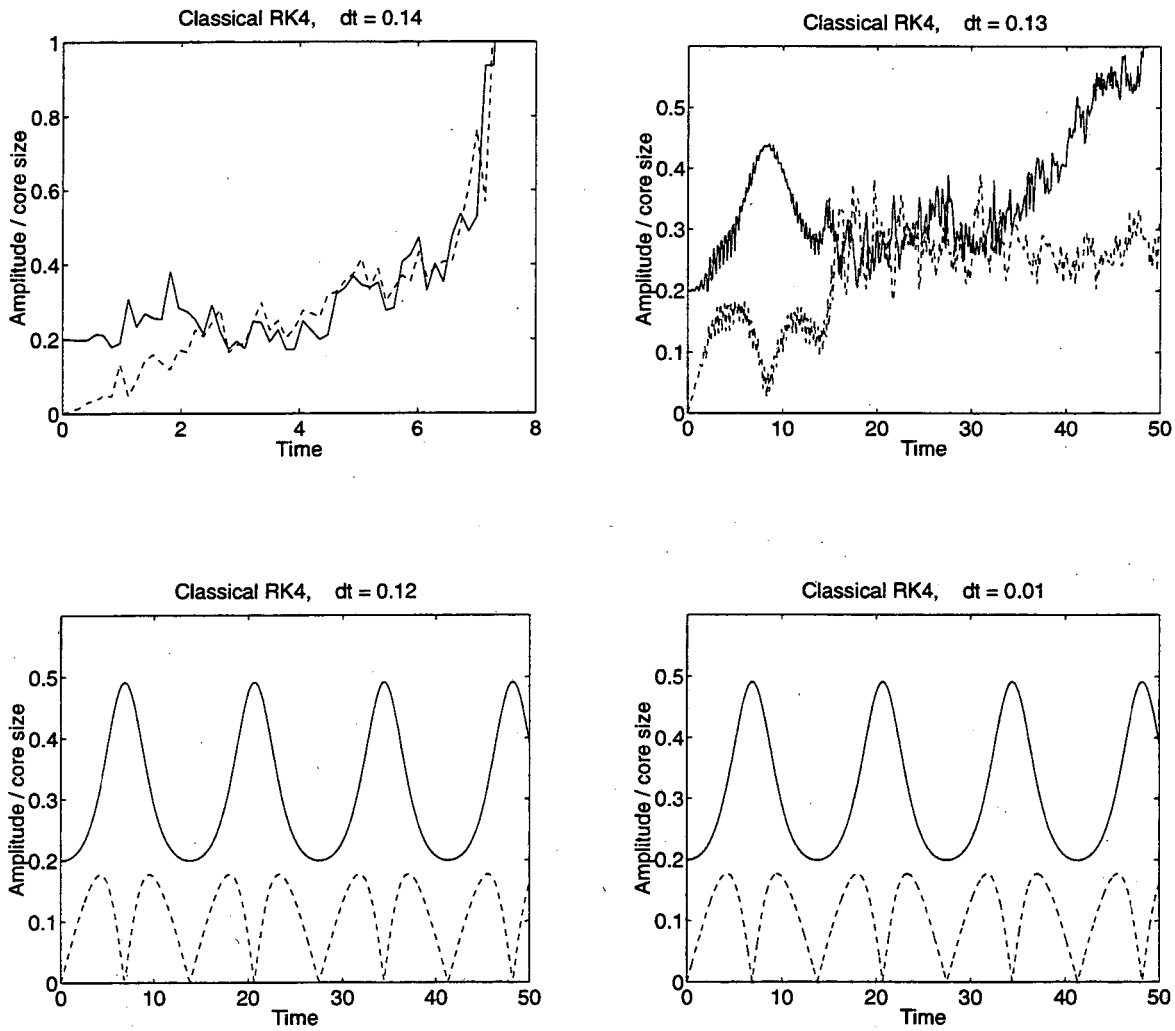

Figure 5.11: Classical fourth order Runge-Kutta method: Comparison of numerical results for different time steps.

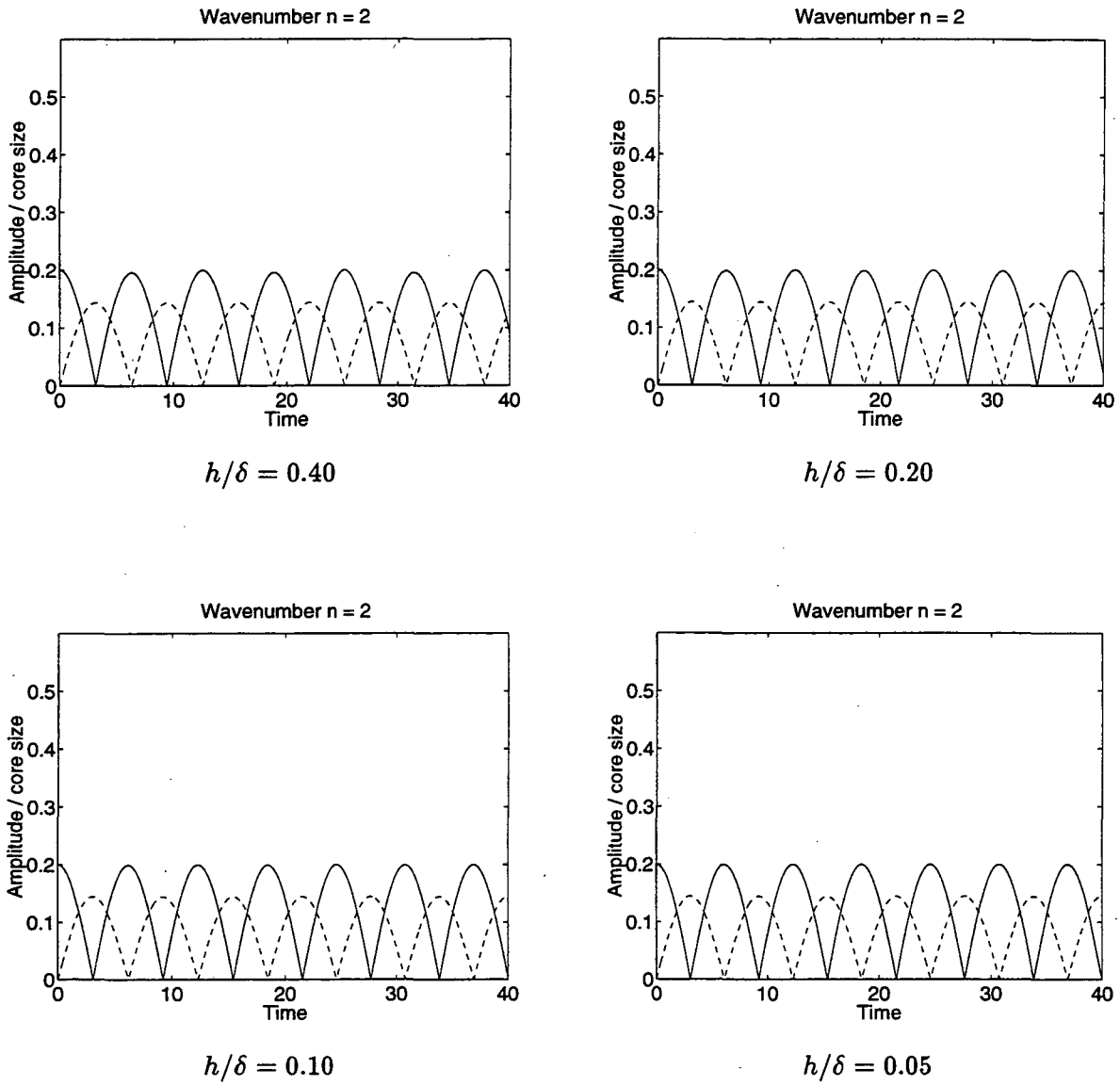

Figure 5.12: Comparison of numerical results for different h/δ.

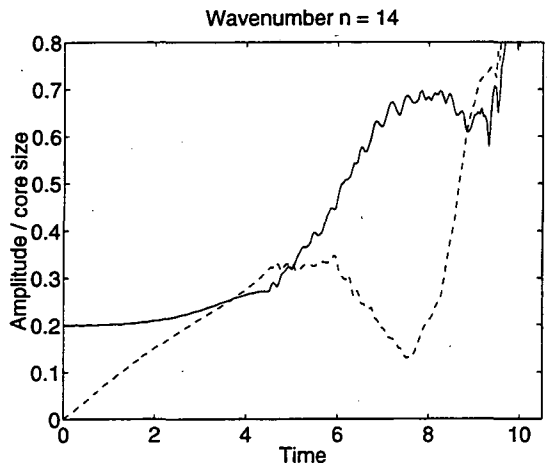

$h/\delta = 0.20$

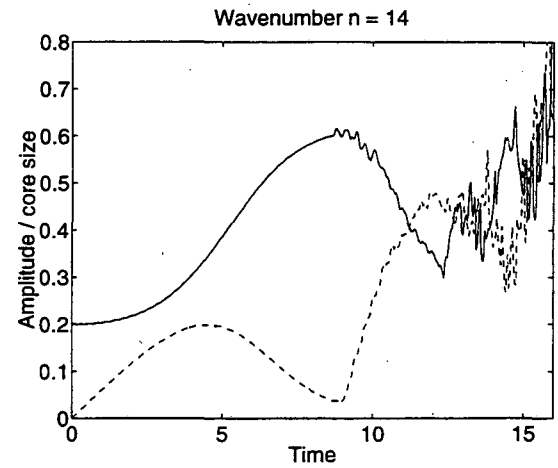

$h/\delta = 0.10$

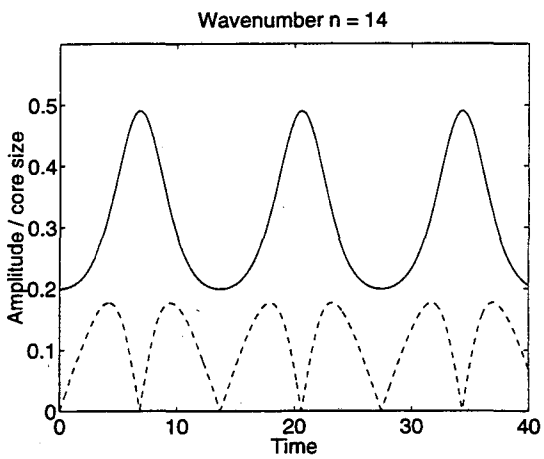

$h/\delta = 0.05$

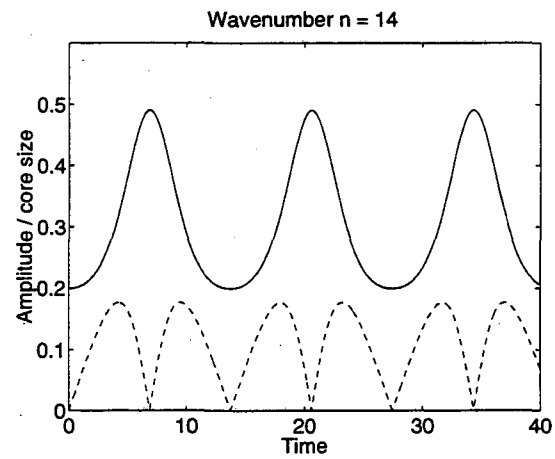

$h/\delta = 0.025$

Figure 5.13: Comparison of numerical results for different h/δ.

Chapter 6

Short Wave Instability On Vortex Filaments Of Fixed Core Structure In A Co-rotating Vorticity Field

In this chapter we investigate the short wave instability on vortex filaments of fixed core structure in a co-rotating vorticity field. The main conclusion is that neighboring vortices induce short wave unstable modes which lead to stretching and folding and that an isolated vortex filament will not create hairpins or wild stretching.

We start with a pair of co-rotating vortex filaments. In the previous chapters we reviewed Widnall's analysis of the short wave instability on a vortex ring or on an anti-parallel vortex pair. In this chapter, using an approach similar to Widnall's, we construct a theoretical analysis for the short wave instability on a co-rotating vortex pair. The motion of a short wave perturbation on a co-rotating vortex pair is governed by the rotation induced by the vortex filament which carries the wave, and by the velocity field induced by the other vortex filament. In the stability analysis of waves with small amplitude, only the linear part of velocity field induced by other filaments is needed. For a co-rotating vortex pair, the streamlines of the linearized flow are ellipses. If the vortex filament is in a continuous vorticity field or surrounded by many vortex filaments, the linearized flow is a straining flow. In the analysis, we find that the short wave instability occurs when the self-induced rotation is balanced by the linearized flow in the circumferential direction and the radial component of the linearized flow causes the wave to grow exponentially. The unstable wave

numbers form an interval which is determined by the ratio of the distance between the two vortex filaments to the core radius of the filaments. These theoretical predictions are verified in the numerical simulations. Furthermore, the numerical simulations reveal the long time behavior of the unstable wave for different separations of the vortex pair. When the ratio of the separation to the core radius is above 4.0, the amplitude of the unstable mode grows to a maximum, falls back, then starts growing and repeats the pattern. The vortex filaments alternately stretch and contract. No wild stretching is observed. In the case where the ratio of the separation to the core radius is below 4.0, the unstable mode grows without bound. The vortex filaments do not return to their original positions. Instead they stretch violently and develop hairpin-shaped small scale structures.

After the discussion of the co-rotating vortex pair, we extend our analysis to the case of a single vortex filament in a co-rotating vorticity field. We can show theoretically that the velocity field induced by a second order Gaussian vorticity distribution, if linearized around a point and viewed in the reference system attached to that point (moving and rotating with that point), is a straining flow. Marcus studied the two dimensional evolution of vortices in a shearing zonal flow [67] and showed that Jupiter's Great Red Spot is an example of two dimensional vortex equilibria in nature [66]. Here we study the evolution of the three dimensional evolution of vortex filaments with fixed core structure. When the surrounding vorticity field is discretized and represented by a set of numerical vortex filaments, numerical results indicate that the streamlines of the linearized flow are ellipses. As the vorticity field is approximated by more numerical vortex filaments, these ellipses become flatter, and the linearized flow is approximately a straining flow. Again for a vortex filament surrounded by a co-rotating vorticity field, the instability is driven by the radial component of the linearized flow while the circumferential component of the linearized flow is balanced by the self-induced rotation of the wave.

In numerical simulations using vortex methods, the wild stretching of the vortex filaments and the subsequent formation of the hairpin-shaped fine structures have been observed by many authors [26], [28], [75]. At the end of this chapter, we show that these small scale vortex structures are not caused by numerical instability, rather they are related to the short wave instability described above. The appearance of the hairpin structures drastically increases the total number of numerical vortex segments, thereby making it virtually impossible to simulate the long time physical behavior. Currently, the only way around this obstacle is Chorin's hairpin removal method [26], [28]. The hairpin removal

technique keeps the total number of numerical vortex segments at a reasonable level by removing small hairpins from the numerical solution. The hairpin removal procedure is justified by renormalization theory [28].

6.1 Short wave instability on a co-rotating vortex pair

The instability of a vortex pair has been investigated by many authors. Crow [35] studied the long wave and short wave instability for an antiparallel vortex pair. With a slightly different model and a more accurate calculation of the rotation frequency of the short wave modes, Widnall, Bliss and Tsai [95] investigated the instability of antiparallel vortex pairs and vortex rings. Recently Klein, Majda and Damodaran [56] studied the instability of long wave modes on both antiparallel vortex pairs and co-rotating vortex pairs. They found that certain long wave modes are unstable on an antiparallel vortex pair and long wave modes are always stable on a co-rotating vortex pair. However, their study is based on a simplified model equation which excludes the short wave modes from the study. In other words, their model equation is valid only for long waves.

In this section we analyze the stability of short wave modes on a co-rotating vortex pair with constant core structure. We will show that a co-rotating vortex pair always has short wave instability. Here "short wave" means the wavelength is comparable to the core radius of the vortex filaments. A perturbation wave is called "unstable" if it grows exponentially with time. A rigorous definition of stable and unstable modes will be given in the next section.

A co-rotating vortex pair consists of two parallel vortex filaments of the same circulation. As sketched in Figure 6.1 and Figure 6.2, at time $t = 0$, the two undisturbed straight vortex filaments are on the z-x plane and are parallel to the z-axis. The undisturbed pair rotates around the z-axis with angular velocity $\Gamma/\pi b^2$, where b is the separation between the two unperturbed vortex filaments and Γ is their circulation.

To better illustrate the evolution of the perturbation wave on the vortex pair, we let the x-y plane rotate along with the vortex pair such that the vortex pair is stationary in the reference system defined by the xyz-axes. The stability calculation can be done by

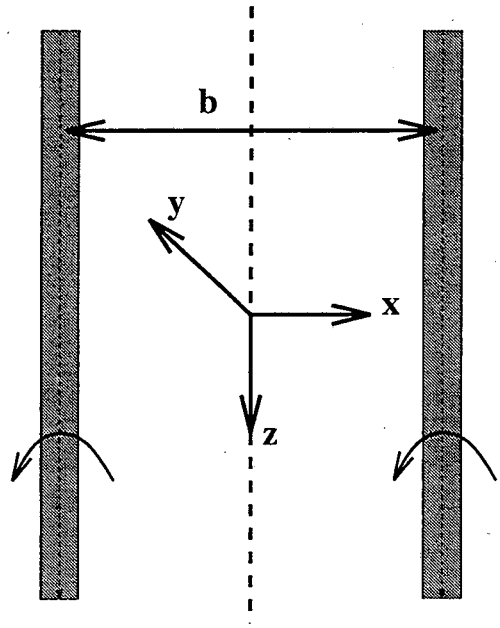

Figure 6.1: An unperturbed co-rotating vortex pair.

considering the motion of the vortex filaments that results from a sinusoidal perturbation (Figure 6.3 and Figure 6.4). The vortex filaments move with a velocity that is a combination of the self-induced rotation Ω of the sinusoidally perturbed filament and the velocity induced by the other filament. For short waves, when we calculate the velocity induced at the vortex by the neighboring filament, it is the presence of the neighboring filament rather than the perturbation on the filament that plays the dominant role. The induced velocity can be well approximated by treating the neighboring filament as unperturbed, and the contribution due to the short wave perturbation on that filament can be ignored. For simplicity, we shift the origin of the x-y plane to the unperturbed position of the vortex on the right. In Figure 6.4 the perturbed position of the vortex on the right represents the amplitude and the orientation of the sinusoidal wave on the right filament, and the vortex on the left represents the left filament which is treated as a straight unperturbed filament when we investigate the evolution of the perturbation on the right filament.

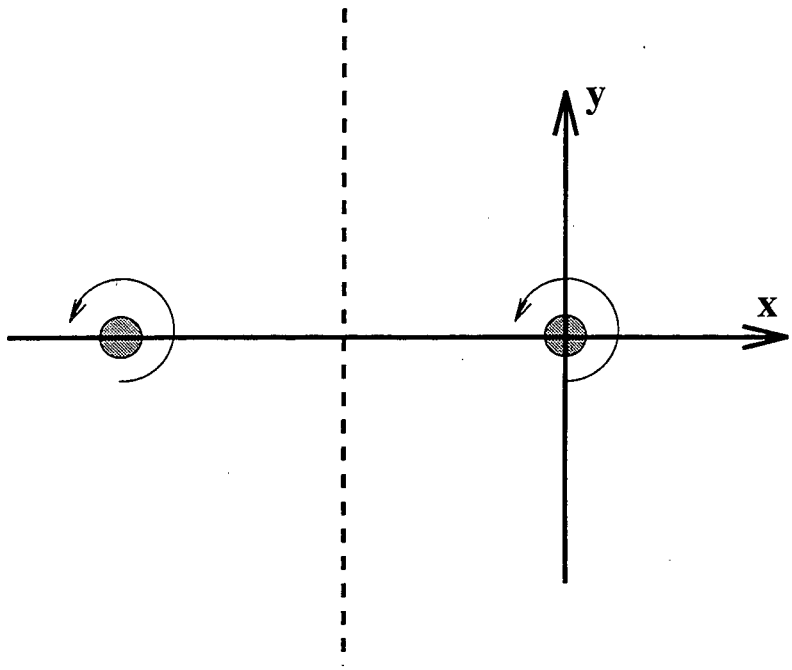

Figure 6.2: A cross-section of the unperturbed vortex pair.

The velocity at a point (x, y) induced by the left vortex is

$$\mathbf{u}(x,y) = \frac{\Gamma}{2\pi}\frac{1}{(b+x)^2+y^2}\begin{bmatrix} -y \\ b+x \end{bmatrix} - \frac{\Gamma}{\pi b^2}\begin{bmatrix} -y \\ \frac{b}{2}+x \end{bmatrix}. \tag{6.1}$$

Expanding $\mathbf{u}$ around $(0,0)$ gives

$$\mathbf{u}(x,y) = \frac{\Gamma}{2\pi b^2}\begin{bmatrix} y \\ -3x \end{bmatrix} + O(x^2+y^2). \tag{6.2}$$

The first term on the right hand side of equation (6.2) is a linearized flow whose streamlines form a family of ellipses given by

$$\frac{x^2}{\alpha} + \frac{y^2}{3\alpha} = 1 \tag{6.3}$$

with α being the free parameter. The linearized flow and its streams are sketched in Figure 6.4. In the cylindrical (r, θ) coordinate system which is centered on the unperturbed position of the right filament, this linearized flow can be written as

$$u_r(LF) = \frac{-\Gamma}{2\pi b^2}(r\sin 2\theta), \tag{6.4}$$

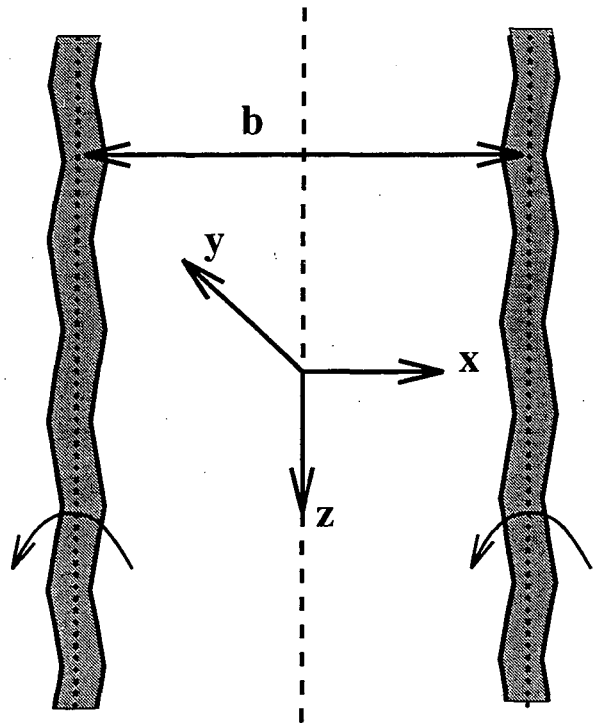

Figure 6.3: A perturbed vortex pair of the same circulation.

$$u_\theta(LF) = \frac{-\Gamma}{2\pi b^2}(2r + r\cos 2\theta), \tag{6.5}$$

where $u_r(LF)$ is the velocity component in the radial direction and $u_\theta(LF)$ is the velocity component in the tangential direction. Therefore, for the right vortex whose position is at (r_0, θ_0), the velocity induced by the left vortex is

$$u_{r_0}(LF) = \frac{-\Gamma}{2\pi b^2}(r_0 \sin 2\theta_0), \tag{6.6}$$

$$u_{\theta_0}(LF) = \frac{-\Gamma}{2\pi b^2}(2r_0 + r_0 \cos 2\theta_0). \tag{6.7}$$

In addition to the linearized flow, the displaced portion of the filament is also subject to its self-induced rotation (SR) around the unperturbed position $(0, 0)$. The self-induced tangential velocity is

$$u_\theta(SR) = -r\,\Omega, \tag{6.8}$$

where Ω is the rotation frequency of the perturbation wave.

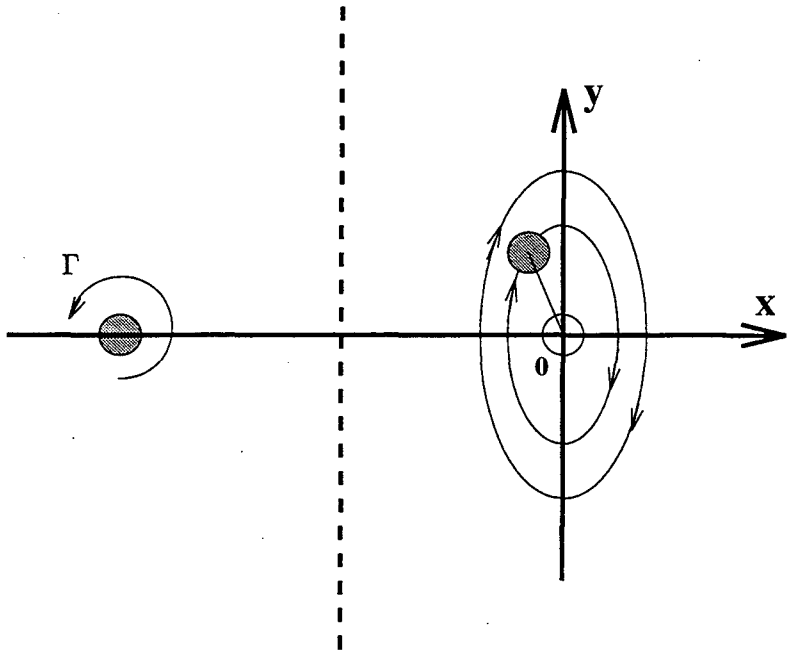

Figure 6.4: A cross-section of the perturbed vortex pair.

The total velocity of the vortex is the sum of the linearized flow and the self-induced rotation. Since the tangential velocity of the linearized flow is between $-3\Gamma r/2\pi b^2$ and $-\Gamma r/2\pi b^2$, instability is expected to occur when

$$\frac{\Gamma r}{2\pi b^2} < u_\theta(SR) < \frac{3\Gamma r}{2\pi b^2}. \tag{6.9}$$

In other words, instability happens when the tangential velocity of the linearized flow is neutralized by the self-induced rotation while the radial velocity of the linearized flow causes the perturbation wave to grow exponentially (see Figure 6.5). The process takes place in the following manner. When the self-induced rotation velocity is between $\Gamma r/2\pi b^2$ and $3\Gamma r/2\pi b^2$, the total tangential velocity turns the vortex to a new angle θ', where the total tangential velocity vanishes. At the new angle θ', one has

$$(u_\theta(LF) + u_\theta(SR))|_{\theta=\theta'} = 0, \tag{6.10}$$

and

$$\frac{\partial(u_\theta(LF) + u_\theta(SR))}{\partial\theta}|_{\theta=\theta'} < 0. \tag{6.11}$$

Substituting (6.5) and (6.8) into the above two expressions, we get

$$\frac{-\Gamma}{2\pi b^2}(2+\cos 2\theta') - \Omega = 0, \tag{6.12}$$

$$\text{and} \qquad \frac{\Gamma}{2\pi b^2}\sin 2\theta' < 0, \tag{6.13}$$

from which it follows immediately that

$$u_r(LF)|_{\theta=\theta'} = \frac{-\Gamma}{2\pi b^2} r \sin 2\theta' > 0. \tag{6.14}$$

So at $\theta = \theta'$, the perturbation wave stops rotating but it diverges along the radial direction $\theta = \theta'$ with velocity $u_r(LF) > 0$.

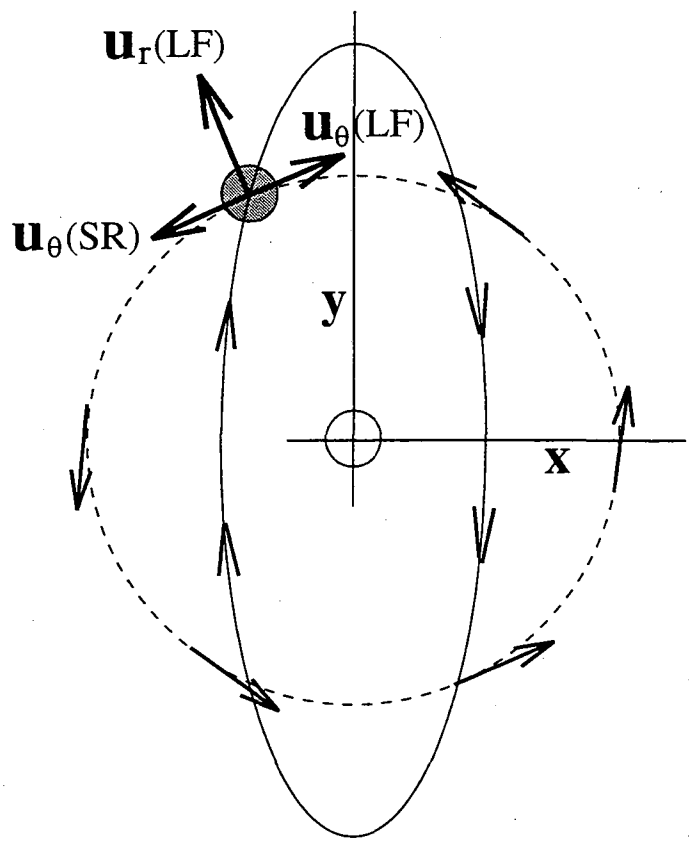

Figure 6.5: A sketch of the motion of the right filament in Fig. 6.4.

Combining equations (6.8) and (6.9), and introducing the dimensionless normal-

ized rotation frequency

$$\tilde{\Omega} = \Omega/(\frac{\Gamma}{2\pi\delta^2}), \tag{6.15}$$

one finds that the instability condition is

$$\frac{-3\delta^2}{b^2} < \tilde{\Omega}(\tilde{k}) < \frac{-\delta^2}{b^2}. \tag{6.16}$$

The normalized rotation frequency of a sinusoidal wave on a vortex filament with fixed core structure is a function of the normalized wavenumber $\tilde{k} = k\,\delta$, where k is the wavenumber and δ is the core radius.

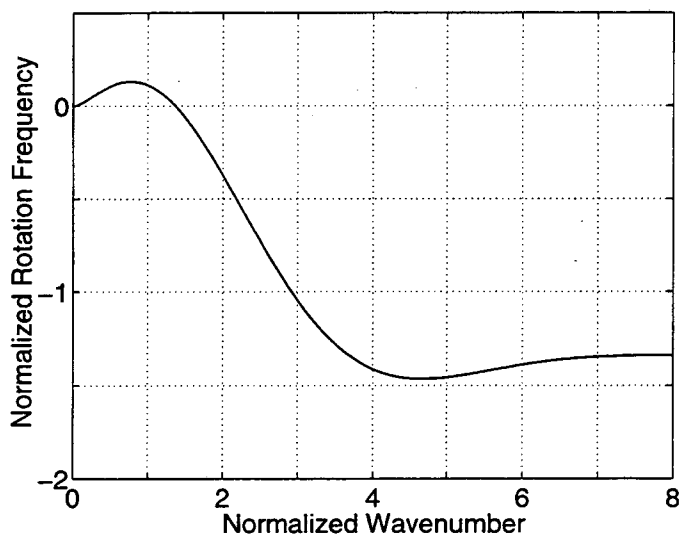

Figure 6.6: Normalized rotation frequency $\tilde{\Omega}$ as a function of normalized wavenumber $\tilde{k}$ for the core vorticity distribution derived from the cut-off function (6.17) .

Figure 6.6 depicts $\tilde{\Omega}$ as a function of $\tilde{k}$ for sinusoidal waves of small amplitude on a vortex filament whose core vorticity distribution is derived from the second order cut-off function

$$f(r) = 1 - \exp(-r^3). \tag{6.17}$$

This particular dispersion relation is obtained numerically by running simulations using the vortex method. From Figure 6.6, one can see that for each fixed $b/\delta > 1$, there is always an interval of normalized wavenumbers $\tilde{k}$ in which the normalized frequency $\tilde{\Omega}(\tilde{k})$ satisfies the instability condition (6.16). Such an interval contains the unstable modes for

the corresponding ratio of separation to core size b/δ. For example, when $b/\delta = 5.0$, the interval of the normalized unstable wavenumbers is $[1.454, 1.606]$.

We also calculated numerically the dispersion relations for the core vorticity distributions derived from the following four cut-off functions:

$$f(r) = \begin{cases} 1, & r > 1 \\ r^3, & r \leq 1 \end{cases} \tag{6.18}$$

$$f(r) = \tanh(r^3) \tag{6.19}$$

$$f(r) = 1 + (\frac{3}{2}r^3 - 1)\exp(-r^3) \tag{6.20}$$

$$f(r) = \tanh(r^3) + \frac{3}{2}r^3 \frac{1}{\cosh^2(r^3)} \tag{6.21}$$

The cut-off functions (6.17) and (6.19) have been shown by Beale and Majda [10] to give second-order convergence of the standard vortex method. The cut-off function (6.18) was used by Anderson and Greengard [4], and Almgren, Buttke and Colella [2] for the numerical simulations of the vortex ring merger problem. (6.20) and (6.21) are fourth order cut-off functions based on the corresponding second order ones (6.17) and (6.19) (see Beale and Majda [10]). Figure 6.7 displays the dispersion relations for the core vorticity distributions derived from these cut-off functions. Qualitatively these plots are very similar to the one shown in Figure 6.6. In particular, for all these dispersion functions, the range of normalized rotation frequency $\tilde{\Omega}$ contains the interval $[-1, 0]$. If $b/\delta > 1$, the intersection of the interval $[-1, 0]$ and the interval $[-3\delta^2/b^2, -\delta^2/b^2]$ is not empty and the instability condition (see equation (6.16))

$$\frac{-3\delta^2}{b^2} < \tilde{\Omega}(\tilde{k}) < \frac{-\delta^2}{b^2}$$

is certainly satisfied for some wave modes $\tilde{k}$. In other words, for $b/\delta > 1$, there always exist unstable wave modes for a co-rotating vortex pair.

What happens if b/δ is small ? When $b/\delta \leq 1$, the separation is smaller than the core radius. In this case, when we calculate the velocity at the right vortex induced by the left one, we cannot simply treat the left vortex as a point vortex. Consequently the angular velocity of the unperturbed vortex pair, which is also the rotation velocity of our reference system, is no longer $\Gamma/\pi b^2$. In the calculation of the linearized flow induced by the left vortex, the core vorticity distribution needs to be taken into consideration. We did not do

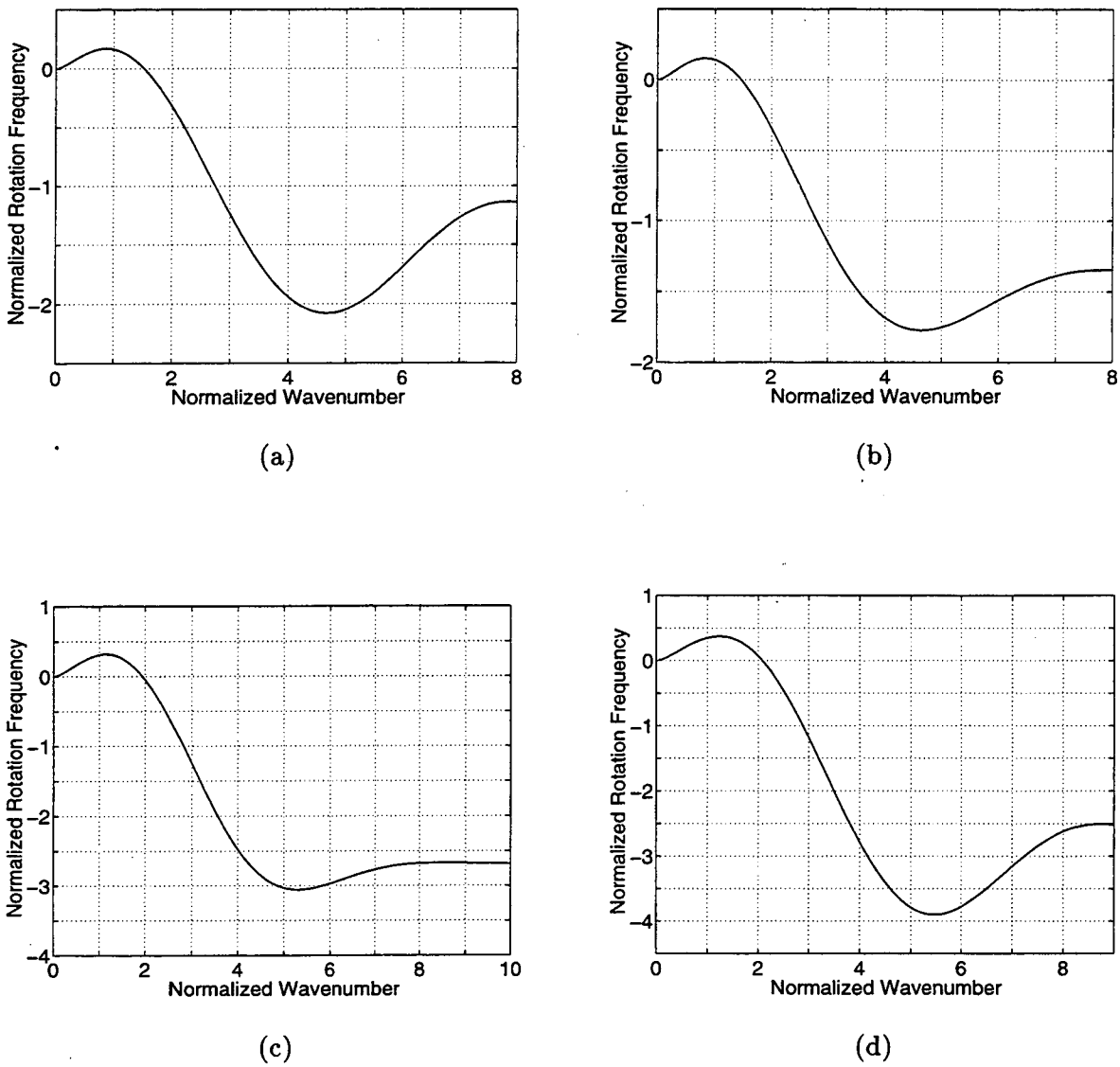

Figure 6.7: Normalized rotation frequency $\tilde{\Omega}$ as a function of normalized wavenumber $\tilde{k}$ for the core vorticity distributions determined by various cut-off functions: (a) cut-off function (6.18), (b) cut-off function(6.19), (c) cut-off function (6.20), (d) cut-off function (6.21).

this in equation (6.1) because doing so would have made the calculation complicated, and it would have been difficult to see the basic mechanism of instability.

To complete the analysis, we now derive the general formula for the linearized flow, which holds for any b/δ.

In the static (non-rotating) reference system, the velocity induced at the right vortex (x, y) by the left vortex is given by

$$\mathbf{u}_1(x,y) = \frac{\Gamma}{2\pi}\frac{1}{(b+x)^2+y^2}\begin{bmatrix} -y \\ b+x \end{bmatrix} \cdot f_{2D}\left(\frac{\sqrt{(b+x)^2+y^2}}{\delta}\right), \tag{6.22}$$

where the function $f_{2D}(r)$ is the two-dimensional cut-off function corresponding to the two-dimensional core vorticity distribution. For a straight unperturbed vortex filament, the two-dimensional core vorticity distribution can be determined by the three-dimensional cut-off function $f(r)$. Given a three-dimensional cut-off function $f(r)$, the effective two-dimensional core vorticity distribution is

$$g(r) = \int_{-\infty}^{+\infty} \frac{f'(\sqrt{r^2+z^2})}{4\pi(r^2+z^2)}\, dz. \tag{6.23}$$

Consequently, the effective two-dimensional cut-off function is

$$\begin{aligned} f_{2D}(r) &= \int_0^r g(\rho)\, 2\pi\rho\, d\rho \\ &= \int_0^r d\rho \int_{-\infty}^{+\infty} dz\, \frac{f'(\sqrt{\rho^2+z^2})}{2(\rho^2+z^2)}\,\rho. \end{aligned} \tag{6.24}$$

On the other hand, the angular velocity of the unperturbed vortex pair is

$$\Omega_{pair} = \frac{\Gamma}{\pi b^2} f_{2D}\left(\frac{b}{\delta}\right). \tag{6.25}$$

Equation (6.25) also gives the angular velocity of our reference system since the reference system is rotating with the same angular velocity as the unperturbed vortex pair.

Putting the above facts together, one finds that viewed in the rotating reference system, the velocity induced at (x, y) by the left vortex is

$$\begin{aligned} \mathbf{u}(x,y) &= \mathbf{u}_1(x,y) - \Omega_{pair}\begin{bmatrix} -y \\ \frac{b}{2}+x \end{bmatrix} \\ &= \frac{\Gamma}{2\pi}\frac{1}{(b+x)^2+y^2} f_{2D}\left(\frac{\sqrt{(b+x)^2+y^2}}{\delta}\right)\begin{bmatrix} -y \\ b+x \end{bmatrix} - \frac{\Gamma}{\pi b^2} f_{2D}\left(\frac{b}{\delta}\right)\begin{bmatrix} -y \\ \frac{b}{2}+x \end{bmatrix} \end{aligned} \tag{6.26}$$

As before, expanding $\mathbf{u}(x,y)$ around $(0,0)$, we arrive at the linearized flow

$$\mathbf{u}(x,y) = \frac{\Gamma}{2\pi b^2}\begin{bmatrix} f_{2D}(\frac{b}{\delta})\,y \\ -(3\,f_{2D}(\frac{b}{\delta}) - \frac{b}{\delta}\,f'_{2D}(\frac{b}{\delta}))\,x \end{bmatrix} + O(x^2+y^2)$$

$$\stackrel{\text{def}}{=} \frac{\Gamma}{2\pi b^2}\begin{bmatrix} c_1\,y \\ -c_2\,x \end{bmatrix} + O(x^2+y^2). \tag{6.27}$$

Here $c_1 = f_{2D}(\frac{b}{\delta})$ and $c_2 = 3\,f_{2D}(\frac{b}{\delta}) - \frac{b}{\delta}\,f'_{2D}(\frac{b}{\delta})$. For $b/\delta >> 1$, we have $f_{2D} = 1$ and $\frac{b}{\delta}\,f'_{2D}(\frac{b}{\delta}) = 0$, therefore $c_1 = 1$, $c_2 = 3$ and equation (6.27) reduces to equation (6.2).

In the cylindrical (r,θ) coordinate system, the radial component $u_r(LF)$ and the tangential component $u_\theta(LF)$ of the linearized flow are

$$u_r(LF) = -\frac{\Gamma}{2\pi b^2}\,r\,\frac{c_2-c_1}{2}\,\sin 2\theta, \tag{6.28}$$

$$u_\theta(LF) = -\frac{\Gamma}{2\pi b^2}\,r\,(\frac{c_1+c_2}{2} + \frac{c_2-c_1}{2}\,\cos 2\theta). \tag{6.29}$$

The maximum and minimum of the tangential velocity of the linearized flow $u_\theta(LF)$ are respectively $-\frac{\Gamma}{2\pi b^2}\,r\,c_1$ and $-\frac{\Gamma}{2\pi b^2}\,r\,c_2$. So instability is expected to occur when the self-induced tangential velocity $u_\theta(SR)$ is between $\frac{\Gamma}{2\pi b^2}\,r\,c_1$ and $\frac{\Gamma}{2\pi b^2}\,r\,c_2$. In terms of the normalized rotation frequency $\tilde{\Omega}$ defined in (6.15) and the normalized wavenumber $\tilde{k}$ (defined as $\tilde{k} = k\,\delta$), the instability condition reads

$$-c_2\,\frac{\delta^2}{b^2} < \tilde{\Omega}(\tilde{k}) < -c_1\,\frac{\delta^2}{b^2}. \tag{6.30}$$

Here we should point out that c_1 and c_2 are independent of (r,θ), but they depend on the cut-off function and the ratio b/δ.

As an example, we examine the case where the two-dimensional cut-off function is chosen as $f_{2D}(r) = 1-\exp(-r^2)$. This cut-off function is the two-dimensional analogue of the three-dimensional cut-off function (6.17) (see Beale and Majda [10]). In this case, the left-hand side of the inequality (6.30) becomes

$$-c_2\,\frac{\delta^2}{b^2} = -\left\{3\left[1-\exp(-\frac{b^2}{\delta^2})\right] - 2\,\frac{b^2}{\delta^2}\exp(-\frac{b^2}{\delta^2})\right\}\frac{\delta^2}{b^2}, \tag{6.31}$$

whereas the right-hand side of (6.30) is

$$-c_1\,\frac{\delta^2}{b^2} = -\left[1-\exp(-\frac{b^2}{\delta^2})\right]\frac{\delta^2}{b^2}. \tag{6.32}$$

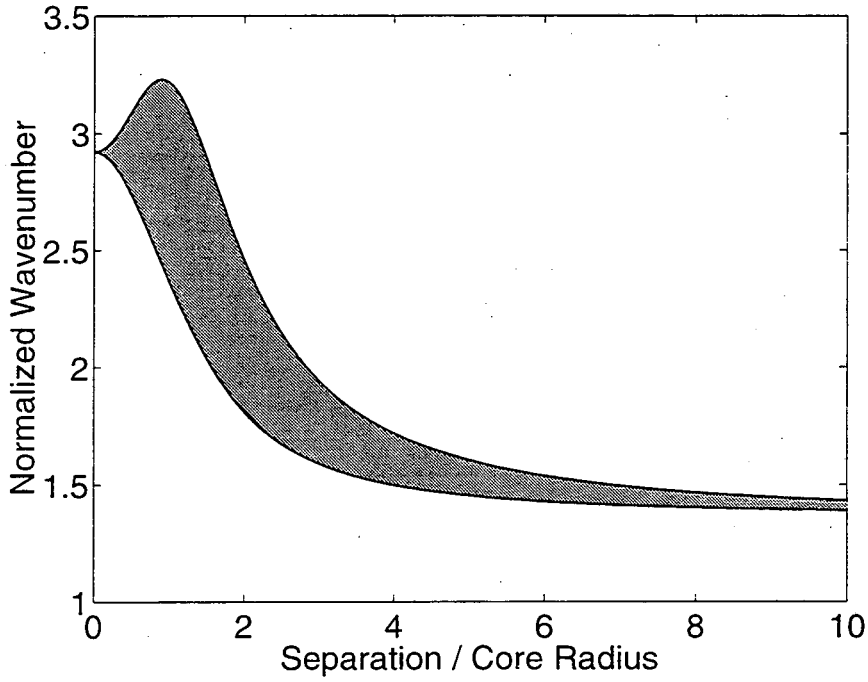

Figure 6.8: The unstable region in the $(b/\delta, \tilde{k})$ plane for a co-rotating vortex pair.

For each ratio b/δ, the interval of unstable normalized wavenumber $\tilde{k}$ can be solved numerically from the dispersion relation and the inequality (6.30). The shaded area of Figure 6.8 marks the region of instability in the $(b/\delta, \tilde{k})$ plane. Figure 6.8 indicates that for any value of b/δ, there are always unstable wave modes for the co-rotating vortex pair.

6.2 Numerical simulations of short wave instability on a co-rotating vortex pair

Now we simulate numerically the evolution of small sinusoidal perturbations on a co-rotating vortex pair using the thin tube vortex filament method. The purpose here is to verify the theoretical predictions we made in the last section and to study the long time behavior of the unstable modes.

We choose the initial conditions as follows: A pair of parallel co-rotating vortex filaments with separation b is placed in the z-x plane with the z-axis as its line of symmetry. At time $t = 0$, a cosine wave perturbation with amplitude ϵ and wave number n is imposed

on each filament in the span-wise direction. The vortex pair is perturbed in such a way that the perturbed pair remains symmetric. The size of the perturbation varies in the z-direction as $\triangle x = \pm\,\epsilon\,\cos(nz)$. In other words, initially the perturbed vortex pair has the form

$$\begin{cases} x^{(L)} = -\dfrac{b}{2} - \epsilon\,\cos(n\,z) \\ y^{(L)} = 0 \end{cases} \quad \text{and} \quad \begin{cases} x^{(R)} = \dfrac{b}{2} + \epsilon\,\cos(n\,z) \\ y^{(R)} = 0 \end{cases} \tag{6.33}$$

where the superscript "L" refers to the vortex on the left in the x-y plane at time $t = 0$, and the superscript "R" refers to the vortex on the right.

The vortex pair is periodic in the z-direction with a period equal to $2\pi/n$ or any integral multiple of $2\pi/n$. For numerical calculations, the period needs to be at least six times as large as the core radius δ. The reason for this will become clear later when we present the method for calculating the discrete Biot-Savart summation over a periodic vortex filament. So in our simulations we use the period

$$p = \left\lceil \frac{6\delta}{2\pi/n} \right\rceil \frac{2\pi}{n}. \tag{6.34}$$

We discretize the perturbed vortex pair by dividing a period of each filament into N pieces according to z coordinate. Each piece corresponds to an increment $\triangle z = p/N$ in the z direction. The length of each vortex element is approximately $\triangle z$. More specifically, the numerical discretization of the initial condition is

$$\begin{cases} x_j^{(L)} = -\dfrac{b}{2} - \epsilon\,\cos(n\,j\,\triangle z) \\ y_j^{(L)} = 0 \\ z_j^{(L)} = j\,\triangle z \end{cases} \quad \text{and} \quad \begin{cases} x_j^{(R)} = \dfrac{b}{2} + \epsilon\,\cos(n\,j\,\triangle z) \\ y_j^{(R)} = 0 \\ z_j^{(R)} = j\,\triangle z \end{cases} \tag{6.35}$$

for $j = 1, 2, ..., N$.

The total velocity at $\mathbf{x}_j^{(R)} = (x_j^{(R)}, y_j^{(R)}, z_j^{(R)})$ is the sum of the contributions from all vortex elements:

$$\begin{aligned} \mathbf{u}_j^{(R)} &= \sum_{k=-\infty}^{\infty} \frac{\Gamma}{4\pi} \triangle \mathbf{x}_{k+\frac{1}{2}}^{(R)} \times \frac{\mathbf{x}_j^{(R)} - \mathbf{x}_{k+\frac{1}{2}}^{(R)}}{|\mathbf{x}_j^{(R)} - \mathbf{x}_{k+\frac{1}{2}}^{(R)}|^3} f\left(\frac{|\mathbf{x}_j^{(R)} - \mathbf{x}_{k+\frac{1}{2}}^{(R)}|}{\delta}\right) \\ &+ \sum_{k=-\infty}^{\infty} \frac{\Gamma}{4\pi} \triangle \mathbf{x}_{k+\frac{1}{2}}^{(L)} \times \frac{\mathbf{x}_j^{(R)} - \mathbf{x}_{k+\frac{1}{2}}^{(L)}}{|\mathbf{x}_j^{(R)} - \mathbf{x}_{k+\frac{1}{2}}^{(L)}|^3} f\left(\frac{|\mathbf{x}_j^{(R)} - \mathbf{x}_{k+\frac{1}{2}}^{(L)}|}{\delta}\right) \\ &\stackrel{\text{def}}{=} \mathbf{u}_{right} + \mathbf{u}_{left}, \end{aligned} \tag{6.36}$$

where Γ is the circulation, δ is the core radius, $\triangle \mathbf{x}^{(R)}_{k+\frac{1}{2}} = \mathbf{x}^{(R)}_{k+1} - \mathbf{x}^{(R)}_{k}$, $\mathbf{x}^{(R)}_{k+\frac{1}{2}} = \frac{1}{2}(\mathbf{x}^{(R)}_{k+1} + \mathbf{x}^{(R)}_{k})$, and $\triangle \mathbf{x}^{(L)}_{k+\frac{1}{2}}$ and $\mathbf{x}^{(L)}_{k+\frac{1}{2}}$ are defined in the same way for the left filament. In the simulations, we use the second order cut-off function $f(r) = 1 - \exp(-r^3)$.

In equation (6.36), $\mathbf{u}_{right}$ is the velocity induced by the right filament and $\mathbf{u}_{left}$ is the velocity induced by the left one, both of which can be evaluated as follows. We rewrite $\mathbf{u}_{right}$ as

$$\begin{aligned}
\mathbf{u}_{right} = & \sum_{k=-N/2+j}^{N/2} \left[\frac{\Gamma}{4\pi} \triangle \mathbf{x}^{(R)}_{k+\frac{1}{2}} \times \frac{\mathbf{x}^{(R)}_{j} - \mathbf{x}^{(R)}_{k+\frac{1}{2}}}{|\mathbf{x}^{(R)}_{j} - \mathbf{x}^{(R)}_{k+\frac{1}{2}}|^3} f\left(\frac{|\mathbf{x}^{(R)}_{j} - \mathbf{x}^{(R)}_{k+\frac{1}{2}}|}{\delta}\right) \right. \\
& \left. + \sum_{l=\pm 1}^{\pm\infty} \frac{\Gamma}{4\pi} \triangle \mathbf{x}^{(R)}_{k+\frac{1}{2}} \times \frac{\mathbf{x}^{(R)}_{j} - \mathbf{x}^{(R)}_{k+\frac{1}{2}} + l\,p\,\mathbf{e}_z}{|\mathbf{x}^{(R)}_{j} - \mathbf{x}^{(R)}_{k+\frac{1}{2}} + l\,p\,\mathbf{e}_z|^3} \right] \\
\stackrel{\text{def}}{=} & \sum_{k=-N/2+j}^{N/2} \left[\mathbf{w}_1(\mathbf{x}^{(R)}_{k+\frac{1}{2}}) + \mathbf{w}_2(\mathbf{x}^{(R)}_{k+\frac{1}{2}}) \right],
\end{aligned} \tag{6.37}$$

where $\mathbf{e}_z$ is the unit vector in z-direction, $\mathbf{w}_1(\mathbf{x}^{(R)}_{k+\frac{1}{2}})$ is the velocity contribution from the vortex element $\mathbf{x}^{(R)}_{k+\frac{1}{2}}$ which lies within half period to the point $\mathbf{x}^{(R)}_{j}$, $\mathbf{w}_2(\mathbf{x}^{(R)}_{k+\frac{1}{2}})$ is the sum of contributions from all images of $\mathbf{x}^{(R)}_{k+\frac{1}{2}}$. In [53] Klein and Knio introduced a method to reduce the infinite summation in $\mathbf{w}_2(\mathbf{x}^{(R)}_{k+\frac{1}{2}})$ to an evaluation of two functions. Here we use a technique similar to that of Klein and Knio but with a more efficient and more accurate way of calculating the two functions F and G which are defined below. For the sake of simplicity, we will write $\mathbf{x}^{(R)}_{k+\frac{1}{2}}$ as $\mathbf{x}$, $\triangle \mathbf{x}^{(R)}_{k+\frac{1}{2}}$ as $\triangle \mathbf{x}$, and $\mathbf{x}^{(R)}_{j}$ as $\mathbf{x}_0$. Then we get

$$\begin{aligned}
\mathbf{w}_2(\mathbf{x}) &= \frac{\Gamma}{4\pi} \sum_{l=\pm 1}^{\pm\infty} \frac{\triangle \mathbf{x} \times (\mathbf{x}_0 - \mathbf{x}) + (\triangle \mathbf{x} \times \mathbf{e}_z)\, l\, p}{|\mathbf{x}_0 - \mathbf{x} + l\,p\,\mathbf{e}_z|^3} \\
&= \frac{\Gamma}{4\pi} \left[\triangle \mathbf{x} \times (\mathbf{x}_0 - \mathbf{x}) \frac{1}{p^3} \sum_{l=\pm 1}^{\pm\infty} \frac{1}{|\frac{\mathbf{x}_0 - \mathbf{x}}{p} + l\,\mathbf{e}_z|^3} \right. \\
&\quad \left. + (\triangle \mathbf{x} \times \mathbf{e}_z) \frac{1}{p^2} \sum_{l=\pm 1}^{\pm\infty} \frac{l}{|\frac{\mathbf{x}_0 - \mathbf{x}}{p} + l\,\mathbf{e}_z|^3} \right] \\
&= \frac{\Gamma}{4\pi} \left[\triangle \mathbf{x} \times (\mathbf{x}_0 - \mathbf{x}) \frac{1}{p^3} F(a_1, a_2) + (\triangle \mathbf{x} \times \mathbf{e}_z) \frac{1}{p^2} G(a_1, a_2) \right],
\end{aligned} \tag{6.38}$$

where $\mathbf{x}_0 = (x_0, y_0, z_0)$, $\mathbf{x} = (x, y, z)$, and

$$a_1 = \frac{z_0 - z}{p}, \tag{6.39}$$

$$a_2 = \frac{(x_0 - x)^2 + (y_0 - y)^2}{p^2}, \tag{6.40}$$

$$F(a_1, a_2) = \sum_{l=\pm 1}^{\pm\infty} \frac{1}{[(l + a_1)^2 + a_2]^{3/2}}, \tag{6.41}$$

$$G(a_1, a_2) = \sum_{l=\pm 1}^{\pm\infty} \frac{l}{[(l + a_1)^2 + a_2]^{3/2}}. \tag{6.42}$$

The functions $F(a_1, a_2)$ and $G(a_1, a_2)$ can be evaluated accurately up to the machine error. In the following we give an efficient algorithm for calculating F and G.

Let

$$a = 2d_1 \tag{6.43}$$

$$b = d_1^2 + d_2 \tag{6.44}$$

We can write F as

$$\begin{aligned} F(d_1, d_2) &= \sum_{k=1}^{\infty} \left(\frac{1}{[(k + d_1)^2 + d_2]^{3/2}} + \frac{1}{[(-k + d_1)^2 + d_2]^{3/2}} \right) \\ &= \sum_{k=1}^{\infty} \frac{1}{k^3} [(1 + \frac{a}{k} + \frac{b}{k^2})^{-3/2} + (1 - \frac{a}{k} + \frac{b}{k^2})^{-3/2}] \end{aligned} \tag{6.45}$$

The power series expansion reads

$$(1 + t)^{-3/2} = 1 + \alpha_1 t + \alpha_2 t^2 + ... + \alpha_n t^n + ... \tag{6.46}$$

where

$$\alpha_1 = -3/2, \tag{6.47}$$

$$\alpha_{k+1} = \alpha_k \frac{-(2k + 1)}{2k}, \quad k = 1, 2, ... \tag{6.48}$$

Hence

$$(1 + \frac{a}{k} + \frac{b}{k^2})^{-3/2} + (1 - \frac{a}{k} + \frac{b}{k^2})^{-3/2} = 2[\beta_0 + \beta_1 k^{-2} + \beta_2 k^{-4} + ... + \beta_n k^{-2n} + ...] \tag{6.49}$$

where

$$\beta_0 = 1 \tag{6.50}$$

$$\beta_1 = \alpha_1 b + \alpha_2 a^2 \tag{6.51}$$

$$\beta_2 = \alpha_2 b^2 + 3\alpha_3 b a^2 + \alpha_4 a^4 \tag{6.52}$$

$$..... \tag{6.53}$$

$$\beta_n = \alpha_n C_n^1 b^n a^n + \alpha_{n+1} C_{n+1}^2 b^{n-1} a^2 + \alpha_{n+2} C_{n+2}^4 b^{n-2} a^4 + ... + \alpha_{2n} C_{2n}^{2n} b^0 a^{2n} \tag{6.54}$$

It follows that

$$F(d_1,d_2) = \sum_{k=1}^{N}\left(\frac{1}{[(k+d_1)^2+d_2]^{3/2}} + \frac{1}{[(-k+d_1)^2+d_2]^{3/2}}\right) + 2\sum_{j=0}^{L}\beta_j\left(\sum_{k=N+1}^{\infty}\frac{1}{k^{2j+3}}\right) + O\left(\frac{1}{N^{2L+4}}\right) \tag{6.55}$$

Introducing the notation

$$I(N,p) = \sum_{k=N+1}^{\infty}\frac{1}{k^p} \tag{6.56}$$

and using the expansions

$$\left(1-\frac{1}{2k}\right)^{-p} = 1+\sum_{i=1}^{\infty}\frac{p(p+1)...(p+i-1)}{i!\,2^i}\left(\frac{1}{k}\right)^i \tag{6.57}$$

$$\left(1+\frac{1}{2k}\right)^{-p} = 1+\sum_{i=1}^{\infty}\frac{p(p+1)...(p+i-1)}{i!\,2^i}\left(-\frac{1}{k}\right)^i \tag{6.58}$$

we have

$$\left(1-\frac{1}{2k}\right)^{-p}-\left(1+\frac{1}{2k}\right)^{-p} = \frac{p}{k}+\sum_{l=1}^{\infty}\frac{p(p+1)...(p+2l)}{(2l+1)!\,2^{2l}}\left(\frac{1}{k}\right)^{2l+1} \tag{6.59}$$

Combining the identity

$$\left(k-\frac{1}{2}\right)^{-p}-\left(k+\frac{1}{2}\right)^{-p} = \frac{1}{k^p}\left[\left(1-\frac{1}{2k}\right)^{-p}-\left(1+\frac{1}{2k}\right)^{-p}\right] \tag{6.60}$$

with equation (6.59), we obtain

$$\left(k-\frac{1}{2}\right)^{-p}-\left(k+\frac{1}{2}\right)^{-p} = \frac{p}{k^{p+1}}+\sum_{l=1}^{\infty}\frac{p(p+1)...(p+2l)}{(2l+1)!\,2^{2l}}\left(\frac{1}{k}\right)^{2l+1+p}, \tag{6.61}$$

which leads to

$$\frac{1}{k^{p+1}} = \frac{1}{p}\left[\frac{1}{(k-\frac{1}{2})^p}-\frac{1}{(k+\frac{1}{2})^p}\right]-\sum_{l=1}^{\infty}\frac{(p+1)...(p+2l)}{(2l+1)!\,2^{2l}}\left(\frac{1}{k}\right)^{2l+1+p}, \tag{6.62}$$

i.e.

$$\frac{1}{k^p} = \frac{1}{p-1}\left[\frac{1}{(k-\frac{1}{2})^{p-1}}-\frac{1}{(k+\frac{1}{2})^{p-1}}\right]-\sum_{l=1}^{\infty}\frac{p...(p+2l-1)}{(2l+1)!\,2^{2l}}\left(\frac{1}{k}\right)^{2l+p}. \tag{6.63}$$

As an immediate consequence, we have

$$I(N,p) = \sum_{k=N+1}^{\infty}\frac{1}{k^p} = \frac{1}{p-1}\frac{1}{(N+\frac{1}{2})^{p-1}}-\sum_{l=1}^{\infty}\frac{p...(p+2l-1)}{(2l+1)!\,2^{2l}}I(N,p+2l)$$

$$= \frac{1}{p-1}\frac{1}{(N+\frac{1}{2})^{p-1}}-\sum_{l=1}^{p+2l\le 2L+3}\frac{p...(p+2l-1)}{(2l+1)!\,2^{2l}}I(N,p+2l)+O\left(\frac{1}{N^{2L+4}}\right) \tag{6.64}$$

Therefore, the function $F(d_1, d_2)$ can be evaluated using equations (6.55) and (6.64). For $|d_1| \leq 0.5$ and $|d_2| \leq 0.5$, the choice of $N = 14$ and $L = 5$ is sufficient to keep the maximum relative error bounded by 10^{-15}.

The evaluation of the function $G(d_1, d_2)$ is similar.

The term $\mathbf{u}_{right}$ is obtained numerically by summing up $\mathbf{w}_1(\mathbf{x}^{(R)}_{k+\frac{1}{2}})$ and $\mathbf{w}_2(\mathbf{x}^{(R)}_{k+\frac{1}{2}})$. The term $\mathbf{u}_{left}$ can be calculated in a similar way. The filaments are advected in time using the classical fourth order Runge-Kutta method.

We start by setting the separation $b = 1.0$, the core size $\delta = 0.1$, and the perturbation amplitude $\epsilon = 0.01$. Figure 6.9 shows the time evolution of the amplitudes of perturbations for different wavenumbers; $k = 13.70$ and $k = 14.70$ are stable modes whereas $k = 14.10$ and $k = 14.30$ are unstable modes. For $k = 13.70$, in the reference system which is rotating along with the vortex pair the linearized flow prevails over the self-induced rotation. The perturbation wave rotates clockwise following the linearized flow. The amplitude of the perturbation fluctuates due to the fact that the linearized flow is not a perfectly circular rotation. For $k = 14.70$, the self-induced rotation dominates the linearized flow. The perturbation wave rotates counter-clockwise and is driven by the self-induced rotation. For $k = 14.10$ and $k = 14.30$, and actually for any wavenumber k in the interval $[13.89, 14.31]$ of unstable wave numbers for the ratio $b/\delta = 10.0$, the self-induced rotation velocity is between the minimum and maximum tangential velocity of the linearized flow. Initially, the amplitude of the perturbation grows exponentially. After reaching a maximum, the amplitude falls back to where it started, then it rises again and repeats the pattern.

In the above description of the behavior of the stable and unstable modes, several issues need to be clarified. The first is how to draw a clear distinction between the stable and unstable modes. From Figure 6.9 one sees that none of the perturbation waves grows without limit. One may argue that all these perturbation modes should be called stable modes. The method we use to distinguish instabilities from fluctuations is to compare the maximum amplitude that the perturbation wave reaches with its initial amplitude. If the maximum amplitude of the perturbation wave is bounded by a constant multiple of its initial amplitude, we call it stable. If this is not true, that is, if the perturbation wave always grows over a certain value no matter how small the initial amplitude is, then we call it unstable. This is exactly the same criterion that we used in Chapter 4 when we simulated Widnall's instability on vortex rings.

Figure 6.10 shows the time evolution of the perturbation wave with wavenumber

$k = 13.70$ for the initial perturbation amplitudes $\epsilon = 0.02$, $\epsilon = 0.01$, $\epsilon = 0.005$ and $\epsilon = 0.0025$. It is clear from Figure 6.10 that as the initial amplitude gets smaller, so does the maximum amplitude of the perturbation. The perturbation wave is bounded by a constant multiple of the initial amplitude, where, more precisely, the constant is 2. Hence, according to the criterion we discussed above, the mode $k = 13.70$ is stable. In Figure 6.11, we display the time evolution of the perturbation wave with wavenumber $k = 14.30$ for the initial perturbation amplitudes $\epsilon = 0.02$, $\epsilon = 0.01$, $\epsilon = 0.005$, and $\epsilon = 0.0025$. Figure 6.11 illustrates the typical behavior of an unstable mode. Unlike what we see in the case of $k = 13.70$, the maximum amplitude of the perturbation wave always reaches a certain value no matter how small the initial amplitude is. As can be seen in Figure 6.11, the maximum amplitude is roughly 0.4δ. Thus the mode $k = 14.30$ is unstable.

The second issue about the perturbation wave is the repeating pattern of the unstable mode. As shown in Figure 6.11, after reaching a maximum, the perturbation amplitude decreases until it reaches the initial value and then starts rising again. To explain this up-and-down behavior of the unstable mode, we need to consider the effect of the amplitude on the dispersion relation. The dispersion relations displayed in Figure 6.6 and Figure 6.7 are for perturbation waves of small amplitude (i.e. the amplitude is small in comparison with the wavelength). Recall that in Chapter 4, when numerically simulating the Widnall's instability of a vortex ring, we studied the normalized rotation frequency as a function of the amplitude for several wavenumbers. Figure 6.12 shows the plots of the normalized rotation frequency vs the normalized amplitude for $k\,\delta = 1.4$, 1.45 and 1.5. The general conclusion is that for a fixed wavenumber, the normalized rotation frequency increases as the amplitude increases. In the coordinate system which is rotating with the vortex pair, the self-induced tangential velocity is $u_\theta(SR) = -r\,\frac{\Gamma}{2\pi\delta^2}\,\tilde{\Omega}$, where $\tilde{\Omega}$ is the normalized rotation frequency (see equation (6.8) and (6.15)). Therefore in the coordinate system shown in Figure 6.2, the self-induced rotation velocity $u_\theta(SR)$ decreases as the amplitude increases. With this principle in mind, we can qualitatively sketch the motion of the peak of the unstable modes. As illustrated in Figure 6.13, the unstable perturbation wave starts from its initial position (point A). At point A, $\theta = \pi$, the tangential velocity of the linearized flow $u_\theta(LF) = -\frac{\Gamma}{2\pi b^2}(2\,r + r\,\cos 2\theta)$ attains its minimum (the tangential velocity is negative and its absolute value attains the maximum). The self-induced rotation is not strong enough to counter the linearized flow. Hence the perturbation wave rotates clockwise and grow slowly in its magnitude due to the radial component of the linearized flow

$u_r(LF) = -\frac{\Gamma}{2\pi b^2}(r \sin 2\theta)$. As the perturbation wave approaches point B, the tangential velocity of the linearized flow becomes weaker. When it reaches point B, the linearized flow is balanced in the tangential direction by the self-induced rotation. So, from point B to point C, the perturbation wave grows exponentially in the radial direction while it is not moving much in the tangential direction. It would have grown without bound in the radial direction if the self-induced angular velocity Ω did not depend on the amplitude. However, as the amplitude increases the self-induced angular velocity decreases. Thus the linearized flow once again overcomes the self-induced rotation and turns the perturbation wave from point C to point D. At point D, $\theta = \pi/2$, the radial velocity of the linearized flow is zero. Beyond point D, the perturbation wave continues to rotate clockwise while its amplitude decreases because the radial velocity of the linearized flow is negative. Eventually it arrives at point G. At point G, the perturbation wave has rotated an angle of π around the unperturbed vortex filament and its amplitude is back to its initial value. After another half cycle from point G to point A, the perturbation wave arrives back at its original position.

Now we continue to examine the evolution of the unstable modes for different ratios of separation to core radius b/δ. We ran simulations with $b/\delta = 10$, 9, 8, 7, 6, 5, 4, 3 and 2. The numerical results are shown in Figure 6.14, Figure 6.15 and Figure 6.16. For $b/\delta > 4$, the time evolutions of the unstable modes are similar to those shown in Figure 6.14 (a) where $b/\delta = 10$. The amplitude of the perturbation grows to a maximum, decreases to its original value and then repeats the pattern. One thing to note is that for a fixed core radius, as the separation becomes smaller, the perturbation wave can grow to a larger amplitude. This phenomenon can be seen by comparing the amplitude plots of the perturbation waves for various separations in Figure 6.14 and Figure 6.15. In the plots the vertical axis represents the dimensionless quantity: the ratio of amplitude to core size. Figure 6.14 and Figure 6.15 indicate that the maximum amplitude that the perturbation wave can reach is given by the product of the core radius and a decreasing function of b/δ. Thus for a co-rotating vortex pair of very thin filaments (i.e. b/δ is large), the short wave instability is not prominent, and the unstable modes are negligible compared with the scale of the separation. For $b/\delta < 4$, the unstable modes behave differently from the case where $b/\delta > 4$. Although the perturbation wave may not increase monotonically due to its rotation around the unperturbed position of the filament, it does not return to its original position. In our numerical simulations, we observed that the perturbation wave grows, bends and becomes non-planar. After that, the thin hairpin structures appear and wrap

around the filament. Figure 6.16 shows the plot of amplitude vs time with the separation $b = 0.2$ and the core size $\delta = 0.1$. The amplitude of the perturbation wave grows until it becomes greater than half of the separation: at this point, the two perturbed filaments get very close to each other and become tangled together. After that, it is impossible for the filaments to separate from each other and to return to their original position. Figure 6.17 shows the configuration of the two filaments after they are tangled together. Recall that in Figure 6.13, we sketched the theoretical explanation for the repeating pattern behaviors of the unstable modes. One may wonder: Does that analysis contradicts the wild behaviors of the unstable modes observed here for $b/\delta < 4$? The answer is no. The analysis shown in Figure 6.13 is based on an extended linear analysis. In that analysis, the amplitude of the unstable mode is allowed to be comparable to the core radius. However, in that analysis we also assumed that the amplitude of the perturbation mode is much smaller than the separation between the filaments so that the motion of the perturbed filament due to the other filament relative to its unperturbed position is well approximated by a linearized flow. As the separation decreases, this approximation becomes more and more inaccurate. Thus the analysis sketched in Figure 6.13 is only good for large ratios of separation to core radius. In particular, when the separation is comparable to the core size and the amplitude of the perturbation wave grows to a value comparable to the core size, the two filaments become tangled together and the linear theory fails in this case. That is why the unstable modes grow without bound when the two filaments are close to each other. When the two filaments are far apart, as we already shown in Figures 6.14 and 6.15 the behaviors of the unstable modes are indeed repeating patterns.

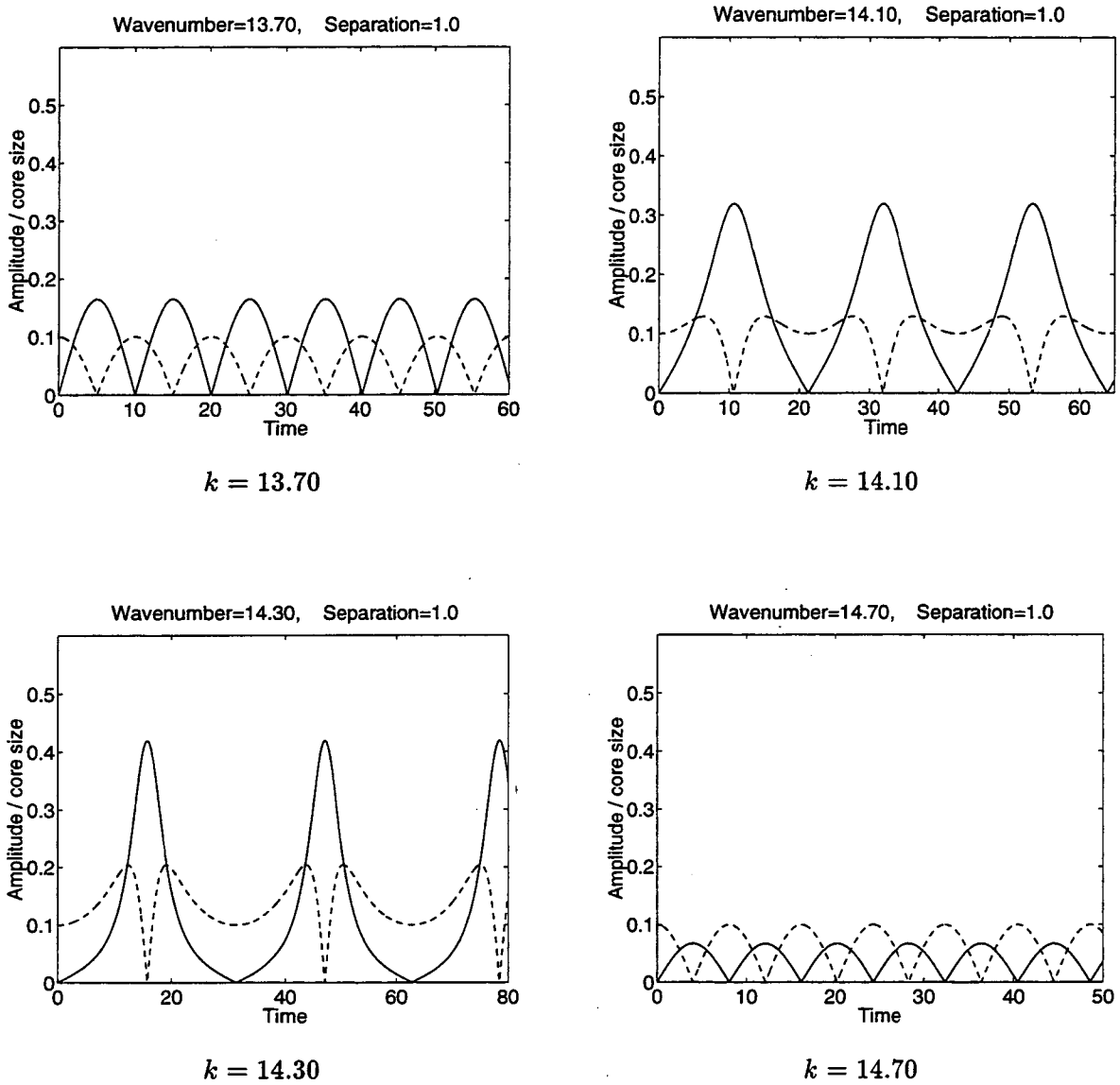

Figure 6.9: Time evolution of the perturbations of different wavenumbers on a pair of co-rotating vortex filaments. Dashed line : amplitude in the x-direction (spanwise direction); Solid line : amplitude in the y-direction. The coordinate system is rotating with the vortex pair.

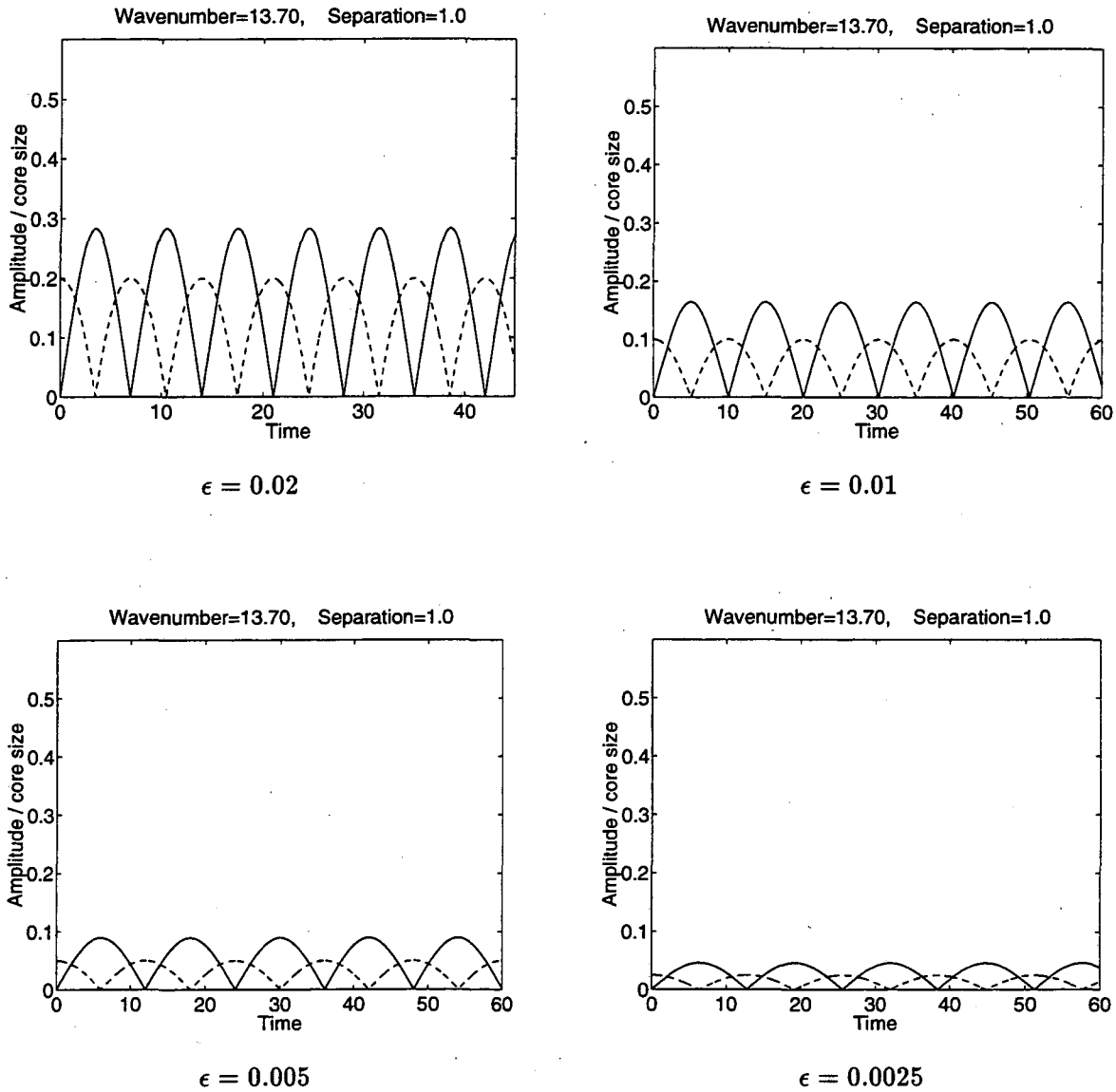

Figure 6.10: Time evolution of the perturbations with different initial amplitudes on a pair of co-rotating vortex filaments. Dashed line : amplitude in the x-direction (spanwise direction); Solid line : amplitude in the y-direction. The coordinate system is rotating with the vortex pair.

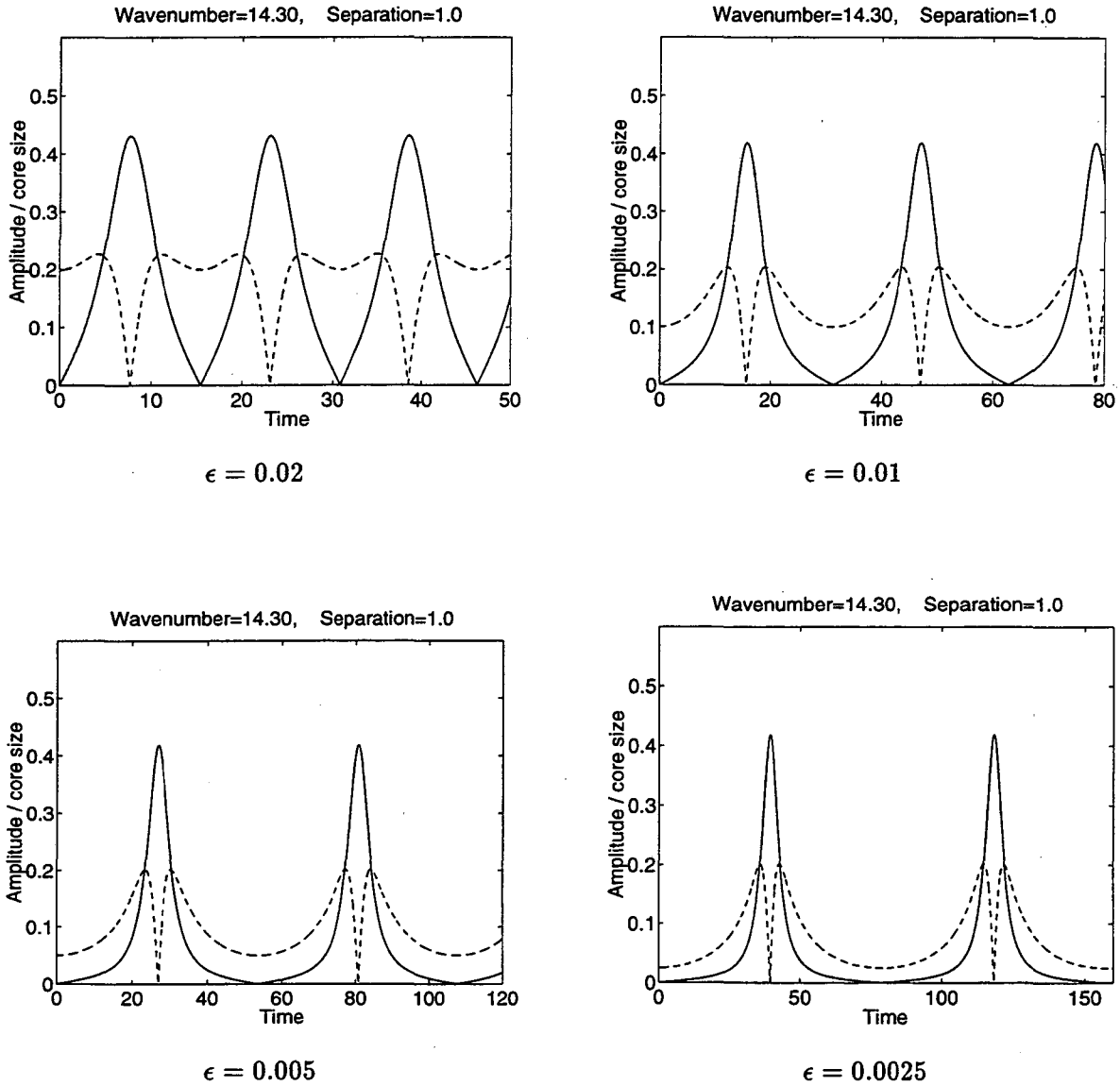

Figure 6.11: Time evolution of the perturbations with different initial amplitudes on a pair of co-rotating vortex filaments. Dashed line : amplitude in the x-direction (spanwise direction); Solid line : amplitude in the y-direction. The coordinate system is rotating with the vortex pair.

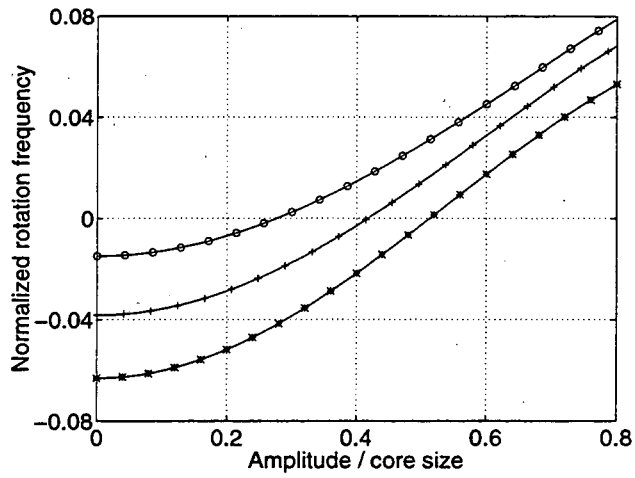

Figure 6.12: Normalized rotation frequency vs amplitude/core radius. $-o-$: $k\,\delta = 1.40$; $-+-$: $k\,\delta = 1.45$; $-*-$: $k\,\delta = 1.50$.

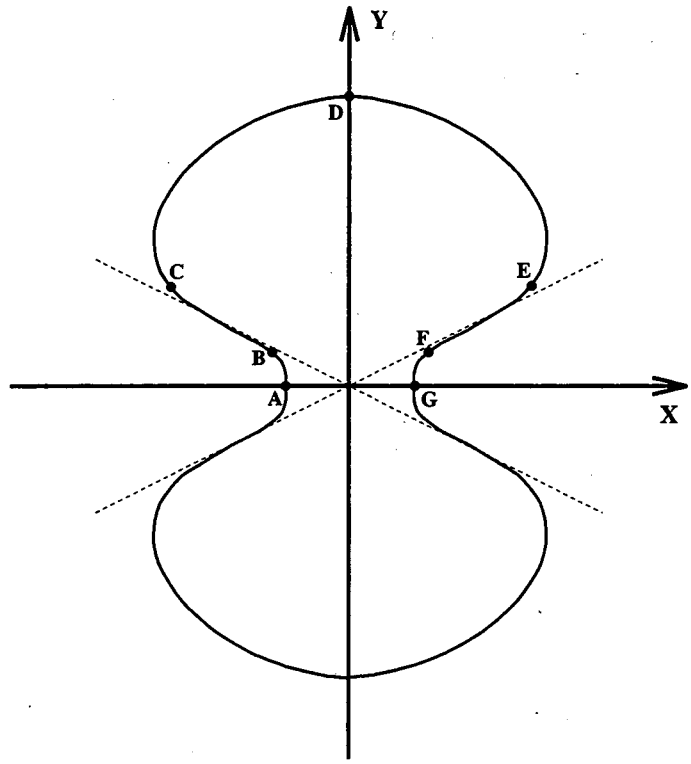

Figure 6.13: The predicted trajectory of the perturbed filament relative to its unperturbed position. The theory is valid only for large b/δ.

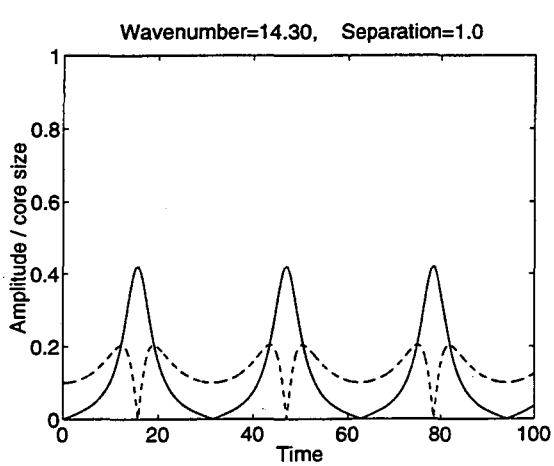

(a) $b = 1.0$

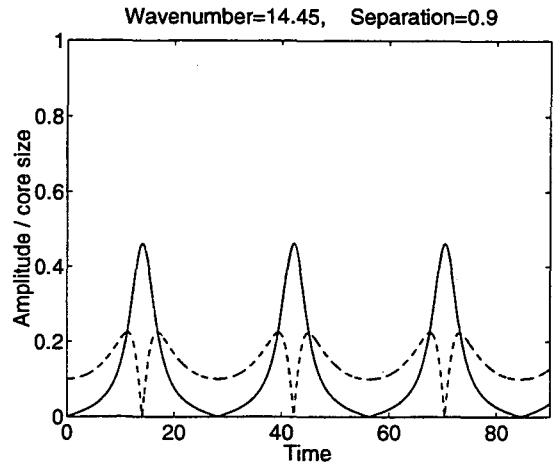

(b) $b = 0.9$

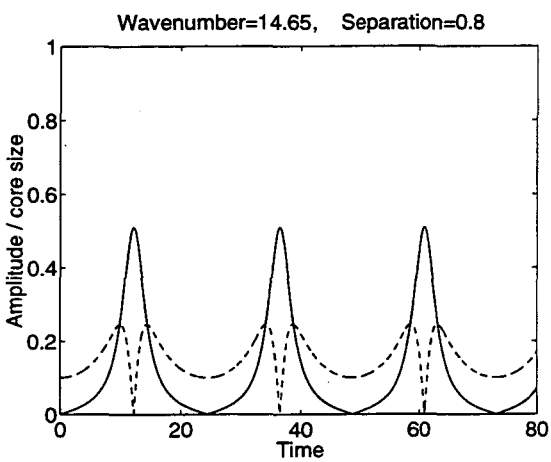

(c) $b = 0.8$

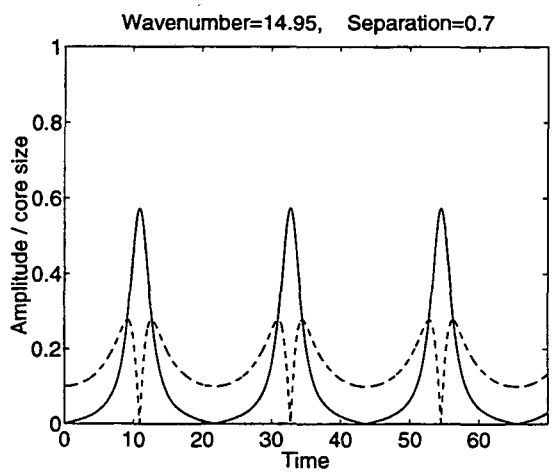

(d) $b = 0.7$

Figure 6.14: Time evolution of the perturbations on a pair of co-rotating vortex filaments with different separations. Dashed line : amplitude in the x-direction (spanwise direction); Solid line : amplitude in the y-direction. The coordinate system is rotating with the vortex pair.

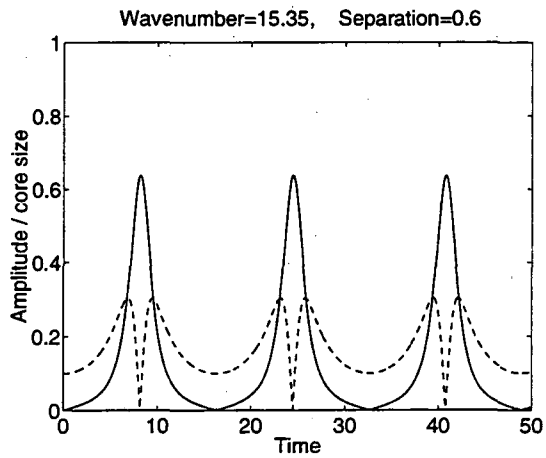

(a) $b = 0.6$

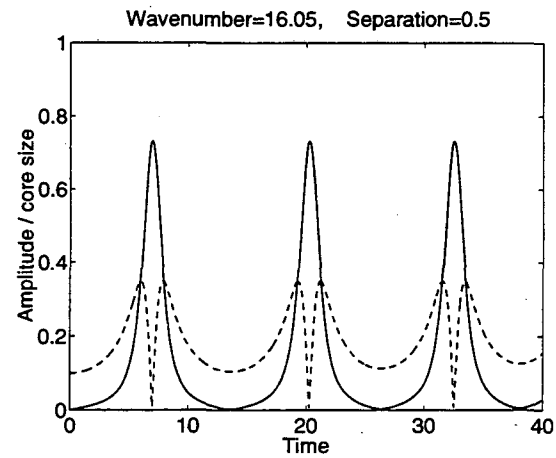

(b) $b = 0.5$

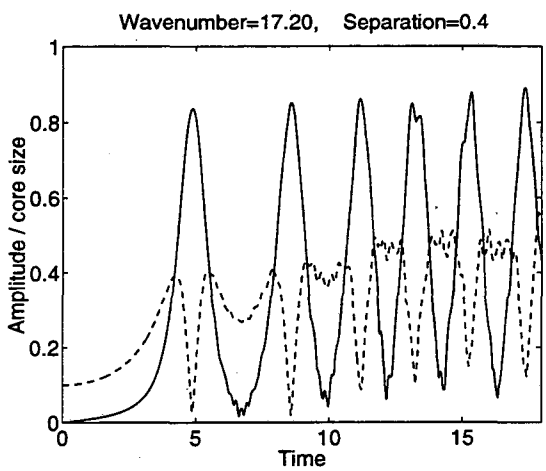

(c) $b = 0.4$

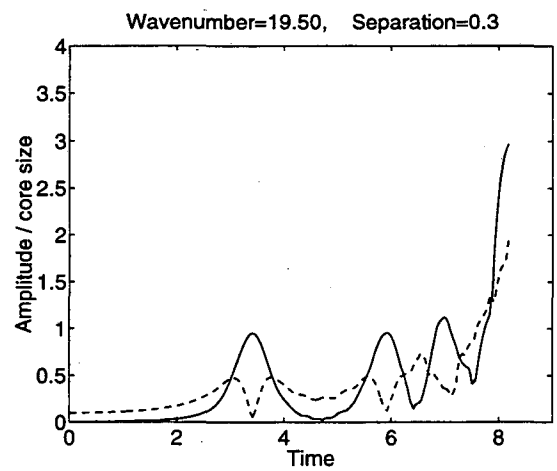

(d) $b = 0.3$

Figure 6.15: Time evolution of the perturbations on a pair of co-rotating vortex filaments with different separations. Dashed line : amplitude in the x-direction (spanwise direction); Solid line : amplitude in the y-direction. The coordinate system is rotating with the vortex pair.

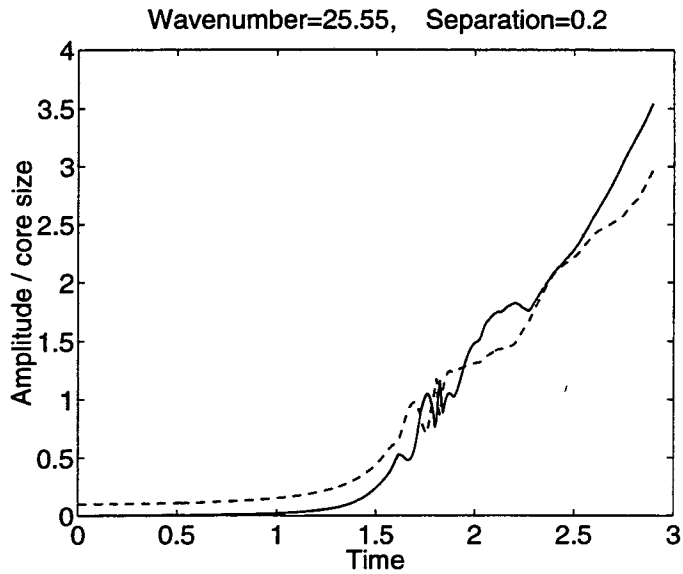

Figure 6.16: Time evolution of the perturbation on a pair of co-rotating vortex filaments. Dashed line : amplitude in the x-direction (spanwise direction); Solid line : amplitude in the y-direction. The coordinate system is rotating with the vortex pair.

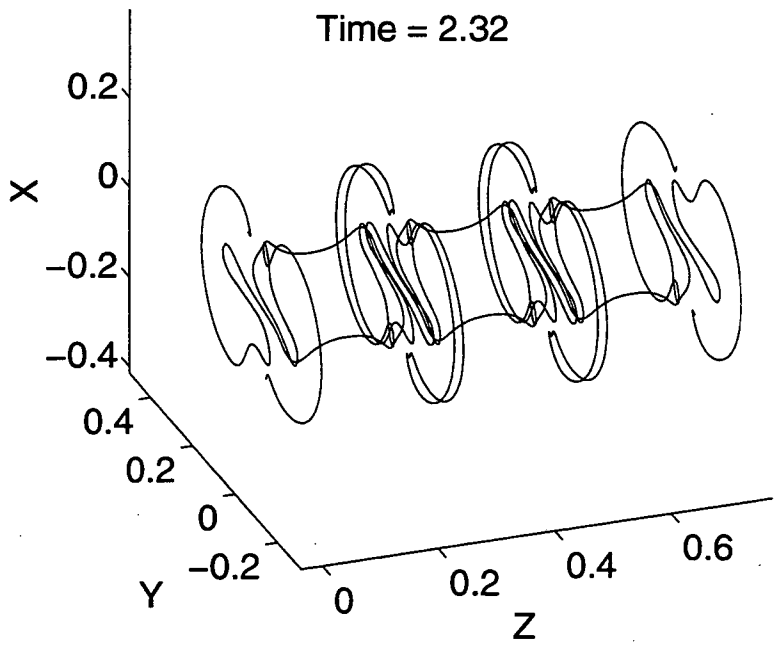

Figure 6.17: Configuration of the vortex pair after the two filaments become tangled together.

6.3 Short wave instability on a vortex filament immersed in a co-rotating vorticity field

We now wish to study the short wave instability on a single vortex filament with fixed core structure immersed in a co-rotating vorticity field. We proceed in the same way as we approached the co-rotating vortex pair in the preceding sections of this chapter.

We shall consider two cases. In case one, a vortex filament is surrounded by a continuous vorticity field whose vorticity is of the same sign as that of the filament. Here the surrounding vorticity field is taken as axisymmetric. The choice of an axisymmetric vorticity field was motivated by two things. First, an axisymmetric vorticity field simplifies the analysis significantly. Second, the two dimensional vorticity equilibrium distribution is locally approximately axisymmetric [31]. In case two, a vortex filament is surrounded by a discrete vorticity field represented by many co-rotating vortex filaments. In both cases, the motion of the filament is the combination of the self-induced rotation and the velocity induced by the surrounding vorticity field. The self-induced rotation frequency is solely determined by the fixed core structure of the vortex filament and is independent of the surrounding vorticity field. Hence the only variable which affects the stability or instability is the property of the velocity field induced by the surrounding vorticity. Near the filament, the velocity field can be well approximated by its linear part.

6.3.1 A vortex filament embedded in a continuous vorticity field

We proceed to consider the first case where a vortex filament is surrounded by a continuous vorticity field. Suppose that the vortex filament under consideration is initially located at $\mathbf{r}_0 = (x_0, 0)$ and the surrounding vorticity field is given by $\omega(r)$ (Figure 6.18). The velocity field induced by the vorticity field $\omega(r)$ is

$$\mathbf{u}(x,y) = \frac{1}{2\pi(x^2+y^2)} f\left(\sqrt{x^2+y^2}\right) \begin{bmatrix} -y \\ x \end{bmatrix}, \tag{6.65}$$

where the function $f(r)$ is defined as

$$f(r) = \int_0^r 2\pi\rho\,\omega(\rho)\,d\rho. \tag{6.66}$$

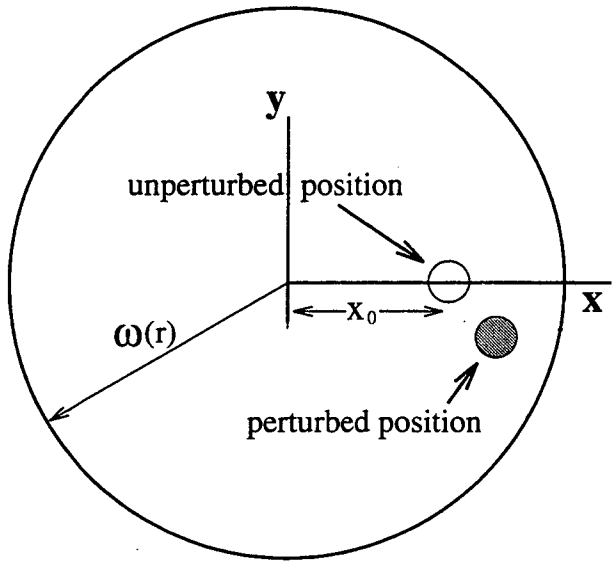

Figure 6.18: A vortex filament surrounded by a continuous vorticity field.

The vortex filament rotates around the origin with an angular velocity $\frac{1}{2\pi x_0^2} f(x_0)$.

In the reference system $(\tilde{x}, \tilde{y})$ which is attached to the unperturbed filament as shown in Figure 6.19, the induced velocity field is

$$\begin{aligned}
\mathbf{u}(\tilde{x},\tilde{y}) &= \frac{1}{2\pi[(x_0+\tilde{x})^2+\tilde{y}^2]} f\left(\sqrt{(x_0+\tilde{x})^2+\tilde{y}^2}\right)\begin{bmatrix} -\tilde{y} \\ x_0+\tilde{x} \end{bmatrix} - \frac{1}{2\pi x_0^2} f(x_0)\begin{bmatrix} -\tilde{y} \\ x_0+\tilde{x} \end{bmatrix} \\
&= -\frac{1}{2\pi x_0^2} f(x_0)\left(2-\frac{f'(x_0)x_0}{f(x_0)}\right)\begin{bmatrix} 0 \\ \tilde{x} \end{bmatrix} + O(\tilde{x}^2+\tilde{y}^2) \\
&\stackrel{\text{def}}{=} -\frac{1}{2\pi x_0^2} c_1 \begin{bmatrix} 0 \\ \tilde{x} \end{bmatrix} + O(\tilde{x}^2+\tilde{y}^2). \qquad (6.67)
\end{aligned}$$

Near the vortex filament (when $\tilde{x}$ and $\tilde{y}$ are small), the induced velocity field is well approximated by the linear term on right-hand side of equation (6.67), which represents a straining flow. In the cylindrical (r, θ) coordinate system, this linearized flow is

$$u_r(LF) = -\frac{1}{2\pi x_0^2}\frac{c_1}{2}(r\sin 2\theta), \qquad (6.68)$$

$$u_\theta(LF) = -\frac{1}{2\pi x_0^2}\frac{c_1}{2}(r + r\cos 2\theta). \qquad (6.69)$$

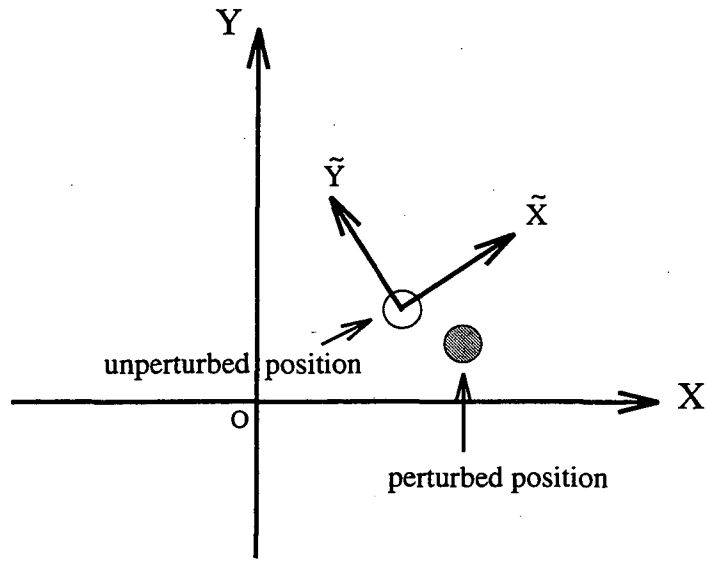

Figure 6.19: The vortex filament and the coordinate system attached to it.

As we have already discussed in the first section of this chapter, when the tangential velocity of the linearized flow is neutralized by the self-induced rotation, the radial component of the linearized flow causes the perturbation wave to grow exponentially in a certain radial direction (Figure 6.20). The maximum of $u_r(LF)$ is $\frac{1}{2\pi x_0^2}c_1 r$. The minimum of $u_r(LF)$ is zero. Instability occurs when the self-induced rotation is between the minimum and maximum of tangential velocity of the linearized flow, i.e. when

$$0 < u_\theta(SR) < \frac{1}{2\pi x_0^2}c_1 r \tag{6.70}$$

Substituting $u_\theta(SR) = -\frac{\Gamma}{2\pi\delta^2}\tilde{\Omega}(\tilde{k})r$, we find that the instability condition is

$$-\frac{\delta^2 c_1}{x_0^2\Gamma} < \tilde{\Omega}(\tilde{k}) < 0 \tag{6.71}$$

where δ is the core size and Γ is the circulation of the vortex filament in consideration. From the dispersion relations shown in Figure 6.6 and Figure 6.7, it is clear that one can always find wavenumbers which satisfy the instability condition (6.71) since the range of normalized rotation frequency in the dispersion relations always contains the interval $[-1, 0]$. Therefore unstable modes always exist on a vortex filament surrounded by a continuous vorticity field.

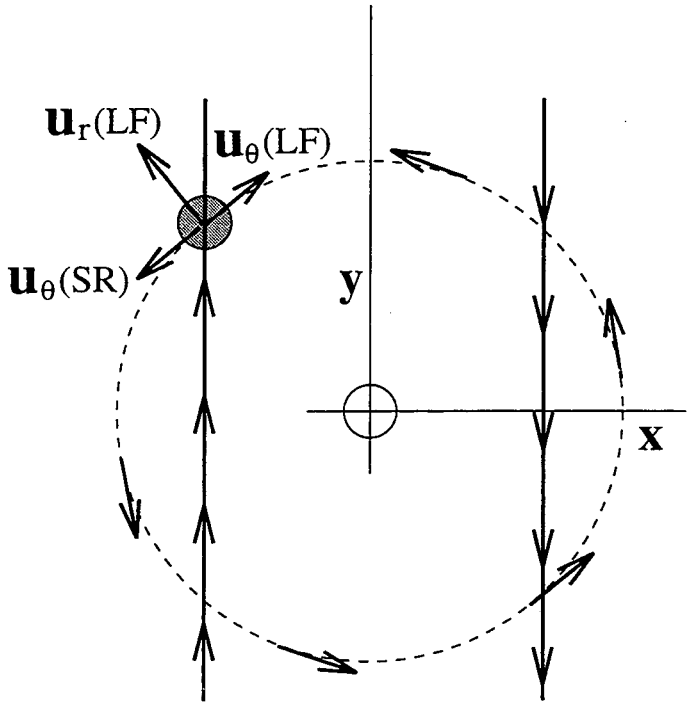

Figure 6.20: A sketch of the motion of a filament surrounded by a continuous vorticity field.

6.3.2 A vortex filament immersed in a discrete vorticity field

In this subsection we discuss the second situation in which a vortex filament is surrounded by a discrete vorticity field. Here we consider a special case where the vorticity field to be discretized is a uniform vorticity distribution in a unit circle, that is,

$$\omega(r) = \begin{cases} 1, & r \leq R \\ 0, & r > R \end{cases} \quad \text{where } R = 1. \tag{6.72}$$

The vorticity field is discretized as follows: first, N_{layer} locations equally spaced in the radial direction are placed within the circle. A numerical filament is placed at the center of the circle. The radial location at $r = n\,\triangle r$ ($n = 1, ..., N_{layer}$) has $6n$ numerical filaments equally spaced at $\theta = j\,\triangle\theta_n$ ($j = 1, ..., 6n$). Here $\triangle r = R/(N_{layer} + 0.5)$ and $\triangle\theta_n = 2\pi/(6n)$. The layouts of the numerical filaments on a cross-section are illustrated in Figure 6.21 for $N_{layer} = 1$, 2, 3, 4, 6 and 8. In Figure 6.21 each solid circle represents a numerical filament. The center line of the corresponding filament passes through the center of the solid circle. However, the solid circle is for illustration only. It does not describe the real size of the cross-section of the filament. In fact, the overlapping condition requires that

the core radius of the filament be large in comparison with the distance between neighboring filaments. In the discretization, we use the numerical core radius

$$\delta = R/\sqrt{N_{layer}}, \tag{6.73}$$

which, as N_{layer} increases, goes to zero, but at a slower pace than the inter-filament distance $\triangle r = R/(N_{layer} + 0.5)$. Anderson and Greengard [4], and Almgren, Buttke and Colella [2] used a similar numerical core radius in their simulations of the vortex ring merger problem.

For this discrete vorticity field, we consider the short wave instability of a vortex filament at the outermost radial layer. As before, we first attach a coordinate system to the unperturbed filament. The crucial step in this stability analysis is to calculate the velocity field around the unperturbed position of the filament, which is caused by the presence of other vortex filaments. Since the surrounding vorticity field is a discrete one represented by a set of numerical filaments, an exact expression for the induced velocity field is difficult, if not impossible, to derive. In this case, the numerical approach is certainly more desirable. In Figure 6.22 and Figure 6.23, we show the velocity field and streamlines for various values of the parameter N_{layer}. In the plots each arrow represents the velocity vector at that location and the thin solid lines are streamlines. Figure 6.22 and Figure 6.23 indicate that the streamlines are a family of ellipses. This phenomenon is qualitatively the same as in the case of a co-rotating vortex pair which we have studied in previous sections (see equation (6.3)). However, as N_{layer} (the number of radial layers in the discretization) increases, so does the ratio of the major axis to the minor axis of the ellipses. In the limit of $N_{layer} \to \infty$, the streamlines become a family of parallel straight lines and the velocity field tends to a straining flow. The convergence to a straining flow of the velocity field is best seen in Figure 6.23 where $N_{layer} = 16$. Recall that the straining flow is exactly what we observed when the surrounding vorticity field is continuous (see equation (6.67)). It is clear that the two extreme cases are (a) a co-rotating vortex pair where the vortex filament in consideration is companied by just one filament, and (b) the case where the vortex filament is surrounded by a continuous vorticity field. No matter whether the surrounding vorticity field is continuous or discrete, the flow near the filament, if observed relative to the filament, is rotating clockwise (see Figure 6.4, Figure 6.22 and Figure 6.23). This rotation is in a direction opposite to the core rotation of the filament. For short wave modes on a filament with fixed core structure, the self-induced rotation is in the same sense as the core rotation of the filament. So the rotation part of the velocity field near the filament acts against

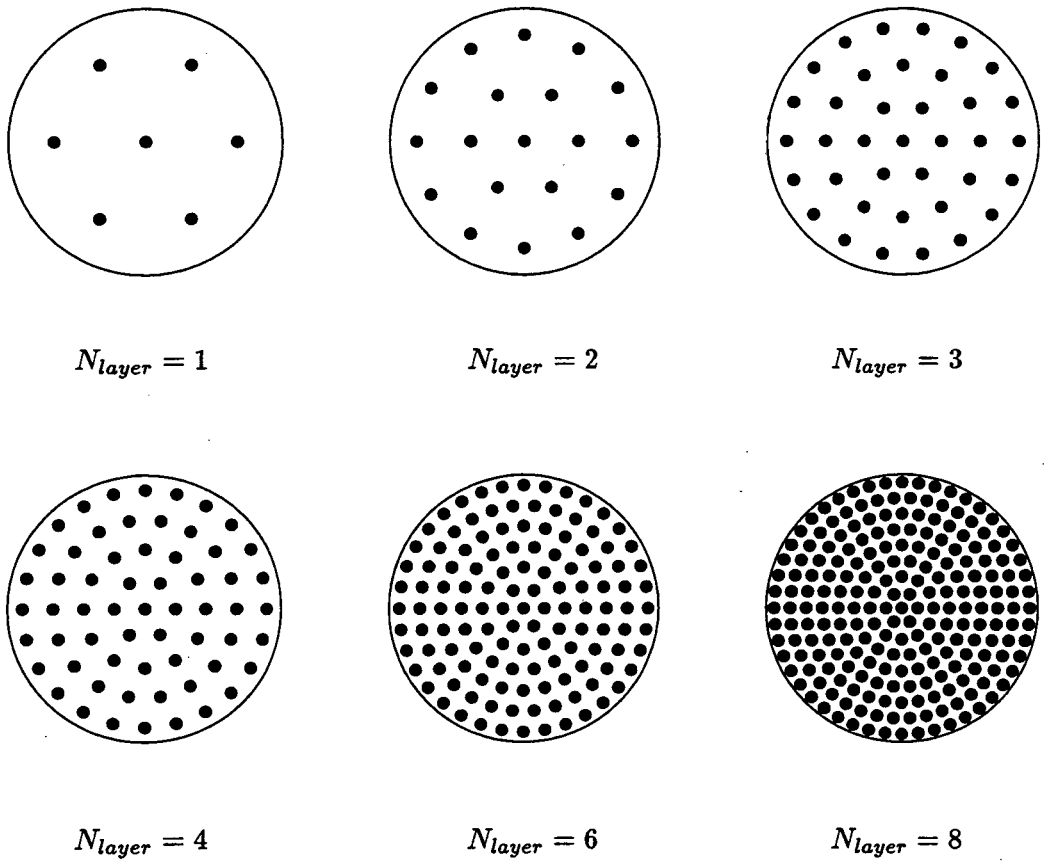

Figure 6.21: Layouts of numerical filaments. Here the solid circles are for illustration only. They do not describe the real size of the cross-section of numerical filaments. In fact, the overlapping condition requires that the core radius of the numerical filaments be larger than the inter-filament distance.

the self-induced rotation. Because of the fact that the minimum tangential velocity of a straining flow is zero and the fact that the range of normalized frequency of the self-induced rotation contains the interval $[-1, 0]$, there are always short wave modes whose self-induced rotation can balance the tangential component of the flow near the filament. When these two rotations cancel each other out, the short wave perturbation mode stops rotating and diverges along the radial direction, driven by the radial component of the flow. Thus the short wave instability always occurs on a vortex filament immersed in a co-rotating vorticity field.

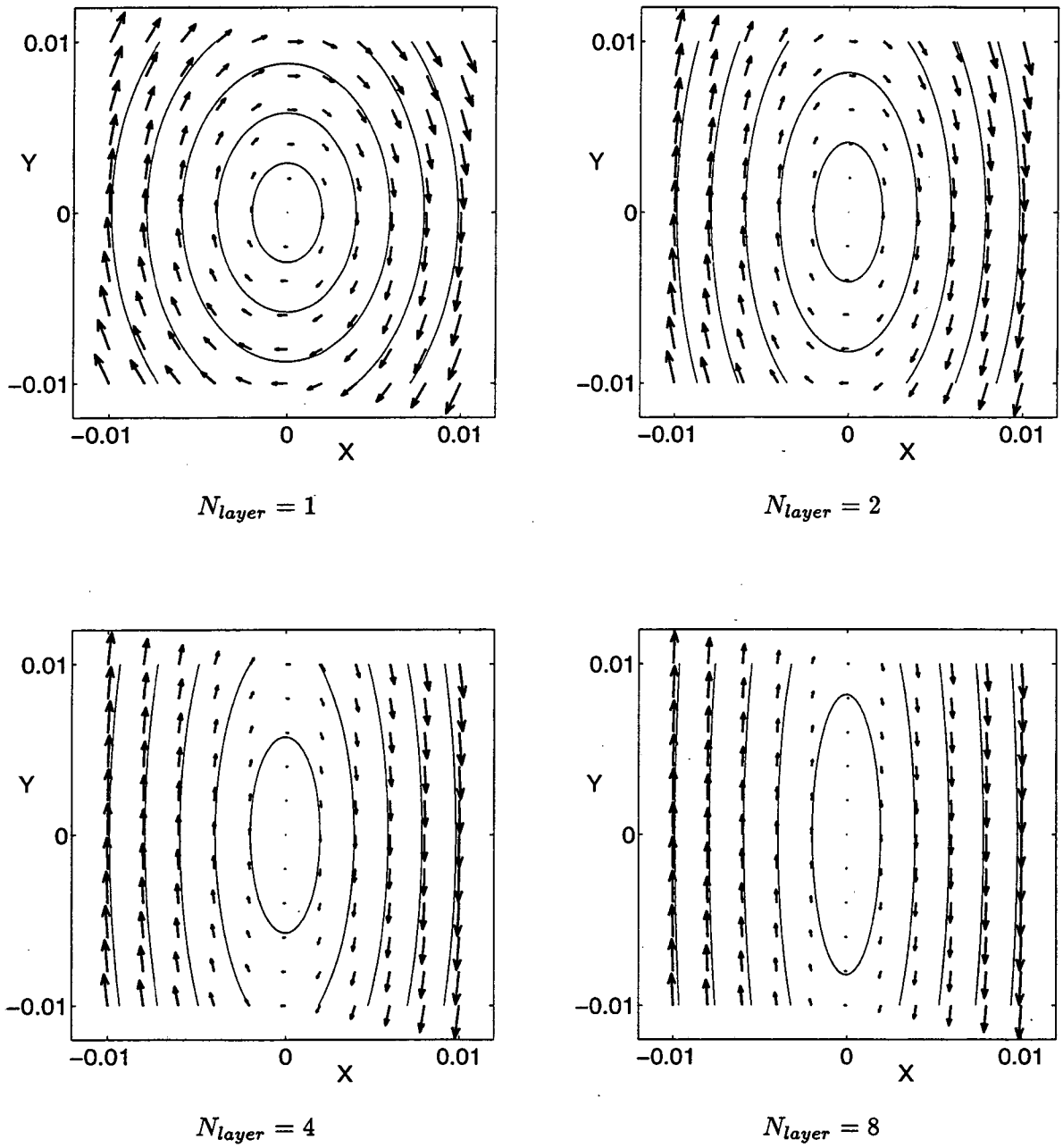

Figure 6.22: Velocity field and streamlines near the filament.

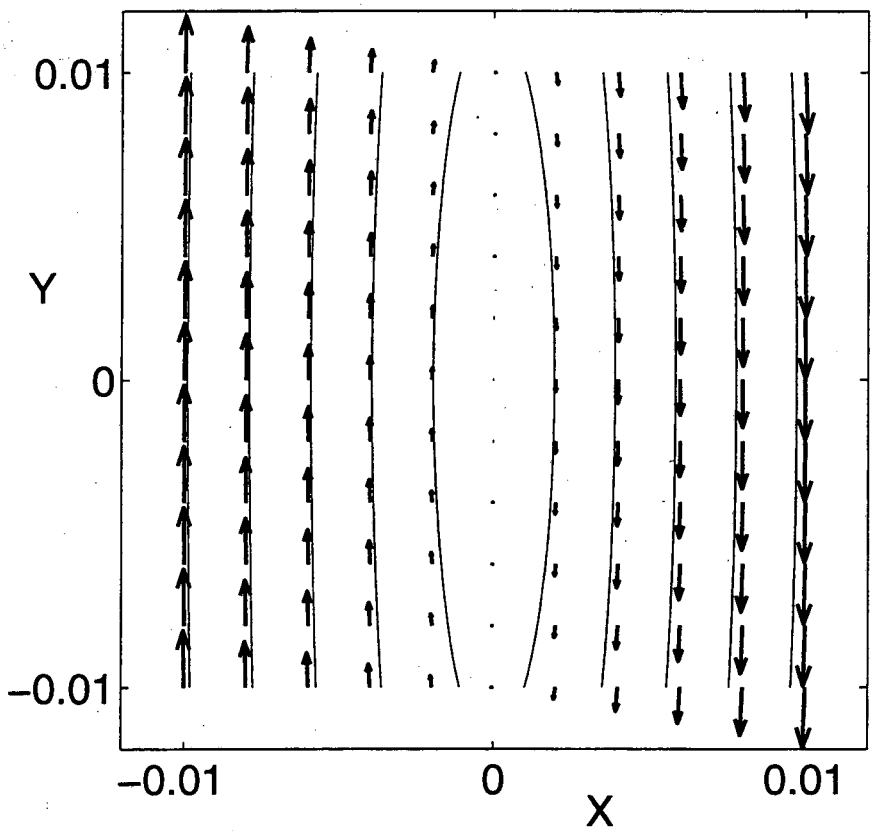

$N_{layer} = 16$

Figure 6.23: Velocity field and streamlines near the filament.

6.4 Short wave instability and the proliferation of vortex hairpins in three dimensional vortex methods

In the remainder of this chapter we study the wild stretching of the numerical vortex filaments and the subsequent formation of small-scale hairpin structures typically observed in numerical simulations using the vortex method. We will relate this phenomenon to the short wave instability on a vortex filament surrounded by one or more co-rotating vortex filaments which we have studied theoretically and numerically in the previous sections.

The complexity of small-scale vortex structure in three dimensional vortex methods has been observed by many authors [26], [28], [75]. In numerical calculations using the vortex method, after some time the numerical vortex filaments start stretching and folding, first gradually, and then violently. The total number of vortex segments increases exponentially (or even faster than that), so it very quickly exceeds the capacity of our computing facilities and forces us to stop the simulation [28]. The stretching and folding occur even if the initial configurations of the numerical filaments are parallel rings or parallel straight lines, for which the stretching and folding are not supposed to appear in exact arithmetics. It has been pointed out [32] that the spatial chaos (stretching and folding) is generated by the evolution of some unstable modes. However in [32] the cause and the mechanism of the instability were not explained. In the following we apply the vortex method to a vortex ring and try to analyze the small-scale structures of the flow produced by the vortex method. We first show that the stretching and folding of the numerical filaments are indeed caused by the exponential growth of unstable modes. Then we go on to show that the instability of these modes is due neither to the numerical instability of the ODE solver we use nor to the spatial discretization resolution. These unstable modes, initially generated by the numerical round-off errors, grow exponentially, driven by the combination of the self-induced rotation velocity and the velocity induced by the surrounding co-rotating vorticity field. Whether the surrounding vorticity field is discrete or continuous does not affect the instability.

At time $t = 0$, the vorticity field to be discretized is represented by a vortex ring with uniform vorticity distribution inside the core. The radius of the ring is $R = 1.0$ and the core radius is $r = 0.15$. The physical vortex ring is replaced by a set of $N_{filament}$ numerical ring-shaped filaments with numerical cut-off core size δ. The layouts of the numerical filaments on a cross-section of the vortex ring are shown in Figure 6.21 for various numbers of filament layers in the radial direction. The circulation carried by each numerical filament

is equal to $\Gamma/N_{filament}$, where Γ is the circulation of the vortex ring and for simplicity we take $\Gamma = 1$. The numerical filaments are then cut into segments in the azimuthal direction around the central axis of the ring. To satisfy the overlapping condition [3], [8], [9], [41], we require that the maximum length h of these segments be smaller than the numerical cut-off core size δ. In the calculation we use the second order cut-off function $f(r) = 1 - e^{-r^3}$ and the classic fourth order Runge-Kutta method to do numerical integration in the time dimension. To maintain a uniform resolution, if the length of a segment becomes larger than $2\,h$ during the calculation, we cut it into two segments of equal length. It is important to note that the i-th node in the azimuthal direction on a numerical filament is theoretically equivalent to the j-th node on that same filament under a rotation transformation. Hence, when exact arithmetics is used (i.e. there is no round-off error), the numerical filaments should remain as rings. Thus if stretching and folding occurs in the numerical calculation, it must be due to the accumulation and the magnification of the round-off errors associated with finite precision arithmetics.

We start with the discretization which has one layer of numerical filaments in the radial direction as shown in Figure 6.21 with $N_{layer} = 1$. The total number of numerical filaments is $N_{filament} = 7$ and initially there are 168 segments on each filament. The numerical core size is taken as $\delta = 0.15$. The maximum length of the segments is approximately $h = \delta/4$. The numerical calculations are carried out using both single precision and double precision. The stopping criterion is the following: when the number of segments on any filament is ten times larger than the original number of segments per filament, the computation is terminated.

Figure 6.24 gives a perspective view of the numerical filaments near the stopping time. This calculation was done with single precision and with a time step of $dt = 0.04$. Figure 6.24 displays the typical configuration of the numerical filaments after the number of segments has increased drastically. The filaments stretch and fold and the thin hairpin structures wrap around the filaments. The configuration of the numerical filaments seen here is very similar to that of a co-rotating vortex pair at the late stage of instability shown in Figure 6.17. The difference is that we now have seven numerical filaments tangled together instead of just two. In Figure 6.25 we exhibit two two-dimensional views of the numerical filaments in the single precision calculation. At time $t = 20.0$, the unstable modes have small amplitudes and are still invisible in the plot. Computations were also carried out using double precision. Figure 6.26 shows two-dimensional views of the numerical

filaments at time $t = 40.0$ and $t = 64.0$. Comparing Figure 6.25 and Figure 6.26, we find that the unstable modes grow at least exponentially. If the growth were less than exponential, we would be able to run the calculation for much longer time before we hit the stopping criterion in the double precision calculation where the round-off error is of the order $10^{-15} \sim 10^{-16}$. Note that the round-off error in double precision calculation is much smaller than the round-off error in single precision calculation which is of the order of 10^{-7}.

We raise three questions: (1). Is the exponential growth of the unstable modes due to the instability of the ODE solver we use ? (2). Is the exponential growth of the unstable modes due to the coarse discretization in the spatial dimensions since there are only seven numerical filaments representing a deformable core ? or (3). Is the exponential growth of the unstable modes caused by the short-wave instability on a vortex filament which is surrounded by a co-rotating vorticity field (continuous or discrete) ? The answer to the first two questions is no and the answer to the third one is yes. We will examine these questions one by one.

Recall that the ODE solver we use is the classical fourth order Runge-Kutta method. As we pointed out in Chapter 6 (see Figure 5.8 and the discussion associated with it), this ODE solver is stable for small time steps, and when it is unstable for large time steps, its instability gets weaker as the time step is decreased. To answer the first question, we run the single precision calculations of seven numerical filaments using various time steps $dt = 0.1$, 0.04, 0.01 and 0.004. The two-dimensional views of the numerical filaments obtained in these calculations are presented in Figure 6.27. Not surprisingly, the four plots in Figure 6.27 obtained with different time steps exhibit very similar structures. This simply implys that the growth rate of the unstable modes is not affected by the time step as long as the time step is not too large. Actually, if we select the time step according to the criterion we established in Chapter 6, then $dt = 0.1$ is a reasonable time step. Relatively speaking, $dt = 0.004$ is a fairly small time step. The fourth order accuracy of the ODE solver generally means that the error behaves like $O((dt)^4)$ as dt goes to zero. Thus for the numerical solution obtained with $dt = 0.004$, one can say that the error associated with the discretization in the time direction is negligible. Hence the exponential growth of the unstable modes is not caused by the discretization in the time direction.

To answer the second question, we repeat the single precision calculations with more numerical vortex filaments. With two layers of filaments in the radial direction $N_{layer} = 2$, the total number of the numerical filaments is $N_{filament} = 19$ (see Figure

6.21 for the distribution of the numerical filaments on the cross-section of the ring). For $N_{layer} = 2$, we chose the numerical core size $\delta = 0.12$. At time $t = 0$, there are 209 segments on each filament. The maximum length of the segments satisfies approximately $h = \delta/4$. The top plot of Figure 6.28 shows the two-dimensional view of the numerical filaments at the stopping time, obtained using 19 numerical filaments. The bottom plot of Figure 6.28 represents a portion of the top plot, giving the detailed structures of the top plot. In the calculations leading to Figure 6.29, we use even more numerical filaments. The number of radial layers N_{layer} is 3. The total number of the numerical filaments goes up to 37. At time $t = 0$, each filament is represented by 235 segments. The total number of vortex segments in the initial discretization already amounts to 8695 ! Again, the top plot of Figure 6.29 is a two-dimensional view of the numerical filaments at the stopping time and the bottom plot is a portion of the top plot shown in detail. Figure 6.29, together with Figure 6.28, indicates that the exponential growth of the unstable modes is not eliminated or reduced by using a better spatial discretization. The stopping time is actually getting smaller as we use more numerical filaments. The stopping criterion is that we terminate the calculation whenever the number of segments on any filament grows by 10 times. The unstable modes originate from the round-off errors. At least this is true for vortex rings where the symmetry of the initial configuration excludes the possibility of stretching and folding if exact arithmetics is used. The round-off errors at each numerical point are affected by thousands if not millions of operations. Thus it is virtually impossible to know the exact values of these round-off errors or to know the relation between the round-off errors at two numerical points. People often treat the round-off errors as being produced randomly. If we believe that there is randomness associated with the starting times and starting amplitudes of the unstable modes, it is reasonable to expect that the stopping criterion can be reached earlier for more filaments since only one of those filaments needs to grow by 10 times. This may account for the smaller stopping time in the case of more numerical filaments.

Now we move on to the third question. The short-wave instability discussed in the previous sections provides a plausible explanation for the exponential growth of the unstable modes. This short-wave instability occurs on a vortex filament surrounded by a co-rotating vorticity field. If the surrounding vorticity field is discrete, the coarsest discretization is just one point. In that case, we have a co-rotating vortex pair. In sections 1 and 2 of this chapter, it was predicted theoretically and confirmed numerically that there are always unstable short-wave modes for a co-rotating vortex pair. In section 3, we showed that this is also true

for other discrete vorticity distributions and continuous vorticity distributions. The general process of stretching and folding is the following. At the early stage of the calculation, the round-off errors generate unstable seeds, i.e., unstable modes with starting amplitudes comparable to the magnitude of the round-off errors. Then the short-wave instability starts to manifest itself and the amplitudes of unstable modes increase exponentially. Although the round-off errors continue to contribute to the unstable modes as the calculation goes on, this contribution becomes less and less significant compared to the exponential growth of the unstable modes. At the late stage of the calculation, the hairpin structures appear and get longer and longer.

Supporting evidence for the above argument comes from the similarity between the filament configuration of a co-rotating vortex pair shown in Figure 6.30 and the filament configuration of a vortex ring in Figure 6.31, Figure 6.32 and Figure 6.33. For a co-rotating vortex pair, two perspective views of one filament at the late stage of instability are given in Figure 6.30. As for a vortex ring, Figure 6.31 exhibits two perspective views of one numerical filament at the stopping time, where the vortex ring is represented by 7 numerical filaments. Figure 6.32 and Figure 6.33 display the configurations of one numerical filament obtained in calculations using respectively 19 numerical filaments and 37 numerical filaments. It is clear from these graphs that they all share the similar structure of long and thin hairpins wrapping around, which suggests that vortex stretching and folding in the vortex method is due to the short-wave instability.

The regular pattern as seen in Figure 6.30 for the co-rotating vortex pair and the irregularity associated with the numerical filament configuration for the vortex ring (Figure 6.31, Figure 6.32, and Figure 6.33) are due to the difference in the initial amplitudes of unstable modes. For the vortex pair, the initial perturbation is an unstable mode with a moderately small amplitude (10^{-2}). Since the round-off error of double precision calculation is of the order of $10^{-15} \sim 10^{-16}$, the finite initial amplitude of the perturbation mode makes it dominate over other unstable modes. So there is only one mode visible in Figure 6.30. In contrast to the vortex pair, for the vortex ring, the initial perturbation is zero. The unstable modes grow from the noise generated by the round-off errors. Due to the randomness of the noise and the fact that the unstable spectrum is a continuous region instead of a discrete set, the filament configuration consists of many unstable modes. Also, as the unstable modes grow, the evolution of these unstable modes is no longer simply the linear superposition of each mode's isolated evolution. Thus the irregularity of the filament configurations shown

in Figure 6.31, Figure 6.32, and Figure 6.33 is fully expected.

Finally, we conclude this section with a summary. In this section we studied the occurrence of hairpin structures in three dimensional vortex methods and its relation to the short-wave instability. We have reached the following conclusions:

- The wild stretching and folding of the numerical vortex filaments is primarily caused by the short-wave instability which occurs on a vortex filament surrounded by a co-rotating vorticity field.
- The wild stretching and folding occurs even if the initial configuration of the numerical vortex filaments is perfectly symmetric (such as vortex rings, straight lines, etc.) where it should not appear if we were using exact arithmetics. It is the round-off errors that provide the starting amplitude for the unstable modes.
- The wild stretching and folding is not caused by the ODE solver we use. It cannot be suppressed or reduced by using a smaller time step.
- Due to the universal presence of the round-off errors, it is very difficult to prevent the unstable modes from starting. The exponential growth of the unstable modes cannot be suppressed or reduced by the refinement in spatial dimensions because the underlying short-wave instability is independent of the spatial discretization.
- Currently Chorin's hairpin removal method [26], [28] is the only method which regulates the numerical filaments and enables us to continue the calculation after the appearance of hairpin structures.

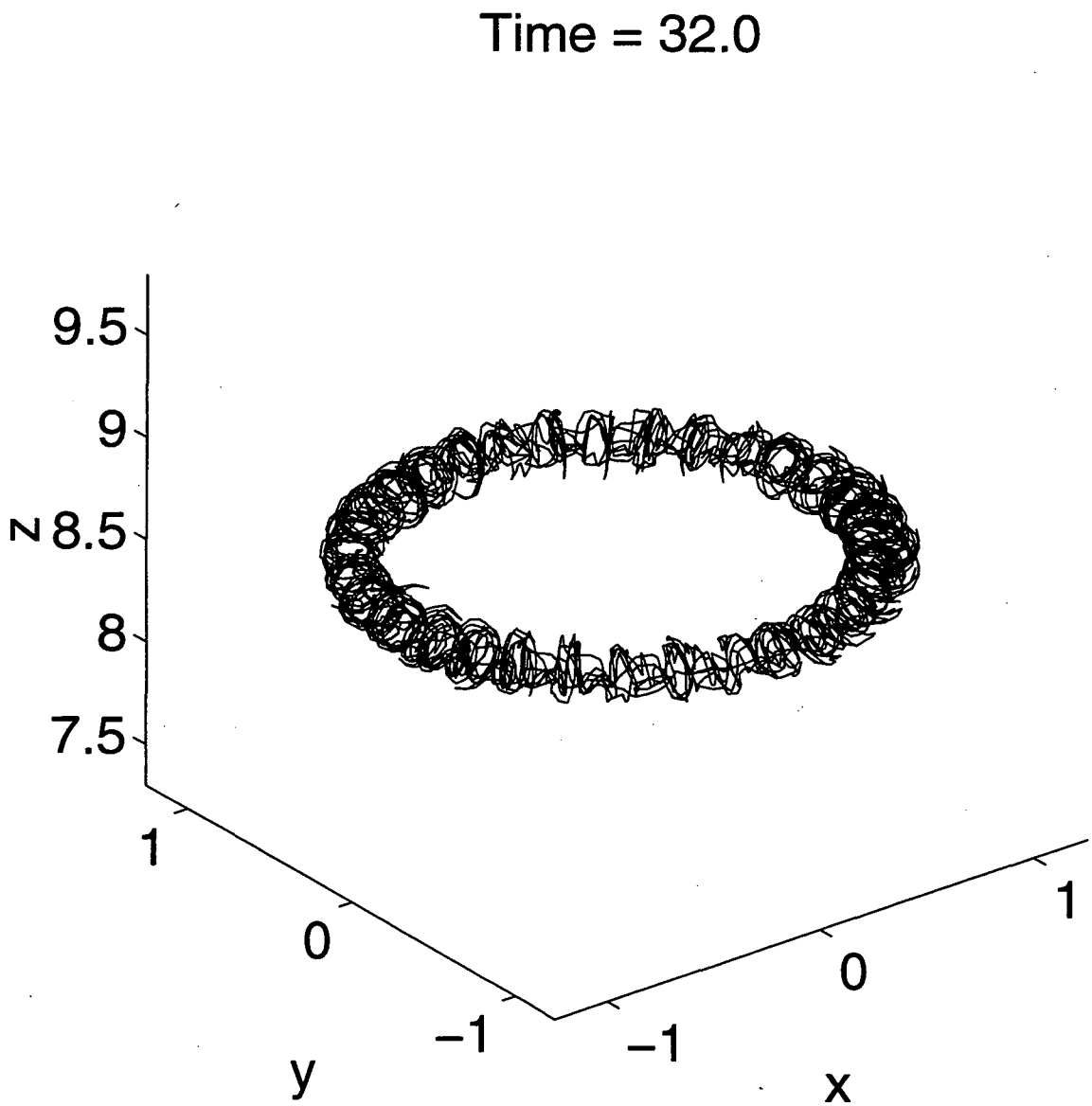

Figure 6.24: Configuration of the numerical filaments obtained with single precision and $dt = 0.04$.

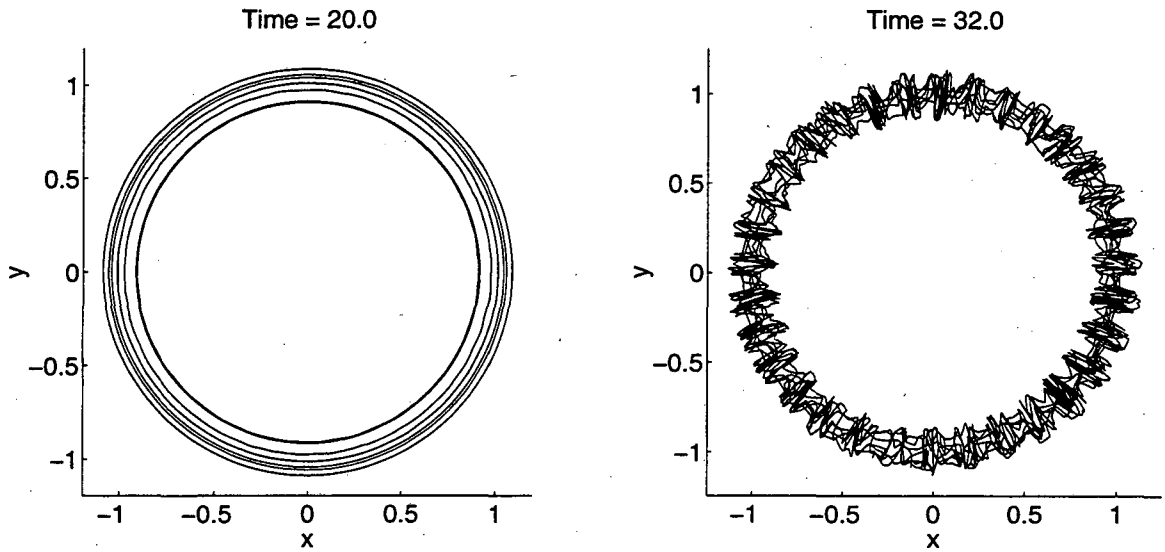

Figure 6.25: Two-dimensional views of the numerical filaments obtained in the single precision calculation.

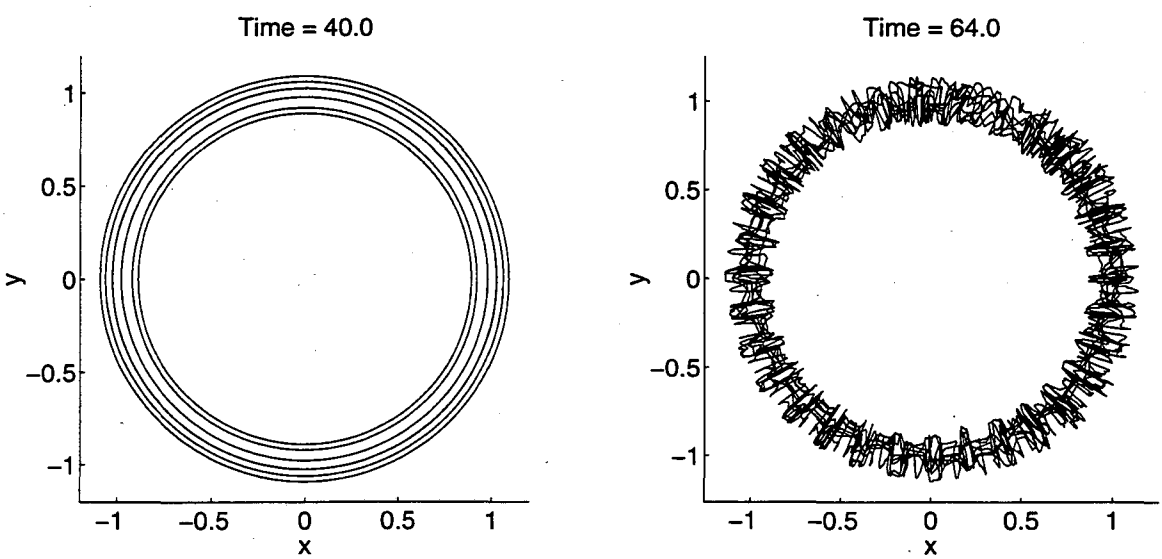

Figure 6.26: Two-dimensional views of the numerical filaments obtained in the double precision calculation.

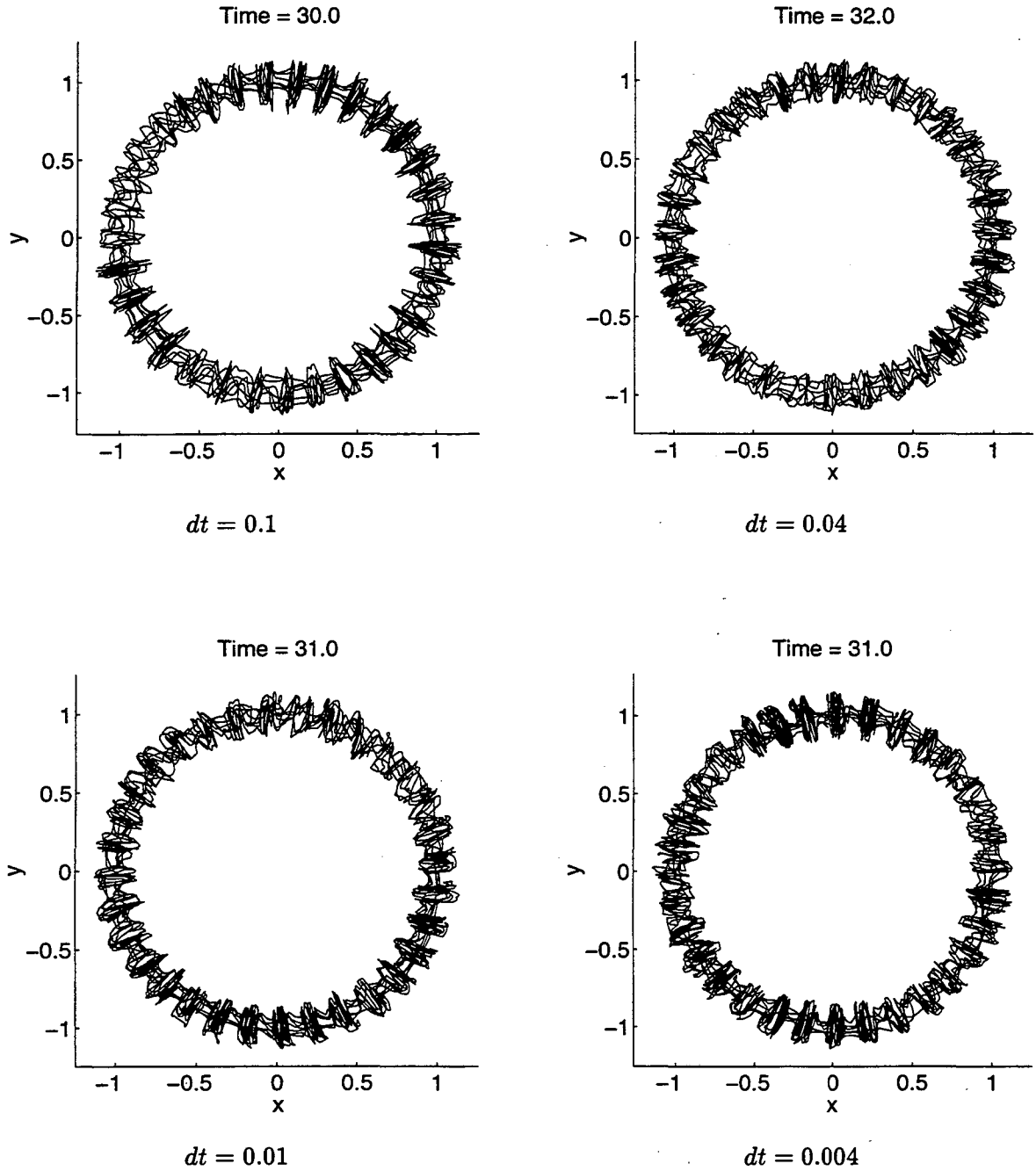

$dt = 0.1$ $dt = 0.04$

$dt = 0.01$ $dt = 0.004$

Figure 6.27: Numerical results obtained in single precision calculations using different time steps.

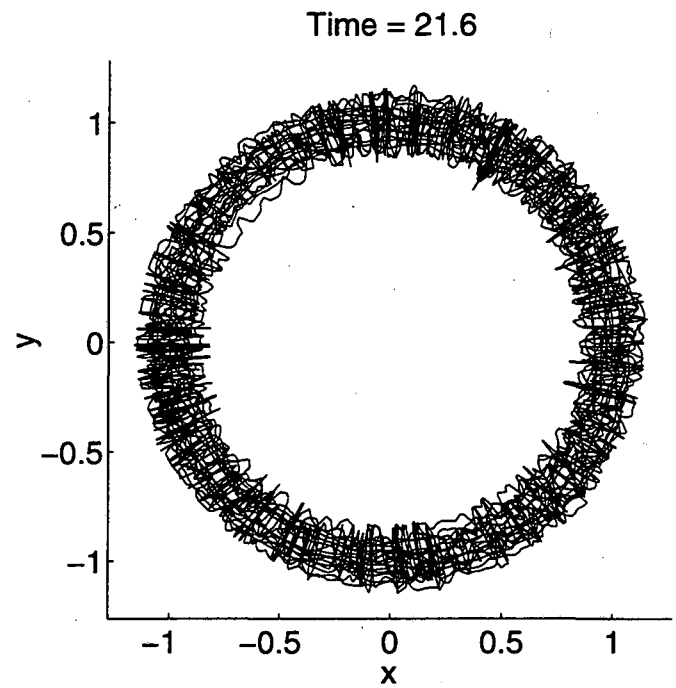

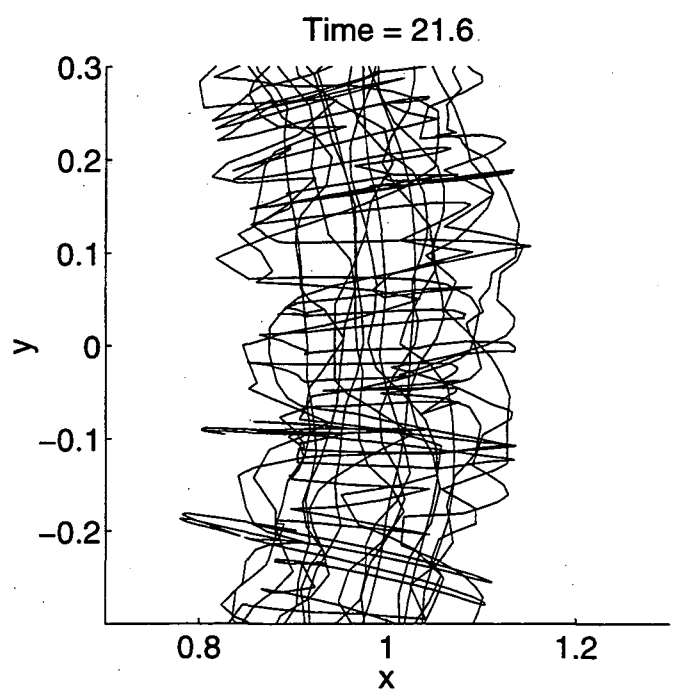

Figure 6.28: Numerical results obtained in the single precision calculation where $N_{layer} = 2$, $N_{filament} = 19$, $\delta = 0.12$ and $dt = 0.04$.

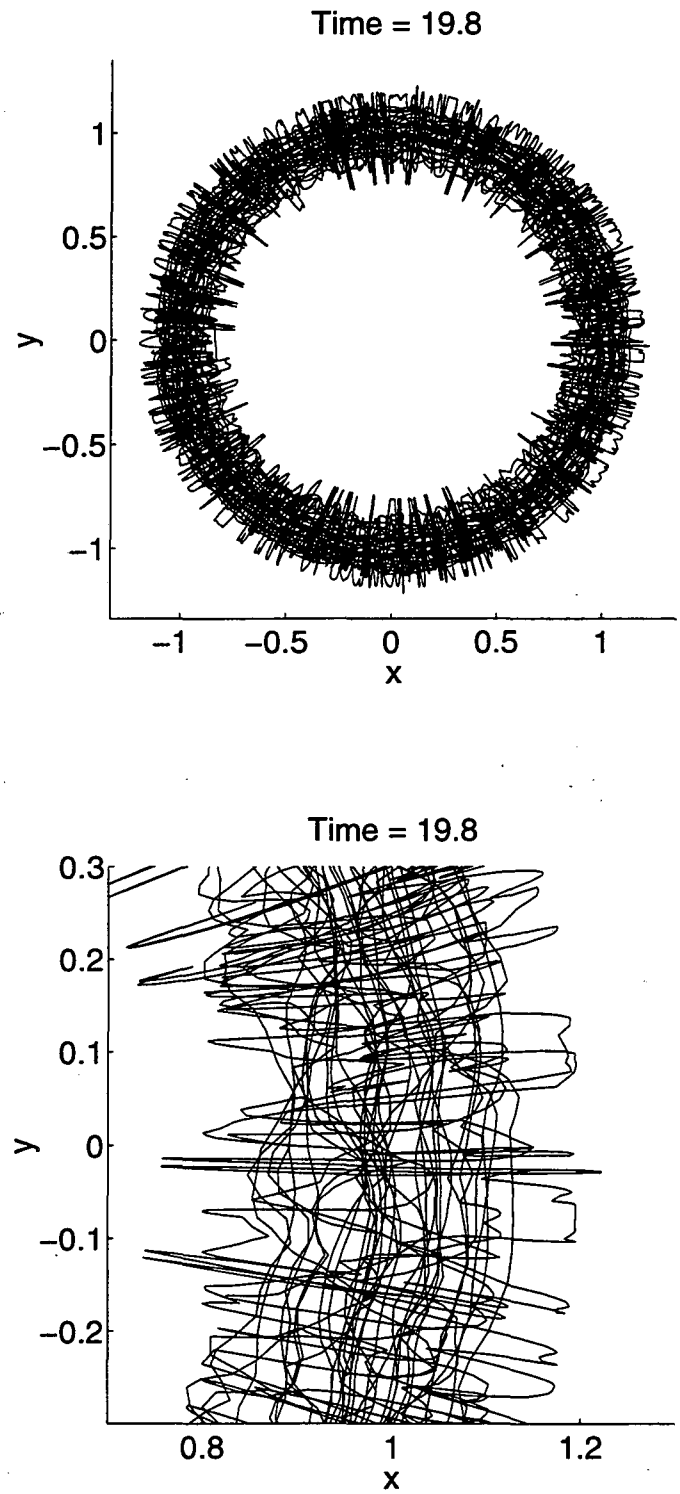

Figure 6.29: Numerical results obtained in the single precision calculation where $N_{layer} = 3$, $N_{filament} = 37$, $\delta = 0.10$ and $dt = 0.04$.

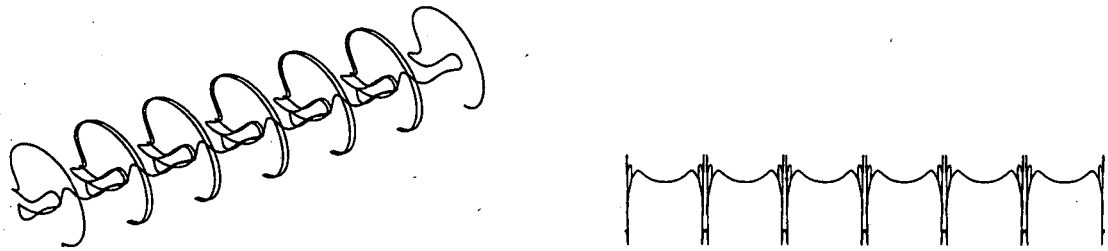

Figure 6.30: Two perspective views of one filament in a co-rotating vortex pair.

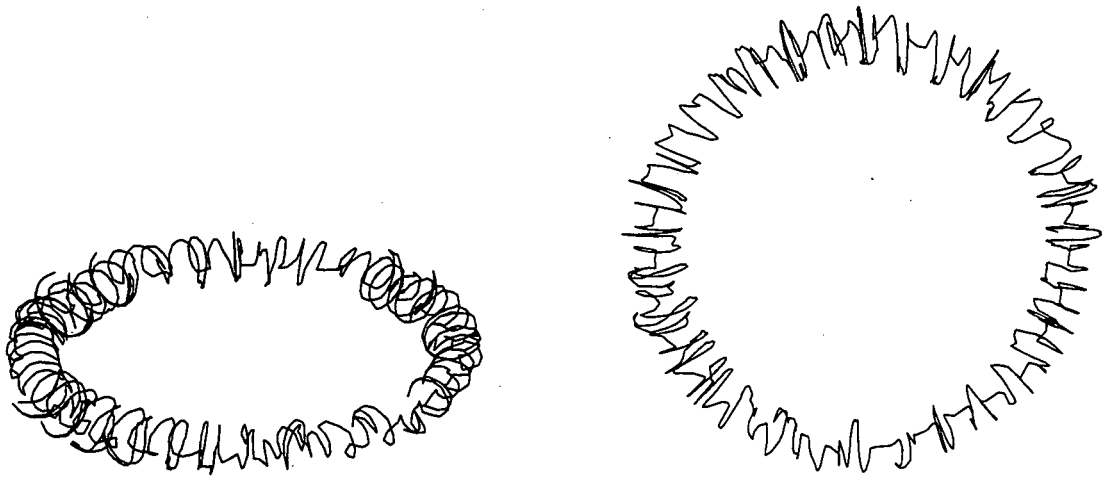

Figure 6.31: Two perspective views of one filament in 7 numerical filaments which are used to represent the vortex ring.

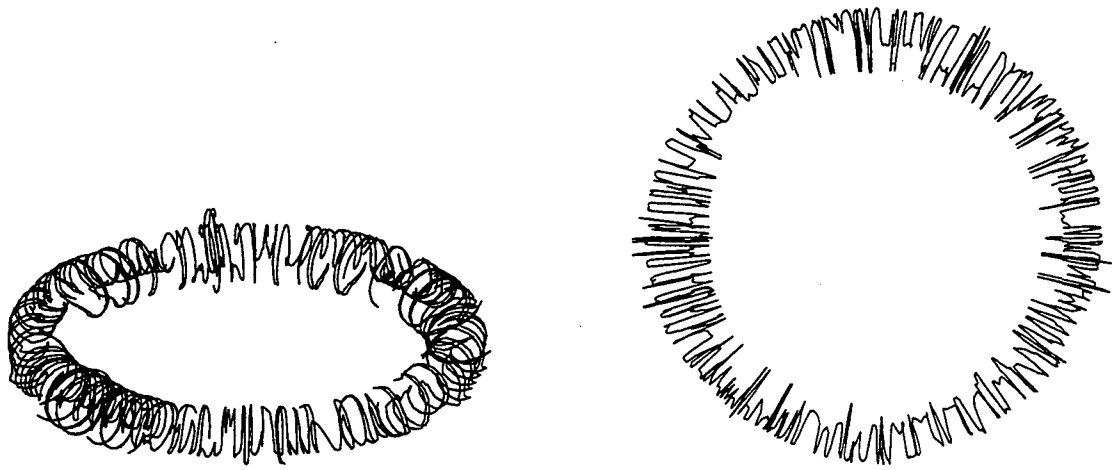

Figure 6.32: Two perspective views of one filament in 19 numerical filaments which are used to represent the vortex ring.

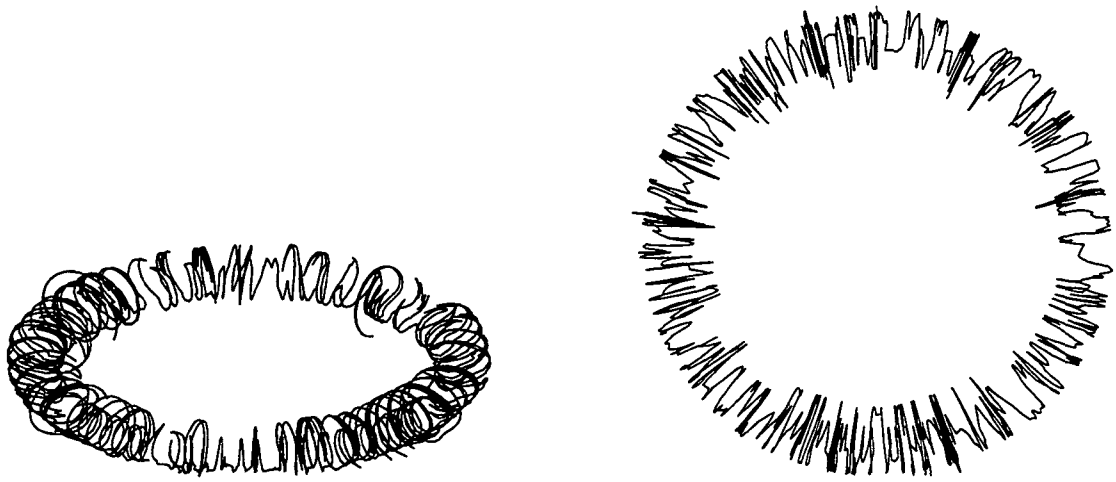

Figure 6.33: Two perspective views of one filament in 37 numerical filaments which are used to represent the vortex ring.

Chapter 7

Conclusions

In this dissertation we have studied vortex methods and short wave instability on vortex filaments both analytically and numerically.

With the thin tube vortex filament method we carried out simulations of the instability of vortex rings. We found that the results previously obtained by Knio and Ghoniem contain an artifact of the numerics; a sufficient refinement of the mesh generates different results. In particular, the neutrally stable (i.e. non-rotating and stable) wave found in the previous study is inconsistent with Widnall's stability theory [96], [95], [97], according to which a wave is unstable when the self-induced rotation is balanced by the stagnation point flow induced by the ring. We found that the neutrally stable wave in the previous study is actually caused by the underresolved spatial mesh. With refined meshes, the wave is stable and rotates around the unperturbed axis of the vortex ring. Furthermore, contrary to the previous numerical study, on thin vortex rings the unstable mode does not grow without bound. Instead the unstable mode exhibits a periodic behavior in time and its maximum amplitude is bounded by a fraction of the core size. These numerical observations have been successfully explained using the dispersion relation for sinusoidal waves on a vortex filament with fixed core structure. Our theoretical analysis supports our numerical results.

To fully understand vortex methods [3], [10], [18], [29], [75] [87], we performed a careful study of the numerical stability and accuracy of the vortex filament method. In this study, we analyzed the effect of ODE solver, time step, and spatial step on the numerical solution. On the basis of a theoretical analysis, we found that the classical four stage fourth order Runge-Kutta method is the best performer among the ODE solvers we studied and that the constraint on the time step size imposed by the numerical stability is given by

$\Delta t \leq C\frac{\delta^2}{\Gamma}$, where Δt is the time step, Γ is the circulation, δ is the core size of the vortex filament and C is a constant depending on the ODE solver and the cut-off function used in the vortex method discretization. This criterion for selecting the time step was confirmed in numerical simulations.

We investigated the short wave instability on vortex filaments of fixed core structure. To do so, we first discussed the case of a co-rotating vortex pair and found that there are always unstable wave modes for a co-rotating vortex pair. We then studied the short wave instability on a single vortex filament with fixed core structure immersed in a co-rotating vorticity field, which is either continuous or discrete. Again, we found that short wave instability always occurs for a vortex filament surrounded by a co-rotating vorticity field. For a co-rotating vortex pair, when the separation between two filaments is comparable with or smaller than the core size, the unstable modes grow without bound and the vortex filaments stretch violently. When the separation between two filaments is large in comparison with the core size, the unstable modes grow to a maximum amplitude, go back to where they started and repeat the cycle; the maximum amplitudes of the unstable modes are bounded by a small fraction of the core size and therefore are insignificant compared to the separation. Furthermore, the maximum growth rate of the unstable modes is proportional to the circulation and inversely proportional to the square of the separation. Thus for a very thin and isolated vortex filament, the unstable modes grow slowly, and even if the unstable modes grow to their maximum amplitudes, it may be difficult to observe the unstable modes in experiments since their maximum amplitudes are bounded by a small fraction of the core size.

As a direct application, our study of the short wave instability can be used to explain the smooth behavior of superfluid vortices. It is well-known that superfluid vortex filaments behave quite differently from the classical vortex filaments [31], [37], [38], [90]. In particular, classical vortex filaments stretch and fold wildly and form small scale structures, whereas superfluid vortex filaments evolve smoothly. It has been found experimentally that superfluid vortex filaments have a very small core size ($\sim$ O(Å)) and have fixed core structures [37], [38], [90]. Thus the superfluid vortex filaments are far apart from each other in the sense that the inter-filament distance is much larger than the core size. Our study of the short wave instability revealed that when vortex filaments are far apart, the unstable modes are bounded by a small fraction of the core size and more importantly the unstable

modes do not cause the catastrophic stretching and folding. Therefore, the short wave instability is negligible for superfluid vortices. This may imply that the tiny core size of the superfluid vortex filaments is more important in accounting for their non-classical dynamics than the quantization of circulation. The different behavior of the superfluid vortices and classical vortices has been explained by Chorin [23], [27], [31], [30], with the use of statistical theories. Our study of the short wave instability supports Chorin's analysis from another point of view.

The similarity between the filament configuration of a co-rotating vortex pair and the configuration of numerical vortex filaments leaded us to relate the phenomenon of wild stretching and folding of numerical vortex filaments to the short wave instability on a vortex filament surrounded by co-rotating vortex filaments. Our numerical simulations reveal that the wild stretching and folding of the numerical vortex filaments is primarily caused by the short wave instability which occurs on a vortex filament immersed in a co-rotating vorticity field. The wild stretching and folding of the numerical vortex filaments is not due to numerical instability. It cannot be suppressed by reducing the time step size, using a more accurate ODE solver, or refining the spatial discretization. In numerical simulations, the wild stretching and folding causes the total number of vortex elements to grow exponentially, which makes simulations of long time behavior virtually impossible [11], [22]. Chorin's hairpin removal method [26], [28] is the only method which can keep the total number of vortex elements at a reasonable level by constantly removing the small scale structures from the calculation.

Bibliography

[1] D. G. Akhmetov, B. A. Lugovtsov, and V. F. Tarasov. Extinguishing gas and oil well fires by means of vortex rings. *Combustion, Explosion, and Shock Waves*, 16:490–494, 1980.

[2] A. S. Almgren, T. Buttke, and P. Colella. A fast adaptive vortex method in three dimensions. *Journal of Computational Physics*, 113:177–200, 1994.

[3] C. Anderson and C. Greengard. On vortex methods. *SIAM J. Numer. Anal.*, 22:413–440, 1984.

[4] C. Anderson and C. Greengard. The vortex ring merger problem at infinite Reynolds number. *Communications on Pure and Applied Mathematics*, 42:1123–1139, 1989.

[5] D. Auerbach. Some open questions on the flow of circular vortex rings. *Fluid Dynamics Research*, 3:209–213, 1988.

[6] G. K. Batchelor. *An Introduction to Fluid Dynamics.* Cambridge University Press, 1967.

[7] J. T. Beale. A convergent 3D vortex method with grid-free stretching. *Math. Comp.*, 46:401–424, 1986.

[8] J. T. Beale and A. Majda. Vortex methods I: convergence in three dimensions. *Math. Comp.*, 39:1–27, 1982.

[9] J. T. Beale and A. Majda. Vortex methods II: higher order accuracy in two and three dimensions. *Math. Comp.*, 39:29–52, 1982.

[10] J. T. Beale and A. Majda. High order accurate vortex methods with explicit velocity kernels. *Journal of Computational Physics*, 58:188–208, 1985.

[11] J. B. Bell and D. L. Marcus. Vorticity intensification and the transition to turbulence in the three-dimensional Euler equations. *Communications in Mathematical Physics*, 147:371–394, 1992.

[12] D. B. Bliss. *The dynamics of flows with high concentrations of vorticity.* PhD thesis, Massachusetts Institute of Technology, 1973.

[13] T. Buttke. A fast adaptive vortex method for patches of constant vorticity in two dimensions. *J. Comp. Phys.*, 89:161–186, 1990.

[14] G. L. Chahine and P. F. Genoux. Collapse of a cavitating vortex ring. *J. Fluids Eng.*, 105:400–405, 1983.

[15] A. J. Chorin. Computational aspects of the turbulence problem. Proc. 2nd int. conf. num. meth. fluid mech.,Springer,1970.

[16] A. J. Chorin. Course notes for advanced numerical analysis. Mathematics Dept., Univ. California, Berkeley.

[17] A. J. Chorin. Vortex methods for rapid flow. Proc. 2nd int. conf. num. meth. fluid mech.,Springer,1972.

[18] A. J. Chorin. Numerical study of slightly viscous flow. *Journal of Fluid Mechanics*, 57:785–796, 1973.

[19] A. J. Chorin. Vortex sheet approximation of boundary layers. *Journal of Computational Physics*, 27:428–442, 1978.

[20] A. J. Chorin. Vortex models and boundary layer instability. *SIAM J. Sci. Stat. Comput.*, 1:1–21, 1980.

[21] A. J. Chorin. Estimates of intermittency, spectra and blow-up in fully developed turbulence. *Comm. Pure. Appl. Math.*, 34:853–866, 1981.

[22] A. J. Chorin. The evolution of a turbulent vortex. *Communications in Mathematical Physics*, 83:517–535, 1982.

[23] A. J. Chorin. Turbulence and vortex stretching on a lattice. *Communications on Pure and Applied Mathematics*, XXXIX:S47–S65, 1986.

[24] A. J. Chorin. Scaling laws in the lattice vortex model of turbulence. *Comm. Math. Phys.*, 114:167–176, 1988.

[25] A. J. Chorin. Spectrum, dimension and polymer analogies in fluid turbulence. *Phys. Rev. Lett.*, 60:1947–1949, 1988.

[26] A. J. Chorin. Hairpin removal in vortex interactions. *Journal of Computational Physics*, 91:1–21, 1990.

[27] A. J. Chorin. Equilibrium statistics of a vortex filament with applications. *Communications in Mathematical Physics*, 141:619–631, 1991.

[28] A. J. Chorin. Hairpin removal in vortex interactions II. *Journal of Computational Physics*, 107:1–9, 1993.

[29] A. J. Chorin. Vortex methods, 1993. Les Houches Summer School of Theoretical Physics.

[30] A. J. Chorin. Vortex phase transitions in 2.5 dimensions. *Journal of Statistical Physics*, 76:835–856, 1994.

[31] A. J. Chorin. *Vorticity and Turbulence.* Springer, 1994.

[32] A. J. Chorin. Microstructure, renormalization, and more efficient vortex methods, 1995. Proc. 2nd. Int. Conf. Vortex Flows and Vortex Method.

[33] A. J. Chorin and J. H. Akao. Vortex equilibria in turbulence theory and quantum analogues. *Physica D*, 52:403–414, 1991.

[34] A. J. Chorin and J. E. Marsden. *A Mathematical Introduction to Fluid Mechanics.* Springer, 1979.

[35] S. C. Crow. Stability theory for a pair of trailing vortices. *AIAA*, 8(12):2172–2179, 1970.

[36] N. Didden. On the formation of vortex rings:Rolling-up and production of circulation. *J. Appl. Mech. and Phys. (ZAMP)*, 30:101–116, 1979.

[37] R. J. Donnelly. *Quantized Vortices in Helium II.* Cambridge University Press, 1991.

[38] R. J. Donnelly. Quantized vortices and turbulence in helium II. *Annual Review of Fluid Mechanics*, 25:325–371, 1993.

[39] A. Glezer and D. Coles. An experimental study of a turbulent vortex ring. *Journal of Fluid Mechanics*, 211:243–283, 1990.

[40] J. Goodman. The convergence of random vortex methods. *Comm. Pure appl. Math.*, 40:189–220, 1987.

[41] C. Greengard. Convergence of the vortex filament method. *Math. Comput.*, 47:387–398, 1986.

[42] O. H. Hald. Course notes for advanced numerical analysis. Mathematics Dept., Univ. California, Berkeley.

[43] O. H. Hald. Convergence of vortex methods for Euler's equations, II. *SIAM J. Numer. Anal.*, 16:726–755, 1979.

[44] O. H. Hald. Convergence of vortex methods for Euler's equations, III. *SIAM J. Numer. Anal.*, 24:538–582, 1987.

[45] O. H. Hald and V. M. Del Prete. Convergence of vortex methods for Euler's equations. *Math. Comp.*, 32:791–809, 1978.

[46] H. Hasimoto. A soliton on a vortex filament. *Journal of Fluid Mechanics*, 51:477–485, 1972.

[47] T. Y. Hou and J. Lowengrub. Convergence of a point vortex method for the 3D Euler equations. *Comm. Pure Appl. Math.*, 43:965–981, 1990.

[48] T. Kambe and T. Takao. Motion of distorted vortex rings. *J. Phys. Soc. Japan*, 31:591–599, 1971.

[49] Lord Kelvin. Vibrations of a columnar vortex. *Phil. Mag.*, 10:155–168, 1980.

[50] S. Kida. Tube-like structure in turbulence. *Lecture notes in Num. Appl. Anal.*, 12:137–159, 1993.

[51] S. Kida and M. Tanaka. Dynamics of vortical structures in homogeneous shear flow. *J. Fluid Mech.*, 274:43–68, 1994.

[52] J. Kim and P. Moin. The structure of the vorticity field in turbulent channel flow. *J. Fluid Mech.*, 162:339–361, 1986.

[53] R. Klein and O. M. Knio. Asymptotic vorticity structure and numerical simulation of slender vortex filaments. *Journal of Fluid Mechanics*, 284:275–321, 1995.

[54] R. Klein and A. Majda. Self-stretching of a perturbed vortex filament I: The asymptotic equation for derivation from a straight line. *Physica D*, 49:323–352, 1991.

[55] R. Klein and A. Majda. Self-stretching of perturbed vortex filaments II: Structure of solutions. *Physica D*, 53:267–297, 1991.

[56] R. Klein, A. J. Majda, and K. Damodaran. Simplified equations for the interaction of nearly parallel vortex filaments. *Journal of Fluid Mechanics*, 288:201–248, 1995.

[57] Omar M. Knio and Ahmed F. Ghoniem. Numerical study of a three-dimensional vortex method. *Journal of Computational Physics*, 86:75–106, 1990.

[58] H. O. Kreiss. Uber die stabilitatsdefinition fur differenzengleichungen die partielle differentialgleichungen approximieren. *BIT*, 2:153–181, 1962.

[59] C. H. Krutzsch. Uber eine experimentell beobachtete erscheinung an wirbelringen bei ihrer translatorischen bewegung in wirklichen flussigkeiten. *Annalen der Physik*, 35:497–523, 1939.

[60] H. Lamb. *Hydrodynamics.* Dover, 1932.

[61] C. Leiss and N. Didden. Zeitschrift der angewandte. *Z. Agnew. Math. Mech.*, 56:T206, 1976.

[62] A. Leonard. Computing three dimensional vortex flows with vortex filaments. *Ann. Rev. Fluid Mech.*, 17:523–559, 1985.

[63] F. Lund, A. Reisenegger, and C. Utreras. Critical properties of a dilute gas of vortex rings in three dimensions and the lambda transition in liquid helium. *Phys. Rev. B*, 41:155–161, 1990.

[64] A. Majda. Vorticity and the mathematical theory of incompressible fluid flow. *Comm. Pure Appl. Math.*, 39:S187–S179, 1986.

[65] A. Majda. Vorticity, turbulence and acoustics in fluid flow. *SIAM Review*, 33:349–388, 1991.

[66] P. Marcus. Numerical simulation of Jupiter's great red spot. *Nature*, 331:693–696, 1988.

[67] P. Marcus. Vortex dynamics in a shearing zonal flow. *Journal of Fluid Mechanics*, 215:393–430, 1990.

[68] T. Maxworthy. The structure and stability of vortex rings. *Journal of Fluid Mechanics*, 51:15–32, 1972.

[69] T. Maxworthy. Turbulent vortex rings. *Journal of Fluid Mechanics*, 64:227–239, 1974.

[70] T. Maxworthy. Some experimental studies of vortex rings. *Journal of Fluid Mechanics*, 81:469–495, 1977.

[71] H. K. Moffatt. The degree of knottedness of tangled vortex lines. *Journal of Fluid Mechanics*, 35:117–129, 1969.

[72] D. W. Moore. The velocity of a vortex ring with a thin core of elliptical cross-section. *Proc. Roy. Soc. London*, 370:407–415, 1980.

[73] D. W. Moore and P. G. Saffman. The motion of a vortex filament with axial flow. *Phil. Trans. R. Soc. Lond.*, 272:403–429, 1972.

[74] D. W. Moore and P. G. Saffman. The instability of a straight vortex filament in a strain field. *Proc. Roy. Soc.*, 346:413–425, 1975.

[75] E. G. Puckett. Vortex methods: An introduction and survey of selected research topics. In M. D. Gunzburger and A. A. Nicolaides, editors, *Incompressible Computational Fluid Dynamics Trends and Advances*. Cambridge, 1993.

[76] A. Pumir and E. D. Siggia. Vortex dynamics and the existence of solutions to the navier-stokes equations. *Phys. Fluids*, 30(6):1606–1626, 1987.

[77] A. Qi. *Three dimensional vortex methods for the analysis of wave propagation on vortex filaments*. PhD thesis, UC Berkeley, 1991.

[78] G. W. Rayfield and F. Reif. Quantized vortex rings in superfluid helium. *Physical Review*, 136(5A):A1194–A1208, 1964.

[79] R. D. Richtmyer and K. W. Morton. *Differential Methods for Initial-Value Problems.* John Wiley, New York, 1967.

[80] S. Roberts. *Convergence of random walk methods.* PhD thesis, UC Berkeley, 1986.

[81] G. Russo and J. Strain. Fast triangulated vortex methods for the 2D Euler equations. *J. Comput. Phys.*, 111:291–323, 1993.

[82] P. G. Saffman. The velocity of viscous vortex rings. *Studies in Applied Math.*, 49:371–380, 1970.

[83] D. W. Sallet and R. S. Widmayer. An experimental investigation of laminar and turbulent vortex rings in air. *Z. Flugwiss*, 22:207–215, 1974.

[84] D. C. Samuels and R. J. Donnelly. Sideband instability and recurrence of Kelvin waves on vortex core. *Physics Review Letters*, 64:1385–1388, 1990.

[85] J. Sethian. Course notes for advanced numerical analysis. Mathematics Dept., Univ. California, Berkeley.

[86] J. A. Sethian. Turbulent combustion in open and closed vessels. *Journal of Computational Physics*, 54:425–456, 1984.

[87] J. A. Sethian. A brief overview of vortex methods. In K. E. Gustafson and J. A. Sethian, editors, *Vortex Methods and Vortex Motion.* SIAM, 1991.

[88] J. A. Sethian and A. F. Ghoniem. Validation study of vortex methods. *Journal of Computational Physics*, 74:283–317, 1988.

[89] E. D. Siggia. Collapse and amplification of a vortex filament. *Physics of Fluids*, 28:794–805, 1985.

[90] D. R. Tilley and J. Tilley. *Superfluidity and Superconductivity.* Boston, 1986.

[91] L. Ting. *In Aircraft Wake Turbulence and its Detection (ed. J. H. Olsen, A. Goldburg & M. Rogers).* Plenum, 1971.

[92] C. Y. Tsai and S. E. Widnall. The stability of short waves on a straight vortex filament in a weak externally imposed strain field. *Journal of Fluid Mechanics*, 73:721–733, 1976.

[93] H. Y. Wang. A high order vortex method for patches of constant vorticity, 1991. Report PAM-534, Math. Dept., UC Berkeley.

[94] S. E. Widnall. The structure and dynamics of vortex filaments. *Annual Review of Fluid Mechanics*, 8:141–165, 1976.

[95] S. E. Widnall, D. B. Bliss, and C. Y. Tsai. The instability of short waves on a vortex ring. *Journal of Fluid Mechanics*, 66:35–47, 1974.

[96] S. E. Widnall and J. P. Sullivan. On the stability of vortex rings. *Proc. Roy. Soc. London*, A332:335–353, 1973.

[97] S. E. Widnall and C. Y. Tsai. The instability of the thin vortex ring of constant vorticity. *Phil. Trans. Roy. Soc.*, A287:273–305, 1977.

Ernest Orlando Lawrence Berkeley National Laboratory
One Cyclotron Road | Berkeley, California 94720

Prepared for the U.S. Department of Energy under Contract No. DE-AC03-76SF00098